

SPATIAL CORRELATION FUNCTION AND SPECIFIC PROBLEMS OF
RESERVOIR STRUCTURE

A Dissertation Presented to
the Faculty of the Department of Earth and Atmospheric Sciences
University of Houston

In Partial Fulfillment
of the Requirements for the Degree
Doctor of Philosophy

By

Aslan Gassiyev

December 2012

SPATIAL CORRELATION FUNCTION AND SPECIFIC PROBLEMS OF
RESERVOIR STRUCTURE

Aslan Gassiyev

APPROVED:

Dr. Evgeni Chesnokov, Chairman

Dr. John Castagna

Dr. Jolante van Wijk

Dr. Donald Kouri

Dr. Mark A. Smith, Dean
College of Natural Sciences and Mathematics

Acknowledgements

My deepest gratitude goes to my adviser Dr. Evgeny Chesnokov, who had encouraged me to start my life as a PhD student in the Summer of 2009. During our conversation Dr. Chesnokov challenged me to solve an integral equation, which was a Gaussian error function that had no analytical solution, and that was the beginning of my work with him. Dr. Chesnokov has definitely played a vital role in my education and helped to dramatically improve my technical knowledge beyond predicted by me limits.

In addition I would like to thank the committee members, Dr. John Castagna, Dr. Donald Kouri, and Dr. Jolante van Wijk, for their guidance as well as the opportunity to present this work.

A very special thanks to Dr. Yasser Metwally for sharing his deep knowledge about shales, to Kefei Lu and Di Chen for their laboratory experiments and provided data. I also wish to express my particular thanks to Dr. Jolante van Wijk for her considerable help in my studies of the uppermost mantle, the results of which are also presented in this manuscript.

I would like to extend my thanks as well to Dr. John Castagna and Dr. Leon Thom-
sen, who slotted me into their tight schedules for further discussions and advice.

I owe a very large debt to Mehdi Eftekharifar for his help with programming lan-
guage, and Robert Follett whose professional skills assisted me with the technical
editing.

Thanks to Sylvia Marshall for her help with registration, enrollment, and other or-
ganizational work.

I am very grateful to the Department of Earth and Atmospheric Sciences for pro-
viding the opportunity to secure an education at such a prestigious university by
granting me support in the form of teaching assistantship.

Lastly, I deeply thank my parents. By their highest level of support and belief, and
their encouraging words and patience have made this accomplishment possible.

to my parents
Vladislav Gassiev
Maria Gassieva

to my sister
Alana Gassieva

and in loving memory of my grandmother
Zoya Kelekhsaeva

SPATIAL CORRELATION FUNCTION AND SPECIFIC PROBLEMS OF
RESERVOIR STRUCTURE

An Abstract of a Dissertation

Presented to

the Faculty of the Department of Earth and Atmospheric Sciences

University of Houston

In Partial Fulfillment

of the Requirements for the Degree

Doctor of Philosophy

By

Aslan Gassiyev

December 2012

Abstract

The spatial correlation function has been introduced to the specific geophysical problem of theoretical characterization of effective elastic properties of gas shales. The spatial correlation function has been described in the form of pair correlation approximation (PCA), meaning that only binary interactions are considered and interactions of higher order are omitted (Shermergor, 1977). The theoretically built model was based on the mineralogical composition of the rock sample with which our calculations have been compared. The model consists of a matrix and gas-filled inclusions. The matrix is composed of 70 percent quartz and 30 percent illite, while the gas concentration varies from zero to ten percent.

PCA has an advantage over other averaging techniques like Voigt-Reuss-Hill (Voigt, 1928; Reuss, 1929; Hill, 1963), Eshelby's method (Eshelby, 1957), Backus (Backus, 1962) due to the presence of an additional variable called fluctuation component that is responsible for interactions between end-members.

The theoretical results for the isotropic medium with inclusions show that the difference between PCA and VRH techniques in terms of effective elastic stiffness tensor is about 7 percent, and between PCA and Eshelby's methods is around 22 percent when the aspect ratio of inclusions is 0.03. The aspect ratio of 0.02-0.03 is common for these types of inclusions (Brodov, Tikhonov, Chesnokov, Tertychnyi, & Zatsepin, 1991) . Theoretical results for anisotropic medium with inclusions show dramatical

increase in differences between these methods. The difference between PCA and VRH is 25 percent, and between PCA and Eshelby is 30 percent.

It has been observed that keeping the aspect ratio constant at a value of 0.03, and increasing the gas volume concentration in anisotropic medium, tends to reduce anisotropy. This phenomenon is explained by random orientation of inclusions, and the fact that keeping the aspect ratio and the length of inclusion constant, the crack density increases with the increase of gas content. As gas content increases the crack density increases from 0.08 at one percent of gas to 0.796 at 10 percent of gas at constant aspect ratio value of 0.03.

Comparison with experimental data shows that PCA has more solid physical background, as the result tend to match well compared to other methods presented in this work.

Table of Contents

Table of Contents	ix
List of Figures	xi
List of Tables	xii
Introduction	1
1 Theoretical Approach	4
1.1 Averaging Techniques	4
1.1.1 Voigt-Reuss-Hill (Voigt Scheme)	5
1.1.2 Eshelby's Method	9
1.2 Spatial Correlation Function. Isotropic	15
1.2.1 Green's Tensor	15
1.2.2 Correlation Tensor	19
1.3 Spatial Correlation Function. Anisotropic	24
1.3.1 Green's Tensor	24
1.3.2 Correlation Tensor	32
2 Practical Application	35
2.1 Data Description	35
2.2 Green's Tensor	37
2.3 Applications of Averaging Techniques	42
2.3.1 VRH. Single-phase Polycrystalline Media	43
2.3.2 VRH. Multi-phase Polycrystalline Media	46
2.3.3 Eshelby's Method	53
2.3.4 Discussion and Comparison of VRH with Eshelby	65
2.4 Applications of Spatial Correlation Function	75
2.4.1 Application of PCA in an Isotropic Media	75
2.4.2 Application of PCA in an Anisotropic Media	89
2.5 Comparison With Laboratory Data	104
Conclusions	109

Appendix	114
2.6 Application to Uppermost Mantle	115
References	123

List of Figures

1.1	Schematic example of Voigt and Reuss bounds	7
1.2	Voigt model	8
1.3	Reuss model	9
1.4	Schematic representation of the first step in Eshelby method	11
1.5	Schematic representation of the second step in Eshelby method	11
1.6	Schematic representation of the third step in Eshelby's method	12
1.7	Spherical Coordinates	28
1.8	Terms of parametric equation in spherical system of coordinates	30
1.9	Orthorhombic crystal lattices (Prince, 2006)	32
2.1	Location of Studied Well JR (III, IV) (Courtesy of Di Chen, 2012)	37
2.2	Euler angles	44
2.3	Isotropic medium with inclusions	47
2.4	Variation of stiffness tensor with gas content (VRH Isotropic)	48
2.5	Variation of velocities with gas content (VRH Isotropic)	49
2.6	Anisotropic media with inclusions	50
2.7	Variation of stiffness tensor with gas content (VRH Anisotropic)	51
2.8	Variation of velocities with gas content (VRH Anisotropic)	52
2.9	Variation of stiffness with gas content for high AR (Eshelby Isotropic)	55
2.10	Variation of stiffness with gas content for low AR (Eshelby Isotropic)	56
2.11	Variation of velocity with gas content for high AR (Eshelby Isotropic)	58
2.12	Variation of velocity with gas content for low AR (Eshelby Isotropic)	58
2.13	Variation of stiffness with gas content for high AR (Eshelby Anisotropic)	59
2.14	Variation of stiffness with gas content for low AR (Eshelby Anisotropic)	61
2.15	Variation of velocity with gas content for high AR (Eshelby Anisotropic)	62
2.16	Variation of velocity with gas content for low AR (Eshelby Anisotropic)	63
2.17	Difference between VRH and Eshelby stiffness tensor value. Isotropic	65
2.18	Variations of stiffness tensor with aspect ratio. Isotropic	66
2.19	Variations of ΔC_{ij} with aspect ratio at one percent of gas. Isotropic	67
2.20	Velocity differences as a function of gas content and aspect ratio. Isotropic	68
2.21	Difference between VRH and Eshelby stiffness tensor. Anisotropic	69
2.22	Variations of stiffness tensor with aspect ratio. Anisotropic	70
2.23	Variations of ΔC_{ij} with aspect ratio at one percent of gas. Anisotropic	71

2.24	Velocity differences versus gas content. Anisotropic	72
2.25	Velocity differences versus aspect ratio. Anisotropic	72
2.26	Anisotropy coefficient as a function of aspect ratio	73
2.27	Thomsen's parameters vs. gas content. (A) VRH method (B) Eshelby's method at AR=0.03	74
2.28	Terms responsible for fluctuation. Isotropic	78
2.29	Effective stiffness tensor values. Isotropic	80
2.30	Effective stiffness tensor values vs. aspect ratio. Isotropic	82
2.31	Velocities vs. gas content. Isotropic	83
2.32	Stiffness and Vp vs.gas content for different sigma. VRH Isotropic . .	86
2.33	Stiffness and Vs vs.gas content for different sigma. VRH Isotropic . .	86
2.34	Velocities vs. sigma. Isotropic	87
2.35	PCA (Eshelby's Averaging) stiffness tensor and Vp vs.gas content for different sigma at AR=0.03. Isotropic	88
2.36	PCA (Eshelby's Averaging) stiffness tensor and Vs vs.gas content for different sigma at AR=0.03. Isotropic	88
2.37	PCA Poisson's ratio vs.gas content for different sigma at AR=0.03 . .	89
2.38	Terms responsible for fluctuation. Anisotropic	92
2.39	Effective stiffness tensor vs. gas content. Anisotropic	93
2.40	Velocity vs. gas content. Anisotropic	96
2.41	Anisotropy coefficient vs. gas content at aspect ratio of 0.03	98
2.42	PCA stiffness tensor vs. sigma at gas content of five percent. VRH averaging is implemented. (A) No Gaussian (B) With Gaussian . . .	100
2.43	PCA stiffness tensor vs. sigma at gas content of five percent and AR=0.03. Eshelby's averaging is implemented. (A) No Gaussian (B) With Gaussian	101
2.44	PCA velocities vs. sigma at gas content of five percent. VRH averaging is implemented. (A) No Gaussian (B) With Gaussian	102
2.45	PCA velocities vs. sigma at gas content of five percent and AR=0.03. Eshelby's averaging is implemented. (A) No Gaussian (B) With Gaussian	102
2.46	PCA Poisson's ratio vs. sigma at five percent of gas and AR=0.03. .	103
2.47	PCA Thomsen's parameters vs. gas content and vs. sigma at AR=0.03.	104
2.48	Comparison of calculated (PCA) with measured stiffness tensor values	105
2.49	Comparison of calculated (PCA) with measured velocity values . . .	106
2.50	Comparison of theory with measurements of Thomsen's parameters .	108
2.51	Stiffness tensor values as a function of depth and offset	116
2.52	Temperature (A) and pressure (B) under Gakkel Ridge	117
2.53	P-wave velocity variation under Gakkel Ridge	118
2.54	S-wave velocity variation under Gakkel Ridge	119
2.55	P-wave anisotropy under Gakkel Ridge	120

List of Tables

2.1	Properties of theoretical model composites	36
2.2	Properties of Barnett Shale sample measured in the laboratory	36
2.3	Properties of Barnett Shale sample calculated using lab data	36
2.4	Variation of stiffness tensor with gas content (VRH Isotropic)	49
2.5	Variation of velocities with gas content (VRH Isotropic)	50
2.6	Variation of stiffness tensor with gas content (VRH Anisotropic)	51
2.7	Variation of velocities with gas content (VRH Anisotropic)	52
2.8	Stiffness tensor vs. gas content. Aspect ratio is 1 (Eshelby Isotropic)	56
2.9	Stiffness tensor vs. gas content. Aspect ratio is 0.5 (Eshelby Isotropic)	56
2.10	Stiffness tensor vs. gas content. Aspect ratio is 0.3 (Eshelby Isotropic)	57
2.11	Stiffness tensor vs. gas content. AR is 0.05 (Eshelby Isotropic)	57
2.12	Stiffness tensor vs. gas content. AR is 0.03 (Eshelby Isotropic)	57
2.13	Stiffness tensor vs. gas content. Aspect ratio is 1 (Eshelby Anisotropic)	59
2.14	Variation of stiffness with gas content. AR is 0.5 (Eshelby Anisotropic)	60
2.15	Variation of stiffness with gas content. AR is 0.3 (Eshelby Anisotropic)	60
2.16	Variation of stiffness with gas content. AR is 0.05 (Eshelby Anisotropic)	61
2.17	Variation of stiffness with gas content. AR is 0.03 (Eshelby Anisotropic)	62
2.18	Velocity vs. gas content. Aspect ratio is 1 (Eshelby Anisotropic)	63
2.19	Velocity vs. gas content. Aspect ratio is 0.5 (Eshelby Anisotropic)	63
2.20	Velocity vs. gas content. Aspect ratio is 0.3 (Eshelby Anisotropic)	64
2.21	Velocity vs. gas content. Aspect ratio is 0.05 (Eshelby Anisotropic)	64
2.22	Velocities vs. gas content. Aspect ratio is 0.03 (Eshelby Anisotropic)	64
2.23	Variations of ΔC_{ij} with aspect ratio at one percent of gas. Isotropic	67
2.24	Variations of ΔC_{ij} (%) with aspect ratio at one percent of gas. Isotropic	68
2.25	Anisotropy coefficients data	73
2.26	Terms responsible for fluctuation. Isotropic	78
2.27	PCA effective stiffness tensor values. VRH averaging. Isotropic	79
2.28	PCA effective stiffness tensor values. Eshelby AR=1. Isotropic	81
2.29	PCA effective stiffness tensor values. Eshelby AR=0.3. Isotropic	81
2.30	PCA effective stiffness tensor values. Eshelby AR=0.03. Isotropic	81
2.31	PCA velocity values. VRH and Eshelby averaging, AR=1. Isotropic	82
2.32	PCA velocity values. Eshelby, AR=0.3 and AR=0.03. Isotropic	83
2.33	PCA stiffness tensor values. VRH averaging. Anisotropic	94

2.34	PCA stiffness tensor values. Eshelby AR=1. Anisotropic	94
2.35	PCA stiffness tensor values. Eshelby AR=0.5. Anisotropic	94
2.36	PCA stiffness tensor values. Eshelby AR=0.3. Anisotropic	95
2.37	PCA stiffness tensor values. Eshelby AR=0.05. Anisotropic	95
2.38	PCA stiffness tensor values. Eshelby AR=0.03. Anisotropic	95
2.39	PCA velocities. VRH. Anisotropic	96
2.40	PCA velocities. Eshelby AR=1. Anisotropic	97
2.41	PCA velocities. Eshelby AR=0.5. Anisotropic	97
2.42	PCA velocities. Eshelby AR=0.3. Anisotropic	97
2.43	PCA velocities. Eshelby AR=0.05. Anisotropic	98
2.44	PCA velocities. Eshelby AR=0.03. Anisotropic	98
2.45	Comparison of calculated (PCA) with measured stiffness tensor values	105
2.46	Comparison of calculated (PCA) with measured (Lab) velocity values	107
2.47	Variation of stiffness tensor with depth at zero-offset	117
2.48	Variation of stiffness tensor with offset at 5 km depth	117
2.49	Variation of stiffness tensor with depth at zero-offset	119
2.50	Variation of velocity with offset at 5 km depth	119

Introduction

Effective elastic properties of the formation depend on the lithology, fluid type, and geometrical arrangement of end-members, as well as other factors. Therefore, it is necessary to have an accurate information regarding the relationships between the elastic moduli and these parameters. Moreover, to usefully predict the effective elastic properties of the media, we also need to have detailed information about the microstructure of that media. Therefore, having the information about the content (end-members) of the media and volume fraction only helps to predict the upper and lower bounds on elastic properties, for example Voigt and Reuss bounds (Voigt, 1928; Reuss, 1929) or Hashin-Shtrikman bounds (Hashin & Shtrikman, 1963).

There are many existing theoretical approaches to determine the effective physical properties of anisotropic and inhomogeneous media. By ignoring inclusion interaction, those methods can only provide an approximate calculation of effective medium parameters. We divide these models into two groups: first (Eshelby, 1957; Kuster & Toksoz, 1974; Thomsen, 1995a) describes the media with inclusions of different shapes and orientations, and second (Biot, 1956; Gassmann, 1951) considers a ho-

mogeneous composite (i.e. homogeneous fluid distribution in the rock).

The behavior of the amplitude of the correlation function, as well as the influence of the different types of inclusions has been investigated. It is complicated to answer exactly which method is the best; therefore, results are compared with experiments. Theoretical calculations are performed for an isotropic and anisotropic media. Laboratory measurements are performed on the core sample that represents the Barnett Shale. The Barnett Shale is found in New Mexico and according to the U.S. Energy Information Administration (2010), it contains 43.4 TCF of gas (Chen, 2012).

The spatial correlation function is studied in this work in the form of pair correlation approximation, meaning that only binary correlations are considered and correlations of higher order are omitted (Shermergor, 1977). The pair correlation approximation (PCA) consists of two main components, averaged value that can be obtained by any averaging technique and fluctuation component. Therefore, if we consider monomineralic medium, the fluctuation term will be equal to zero, and PCA will be equal to a simply averaged value. As an averaging technique, we use Voigt-Reuss-Hill (VRH) and Eshelby's methods. Eshelby's method utilizes more physics principles, as it allows us to control the shape and orientation of the inclusion, while the VRH method is limited to the end-member properties and their volume fractions. The combination of VRH and Eshelby's methods with PCA technique is considered for an isotropic and anisotropic media to calculate effective elastic stiffness tensor values. Based on these values we calculated velocities and Poisson's ratios, as well as anisotropy coefficients and Thomsen's parameters to analyze anisotropy.

In the end, we demonstrate an application of the PCA method in a global Earth seismology. We studied the uppermost mantle under the Gakkel Ridge to understand its elastic properties and characterize anisotropy in that area.

Chapter 1

Theoretical Approach

1.1 Averaging Techniques

This section consists of three subsections, each describing techniques that are frequently used to estimate the average values of elastic properties and an approximation of elastic properties for isotropic and anisotropic media. The first subsection covers the theory behind the two averaging techniques, one called Voigt-Reuss-Hill (VRH) averaging, and the other is called Eshelby's averaging. Each method has its advantages and limitations, and may not be applicable to every scenario. This section describes the theoretical cases in which a particular averaging method might be applied to obtain reliable results. However, there are some situations when neither of the averaging methods provide desirable answers, and we must therefore look to alternative techniques. In our case, the additional technique is called pair correlation approximation (PCA), and is covered in great detail in the final two subsections.

1.1.1 Voigt-Reuss-Hill (Voigt Scheme)

First, we would like to define the effective parameters considering polycrystalline media. Each point \mathbf{r} of this media satisfies the Hooke's law, which relates stress to strain and strain to stress through compliance and stiffness tensors respectively:

$$\begin{aligned}\sigma_{ij}(\mathbf{r}) &= C_{ijkl}(\mathbf{r})\epsilon_{kl}(\mathbf{r}) \\ \epsilon_{kl}(\mathbf{r}) &= S_{ijkl}(\mathbf{r})\sigma_{ij}(\mathbf{r})\end{aligned}\tag{1.1}$$

In the equation above, σ_{ij} is stress, and ϵ_{kl} is strain. If in multi-component medium, like polycrystalline body, each component can be described by Hooke's law, then the whole media can also be described by Hooke's law. Elastic stiffness (C_{ijkl}) and compliance (S_{ijkl}) tensors are constants within one inhomogeneous phase, but change abruptly after the transition into another phase. Therefore, they can be expressed through averaged and fluctuating components:

$$\begin{aligned}C_{ijkl}(\mathbf{r}) &= \langle C_{ijkl}(\mathbf{r}) \rangle + C'_{ijkl}(\mathbf{r}) \\ S_{ijkl}(\mathbf{r}) &= \langle S_{ijkl}(\mathbf{r}) \rangle + S'_{ijkl}(\mathbf{r})\end{aligned}\tag{1.2}$$

Here, $\langle C_{ijkl}(\mathbf{r}) \rangle$ is the averaged component, and $C'_{ijkl}(\mathbf{r})$ is the fluctuating component of stiffness tensor. The same idea applies in the case of the stress and strain:

$$\begin{aligned}\sigma_{ij}(\mathbf{r}) &= \langle \sigma_{ij}(\mathbf{r}) \rangle + \sigma'_{ij}(\mathbf{r}) \\ \epsilon_{kl}(\mathbf{r}) &= \langle \epsilon_{kl}(\mathbf{r}) \rangle + \epsilon'_{kl}(\mathbf{r})\end{aligned}\tag{1.3}$$

where, $\langle \sigma_{ij}(\mathbf{r}) \rangle$ is the averaged component of stress, $\sigma'_{ij}(\mathbf{r})$ is the fluctuating component of stress, $\langle \epsilon_{kl}(\mathbf{r}) \rangle$ is the averaged component of strain, and $\epsilon'_{kl}(\mathbf{r})$ is the fluctuating component of strain. Combining the equation (1.2) with the equation (1.3) allows us to express Hooke's law through average and fluctuation components:

$$\langle \sigma_{ij}(\mathbf{r}) \rangle + \sigma'_{ij}(\mathbf{r}) = (\langle C_{ijkl}(\mathbf{r}) \rangle + C'_{ijkl}(\mathbf{r}))(\langle \epsilon_{kl}(\mathbf{r}) \rangle + \epsilon'_{kl}(\mathbf{r})) \quad (1.4)$$

Hooke's law (1.4) is expressed through a stiffness tensor, and in the same way we can express it through a compliance tensor. Opening the brackets on the left-hand side of the equation we receive:

$$\langle \sigma_{ij}(\mathbf{r}) \rangle + \sigma'_{ij}(\mathbf{r}) = \langle C_{ijkl}(\mathbf{r}) \rangle \langle \epsilon_{kl}(\mathbf{r}) \rangle + C'_{ijkl}(\mathbf{r}) \langle \epsilon_{kl}(\mathbf{r}) \rangle + \langle C_{ijkl}(\mathbf{r}) \rangle \epsilon'_{kl}(\mathbf{r}) + C'_{ijkl}(\mathbf{r}) \epsilon'_{kl}(\mathbf{r}) \quad (1.5)$$

Averaging both sides of equation (1.5), and combining the expressions we get:

$$\langle \sigma_{ij}(\mathbf{r}) \rangle = \langle C_{ijkl}(\mathbf{r}) \rangle \langle \epsilon_{kl}(\mathbf{r}) \rangle + \langle C'_{ijkl}(\mathbf{r}) \epsilon'_{kl}(\mathbf{r}) \rangle \quad (1.6)$$

Given the elastic moduli of the mineral constituents it is possible to calculate the moduli of the composite if certain assumptions are made. For example, Voigt (Voigt, 1928) made a first attempt to average elastic constants of monocrystal to determine elastic properties of polycrystalline aggregates. He calculated the composite moduli by averaging over all crystal lattice orientations, and assuming that the strain is

the same throughout the composite when a given stress is applied externally. Reuss (Reuss, 1929) did the same, assuming that the stress is internally everywhere the same for a given overall strain of the composite. The Voigt and Reuss averages are interpreted as the ratio of average stress and average strain within the composite, and they are sometimes called iso-strain and iso-stress averages, respectively. Hill (Hill, 1952) proved that these moduli constitute upper (Voigt) and lower (Reuss) bounds, providing that the assumption of macroscopic homogeneity is statistically valid. Graphically, VRH bounds are shown in figure 1.1.

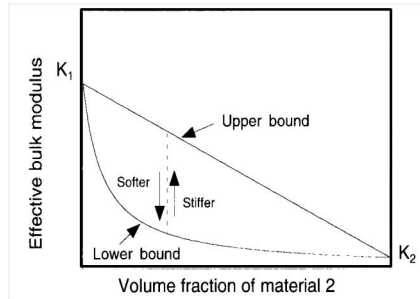


Figure 1.1: Schematic example of Voigt and Reuss bounds

While the individual minerals may be anisotropic, their random orientation results in the aggregate composite being isotropic. Thus, it is common to speak of single mineral bulk and shear moduli even when the mineral crystal is anisotropic; in such cases it should be understood that the mineral moduli actually represent those for a zero-porosity composite of randomly oriented mineral grains. Defining the component moduli in this fashion, we can simply express the Voigt and Reuss bounds for an isotropic composite. Voigt and Reuss developed averaging schemes to estimate the elastic constants of monomineralic aggregates. To apply Voigt and Reuss

moduli on rocks they assumed the separation of the individual rock components (i.e. minerals, pore-filling material, and their arrangement). In the Voigt model (figure 1.2), the strain is the same throughout the composite when a given stress is applied externally.

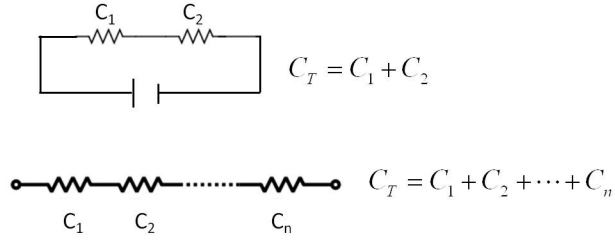


Figure 1.2: Voigt model

The n individual components are assumed to be isotropic, and their elastic properties are described by bulk modulus K , and shear modulus μ . The elastic moduli are:

$$\begin{aligned}
 K_V &= \sum_{i=1}^n X_i K_i \\
 \mu_V &= \sum_{i=1}^n X_i \mu_i
 \end{aligned}
 \tag{1.7}$$

In the Reuss (1927) model (figure 1.3), the stress is homogeneous and the strain in each layer differs. The elastic moduli are:

$$\begin{aligned}
 \frac{1}{K_R} &= \sum_{i=1}^n \frac{X_i}{K_i} \\
 \frac{1}{\mu_R} &= \sum_{i=1}^n \frac{X_i}{\mu_i}
 \end{aligned}
 \tag{1.8}$$

where, K_R and μ_R are the composite Reuss-average bulk and shear moduli.

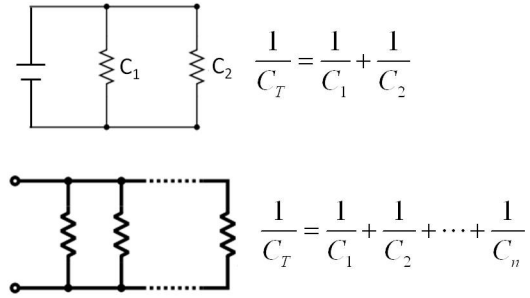


Figure 1.3: Reuss model

If we have isotropic effective material, the Voigt and Reuss bulk and shear moduli form bounds on the possible composite model. Thus, the Voigt relationship leads to the upper bound, and the Reuss relationship to the lower. The real values of elastic moduli are situated between these two bounds. When the shear modulus is the same for all constituents, the composite modulus is given by the simple average of the Voigt and Reuss bounds (Hill, 1963). This is basically an arithmetic or geometric mean that according to Hill (1952) is a useful approximation to the composite moduli. This approximation became very popular and is known as Voigt-Reuss-Hill average.

1.1.2 Eshelby's Method

The general idea of existing models is to characterize the effective physical properties of micro-inhomogeneous anisotropic media. Since we have the great amount of interaction between inclusions, the presented methods can only provide approximate solutions. One of the approximating methods that considers no interactions between inclusions and their low volume concentration is the Eshelby's method (Eshelby,

1957). The elastic bounding methods establish only upper and lower bounds when we do not take into account shape and geometrical arrangement of grains, as well as interaction between grains. However, Eshelby's method considers specific shape and orientation. The problem that was solved by Eshelby concentrates on stress and strain fields created by an ellipsoidal inclusion or inhomogeneity. Orientation of inhomogeneity can be of any type, therefore it should be characterized by corresponding statistical distribution functions. Eshelby in his work concentrated on matrix that contains only one inclusion, hence if we consider a media with many inclusions, it is important to note that the distance between inclusions has to be significantly large for this method to work properly. Even though the media under study is micro-inhomogeneous and anisotropic, the matrix and inclusions themselves can be homogeneous and isotropic. The procedure of determination of effective elastic properties using Eshelby method consists of multiple steps.

Step 1. Matrix and inclusion are free from action of any external forces. Remove inhomogeneity from the matrix, and replace it with the inclusion of exactly the same shape, but with the same elastic properties as matrix. The removed inclusion experiences a homogeneous strain (or eigenstrain) without the application of stress. This homogeneous strain is symbolically defined as ϵ^T . Elastic constants in this case have not changed and stress is equal to zero. Figure (1.4) schematically represents the first step, where C^M is the elastic stiffness tensor of matrix, C^I is the elastic stiffness tensor of inclusion, σ is stress.

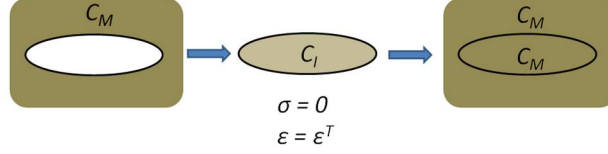


Figure 1.4: Schematic representation of the first step in Eshelby method

Step 2. Restore the inhomogeneity to its original shape and size by applying to its surface forces:

$$-\sigma_{ij}^T n_j = -C_{ijkl}^M \epsilon_{kl}^T n_j \quad (1.9)$$

where, n_j are components of vector normal to the surface of inclusion, and C_{ijkl}^M are components of the stiffness tensor of matrix. The negative sign means that applied forces are in opposite direction than the vector normal to the surface. Put inclusion back to its initial place and rejoin it with matrix. Figure (1.5) shows the scheme of the second step. Each point along the surface between matrix and inclusion returns to the same position as it was before removal of our inhomogeneity. The stress field in the inclusion becomes equal to $-\sigma^T$, and zero in the matrix.

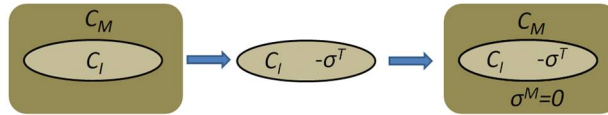


Figure 1.5: Schematic representation of the second step in Eshelby method

Step 3. In this step we want to stop applying stress $-\sigma^T$ to the surface of inclusion, i.e. we want to remove body force acting on the surface between matrix and inclusion. Therefore, we need to apply compensating forces that are symbolically defined as

$+\sigma_{ij}^T n_j$. These forces will create in the matrix and inhomogeneity the strain that is called compensating and symbolically represented as ϵ^C . The corresponding stress in this case is:

$$\sigma^C = C^M \epsilon^C \quad (1.10)$$

This is a Hooke's law that relates stress to strain through elastic constant. Therefore, in the matrix we have stress σ^C , strain ϵ^C , and in inclusion we have stress equal to $\sigma^C - \sigma^T$. This is illustrated in Figure 1.6.

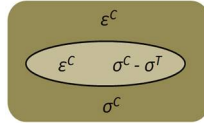


Figure 1.6: Schematic representation of the third step in Eshelby's method

Since we know the distribution of body forces in our media we can find the relationship between compensating strain ϵ^C , and strain in inclusion ϵ^T using Green's tensor (G_{im}), that characterizes displacement. According to Hooke's law we have:

$$\begin{aligned} \sigma_{ij} &= C_{ijkl} \epsilon_{kl} \\ \epsilon_{kl} &= \frac{1}{2} \left(\frac{\partial u_k}{\partial x_l} + \frac{\partial u_l}{\partial x_k} \right) \end{aligned} \quad (1.11)$$

Due to symmetry ($\epsilon_{kl} = \epsilon_{lk}$), we can write:

$$\begin{aligned} \epsilon_{kl} &= u_{k,l} \\ u_{k,l} &\equiv \left(\frac{\partial u_k}{\partial x_l} \right) \end{aligned} \quad (1.12)$$

Therefore Hooke's law can be expressed as:

$$\sigma_{ij} = C_{ijkl}u_{k,l} \quad (1.13)$$

Displacement through the Green's tensor is expressed as:

$$u_m = \iiint G_{im}(\mathbf{r} - \mathbf{r}_1)f_i(\mathbf{r}_1)d\mathbf{r}_1 + \iint u_i(\mathbf{r}_1)[C_{ijkl}G_{km,l}(\mathbf{r} - \mathbf{r}_1) + G_{im}(\mathbf{r} - \mathbf{r}_1)\sigma_{ij}(\mathbf{r}_1)]dS_{1j} \quad (1.14)$$

This is general expression for a media of volume V and surface between inclusion and matrix S , where \mathbf{r} and \mathbf{r}_1 are the points in the volume V and on the surface S respectively; f_i are components of a density of the volume forces. From the equation above we can find the compensating displacement u_i^C . Since, after step three our stress $\sigma^T = const.$, volume force as well as displacements on the surface are equal to zero, we have:

$$u_i^C(\mathbf{r}) = \iint \sigma_{ik}^T G_{il}(\mathbf{r} - \mathbf{r}_1)dS_{1k} = -\sigma_{ik}^T \iiint G_{il,k}(\mathbf{r} - \mathbf{r}_1)d\mathbf{r}_1 \quad (1.15)$$

Now we can go from displacement to strain field taking into account that only Green's function depends on coordinates, hence we receive:

$$\epsilon_{mn}^C = \frac{1}{2}(u_{m,n} + u_{n,m}) = -C_{klj}^M \epsilon_{ij}^T \frac{[\iiint G_{km,ln}(\mathbf{r} - \mathbf{r}_1)d\mathbf{r}_1 + G_{kn,lm}(\mathbf{r} - \mathbf{r}_1)d\mathbf{r}_1]}{2} \quad (1.16)$$

To simplify this equation we can write:

$$\epsilon_{mn}^C = T_{mnij} \epsilon_{ij}^T \quad (1.17)$$

where, T_{mnij} is an Eshelby tensor, which is expressed as:

$$T_{mnij} = -C_{klij}^M \frac{[\iiint G_{km,ln}(\mathbf{r} - \mathbf{r}_1) d\mathbf{r}_1 + G_{kn,lm}(\mathbf{r} - \mathbf{r}_1) d\mathbf{r}_1]}{2} \quad (1.18)$$

To calculate Eshelby's tensor we have to perform volume integration of Green's tensor second derivative.

Step 4. In this step we apply one more homogeneous strain ϵ^A to the whole body (matrix-inclusion system). That will create a strain on the surface of inclusion $\epsilon^C + \epsilon^A$, and within the inclusion strain $\epsilon^C + \epsilon^A - \epsilon^T$. We remember that our inhomogeneity has elastic stiffness tensor C^I , so we replace now inclusion with matrix properties by the initial inclusion without disturbing our stress fields in the media. In this case the stress in the inclusion with elastic properties C^I should have the form:

$$\sigma^I = C^I \epsilon^I = C^I (\epsilon^C + \epsilon^A) = \sigma^M = C^M (\epsilon^C + \epsilon^A - \epsilon^T) \quad (1.19)$$

From equation (1.19) we have:

$$C^I (\epsilon^C + \epsilon^A) = C^M (\epsilon^C + \epsilon^A - \epsilon^T) \quad (1.20)$$

Opening brackets we receive:

$$\begin{aligned}
C^I \epsilon^C + C^I \epsilon^A &= C^M \epsilon^C + C^M \epsilon^A - C^M \epsilon^T \\
C^M \epsilon^T &= C^M \epsilon^C - C^I \epsilon^C + C^M \epsilon^A - C^I \epsilon^A \\
C^M \epsilon^T &= \epsilon^C (C^M - C^I) + \epsilon^A (C^M - C^I)
\end{aligned} \tag{1.21}$$

We also know that $\epsilon^C = T\epsilon^T$, hence:

$$\begin{aligned}
C^M \epsilon^T - T\epsilon^T C^M - T\epsilon^T C^I &= \epsilon^A (C^M - C^I) \\
\epsilon^T (C^M - T(C^M - C^I)) &= \epsilon^A (C^M - C^I)
\end{aligned} \tag{1.22}$$

Finally, the solution for ϵ^T will be:

$$\epsilon^T [(C^M - C^I)T - C^M]^{-1} = (C^M - C^I)\epsilon^A \tag{1.23}$$

Rearranging and substituting the terms in our equation we can also find the equation for the strain field in the inclusion ($\epsilon^I = \epsilon^C + \epsilon^A$) with elastic properties C^I .

1.2 Spatial Correlation Function. Isotropic

1.2.1 Green's Tensor

To calculate effective stiffness tensor of the media we need to consider the effect of elastic interactions between end-members. Taking into account that we describe our

media as statistically homogeneous we use Green's function for displacement to consider elastic interactions between end-members. Analytically Green's function can be solved for isotropic and transversely isotropic media (Lifshitz & Rozentsweig, 1947; Mura, 1991). However, there are numerous techniques available to solve Green's function numerically (Phan, Gray, & Kaplan, 2004; Sales & Gray, 1998). Both approaches are described in this manuscript.

To solve Green's function analytically we follow Shermergor's (Shermergor, 1977) approach. Combining Newton's second law and Hooke's law we receive an equation that allows us to define an elastic displacement field in an unbounded media:

$$L_{ik}u_k + f_i = 0 \quad (1.24)$$

This equation is called an equilibrium equation of displacement, where L is a differential operator, u_k is a displacement, f_i is the volumetric forces, and C_{ijkl} are components of elastic stiffness tensor. Symbolically L can be expressed as:

$$L_{ik} = \frac{\partial}{\partial r_j} C_{ijkl} \frac{\partial}{\partial r_l} \quad (1.25)$$

The goal is to find displacement vector u_i in a random location r_i of the media.

Applying convolution integral we have:

$$u_k(\mathbf{r}) = G_{ik} * f_i = \int G_{ik}(\mathbf{r} - \mathbf{r}_1) f_i(\mathbf{r}_1) d\mathbf{r}_1 \quad (1.26)$$

G_{ik} in this case is called a Green's tensor of an equilibrium equation. Differential equation for Green's tensor we obtain by applying differential tensor L on both sides of the equation (1.26):

$$\mathbf{L}\mathbf{G} = -\mathbf{I}\delta \quad (1.27)$$

Here, I is a second rank unit tensor with components of Kronecker Delta δ_{ik} ; δ is called Dirac's delta function. Equation (1.27) defines Green's tensor for unbounded medium. To demonstrate the accuracy of Green's tensor differential equation (1.27) we add differential operator to both sides of equation (1.26) and apply properties of Dirac's delta function:

$$\mathbf{L}\mathbf{u}(\mathbf{r}) = \int \mathbf{L}\mathbf{G}(\mathbf{r} - \mathbf{r}_1)\mathbf{f}(\mathbf{r}_1)d\mathbf{r}_1 = - \int \delta(\mathbf{r} - \mathbf{r}_1)\mathbf{f}(\mathbf{r}_1)d\mathbf{r}_1 = -\mathbf{f}(\mathbf{r}) \quad (1.28)$$

From equation (1.26) we can see that the component of Green's tensor defines the displacement component at point \mathbf{r} in an unbounded elastic medium that is a result of a unit force applied at point \mathbf{r}_1 . To obtain a solution to Green's tensor we perform Fourier integration:

$$\begin{aligned} G_{ik}(\mathbf{k}) &= \int G_{ik}(\mathbf{r}) \exp^{-i\mathbf{k}\mathbf{r}} d\mathbf{r} \\ G_{ik}(\mathbf{r}) &= \frac{1}{8\pi^3} \int G_{ik}(\mathbf{k}) \exp^{i\mathbf{k}\mathbf{r}} d\mathbf{k} \end{aligned} \quad (1.29)$$

Combining equation (1.25) with equation (1.27) and applying Fourier transformation we receive:

$$C_{ijkl}k_jk_lG_{kn}(\mathbf{k}) = \delta_{in} \quad (1.30)$$

The term $C_{ijkl}k_jk_l$ is called a Green-Christoffel tensor and usually denoted as Γ_{ik} . Green-Christoffel tensor for isotropic media can be expressed through Lamé coefficients:

$$\Gamma_{ik} = \mu k^2 \delta_{ik} + (\lambda + \mu) k_i k_k \quad (1.31)$$

We can clearly see that in order to obtain a solution for Green's tensor we need to find an inverse of Green-Christoffel tensor (Γ_{ik}^{-1}). Therefore, we receive:

$$G_{ik}(\mathbf{k}) = \Gamma_{ik}^{-1} = \frac{1}{\mu k^2} \left(\delta_{ik} - \frac{(\lambda + \mu)}{(\lambda + 2\mu)} \frac{k_i k_k}{k} \right) \quad (1.32)$$

Applying inverse Fourier transform we receive expression for original Green's tensor:

$$G_{ik}(\mathbf{r}) = \frac{1}{8\pi\mu} \left(\delta_{ik} \frac{1}{\pi^2} \int \frac{k_i k_k}{k^4} \exp^{i\mathbf{k}\mathbf{r}} d\mathbf{k} - \frac{(\lambda + \mu)}{(\lambda + 2\mu)} \frac{1}{\pi^2} \int \frac{1}{k^2} \exp^{i\mathbf{k}\mathbf{r}} d\mathbf{k} \right) \quad (1.33)$$

Poisson's equality for single point charge (Shermergor, 1977) has been implemented. The equation (1.33) provides a solution for Green's tensor components of equilibrium equation. However, for our work we need to obtain first and second derivatives of Green's tensor. Analytical expression of second derivative of Green's tensor contains singular and formal parts. We show only singular part:

$$G_{ik,lm}(\mathbf{r}) = \frac{1}{3\mu} \delta(\mathbf{r}) \left(\delta_{ik} \delta_{lm} - \frac{1}{5} \frac{(\lambda + \mu)}{(\lambda + 2\mu)} (\delta_{ik} \delta_{lm} + \delta_{il} \delta_{km} + \delta_{im} \delta_{lk}) \right) \quad (1.34)$$

To obtain numerical calculations we use technical computing software Maple 14.

1.2.2 Correlation Tensor

The local elastic tensors can be represented as a sum of average and fluctuation component. To study in details fluctuation part several methods were introduced. All those methods can only provide approximate results since there is no analytical solution. One of those approximation techniques is called pair correlation approximation and it is a method that was implemented in this work. Pair correlation approximation (PCA) technique was shown in several publications (Lifshitz & Rozentsweig, 1946; Shermergor, 1977). This method works well if we have small difference in elastic moduli between end-members of multi-compositional material. Combining together Newton's 2^{nd} law with Hooke's law and considering equilibrium condition (acceleration is zero), we receive:

$$\begin{aligned}
 L_{ik}u_k + f_i &= 0 \\
 L_{ik} &= \frac{\partial}{\partial x_j} C_{ijkl} \frac{\partial}{\partial x_l}
 \end{aligned}
 \tag{1.35}$$

Here, L_{ik} is the differential operator, u_k is the displacement, f_i is the volumetric forces, and C_{ijkl} is the elastic stiffness tensor. The fluctuating part usually has a small value, therefore averaging this value will be even smaller and we can neglect it. Differential operator and displacement vector can be expressed through their average and fluctuating components:

$$\begin{aligned}
 L_{ik} &= \langle L_{ik} \rangle + L'_{ik} \\
 u_k &= \langle u_k \rangle + u'_k
 \end{aligned}
 \tag{1.36}$$

Multiplying together expressions in equation (1.36) and averaging the result we receive:

$$\langle L_{ik} \rangle \langle u_k \rangle + \langle L'_{ik} u'_k \rangle + f_i = 0 \quad (1.37)$$

We do not know exact relationship between fluctuating and average component, but we may assume that the relationship is linear. Therefore introducing another operator \mathbf{Q} we can establish this relationship in the form:

$$u'_k = Q_{kn} \langle u_n \rangle \quad (1.38)$$

Substituting equation (1.38) into equation (1.37) and rearranging the result, we receive:

$$(\langle L_{ik} \rangle + \langle L'_{in} Q_{kn} \rangle) \langle u_k \rangle + f_i = 0 \quad (1.39)$$

We are interested in calculation of effective elastic stiffness tensor, therefore it is important to have an expression for effective differential operator since according to equation (1.35) stiffness tensor is within this operator. Expression in the brackets of equation (1.39) represents effective differential operator, hence substituting we obtain:

$$L_{ik}^* \langle u_k \rangle + f_i = 0 \quad (1.40)$$

To find the effective elastic stiffness tensor we need to find a solution for effective differential operator, which in turn requires knowledge about operator \mathbf{Q} . To find

Q we subtract equation (1.37) from equation (1.35). Rearranging and canceling negligibly small terms we receive:

$$\langle L_{ik} \rangle u'_k + \langle u_k \rangle L'_{ik} = 0 \quad (1.41)$$

We know that L_{ik} is a differential operator, therefore introducing integral operator M_{ik} the following holds true:

$$M_{im} \langle L_{mk} \rangle = -\delta_{ik} \quad (1.42)$$

Substituting (1.42) into (1.41) and solving for fluctuating component of displacement we obtain:

$$u'_k = M_{km} L'_{mn} \langle u_n \rangle \quad (1.43)$$

If we compare (1.43) with (1.38) we notice that operator Q_{kn} is a combination of integral and differential operators:

$$Q_{kn} = M_{km} L'_{mn} \quad (1.44)$$

The kernel of integral operator M_{km} is the Green's tensor of operator L_{mn} . Combining equation (1.44) together with equation (1.39) and using the definition of M_{km} we obtain an expression for effective differential operator:

$$\langle L_{ik}(\mathbf{r}) \rangle \langle u_k(\mathbf{r}) \rangle + \langle L'_{ik}(\mathbf{r}) \int G_{km}(\mathbf{r} - \mathbf{r}_1) L'_{mn}(\mathbf{r}_1) \langle u_n(\mathbf{r}_1) \rangle d\mathbf{r}_1 + f_i = 0 \quad (1.45)$$

Equation (1.45) describes the relationship between average and fluctuating elastic characteristics in statistically inhomogeneous media. Equation (1.45) as it was stated above represents description of the problem, but not its solution. To solve this expression pair correlation function is introduced. This function is eighth-rank tensor that is expressed through the pair of averaged fluctuating elastic components of stiffness tensor. For statistically homogeneous media properties do not depend on coordinates, therefore argument of correlation function should represent the properties between points of the media:

$$\langle C'_{ijkl}(\mathbf{r}) C'_{pqrs}(\mathbf{r}_1) \rangle = B_{pqrs}^{ijkl}(\mathbf{r} - \mathbf{r}_1) \quad (1.46)$$

To show correlation approximation following Voigt model we consider iso-strain condition. In equation (1.45) we see that $L'_{ik}(\mathbf{r})$ can be moved under integration sign because integration is on \mathbf{r}_1 . Considering equation (1.35), we obtain:

$$\langle L_{ik}(\mathbf{r}) \rangle \langle u_k(\mathbf{r}) \rangle + \frac{\partial}{\partial r_j} \int \langle C'_{ijkl}(\mathbf{r}) G_{km,l}(\mathbf{r} - \mathbf{r}_1) \frac{\partial}{\partial r_q} C'_{mnpq}(\mathbf{r}_1) \rangle \langle u_{n,p}(\mathbf{r}_1) \rangle d\mathbf{r}_1 + f_i = 0 \quad (1.47)$$

To simplify equation (1.47) the following identity is introduced:

$$G_{km,l}(\mathbf{r} - \mathbf{r}_1) \frac{\partial}{\partial r_q} = \frac{\partial}{\partial r_q} G_{km,l}(\mathbf{r} - \mathbf{r}_1) + G_{km,lq}(\mathbf{r} - \mathbf{r}_1) \quad (1.48)$$

Therefore, substituting (1.48) into (1.47), we receive:

$$\langle L_{ik}(\mathbf{r}) \rangle \langle u_k(\mathbf{r}) \rangle + \frac{\partial}{\partial r_j} \int G_{km,lq}(\mathbf{r} - \mathbf{r}_1) B_{mqnp}^{ijkl}(\mathbf{r} - \mathbf{r}_1) \langle u_{n,p}(\mathbf{r}_1) \rangle d\mathbf{r}_1 + f_i = 0 \quad (1.49)$$

Equation (1.49) represents effective differential operator acting on average displacement. Considering equation (1.35) and applying mathematical operations we obtain expression for effective elastic stiffness tensor:

$$C_{ijnp}^* = \langle C_{ijnp} \rangle + \int G_{km,lq}(\mathbf{r} - \mathbf{r}_1) B_{mqnp}^{ijkl}(\mathbf{r} - \mathbf{r}_1) d\mathbf{r}_1 \quad (1.50)$$

Solution of this equation depends on solution of integral expression, which in turn is non-trivial. One of the methods is by applying convolution. Applying Fourier transformation we obtain:

$$\int G_{rs}(\mathbf{r}) B_{mqnp}^{ijkl}(\mathbf{r} - \mathbf{r}_1) d\mathbf{r}_1 = \frac{1}{8\pi^3} \int G_{rs}(\mathbf{k}) B_{mqnp}^{ijkl}(\mathbf{k}) \exp^{-i\mathbf{k}\mathbf{r}} d\mathbf{k} \quad (1.51)$$

It was assumed that $\mathbf{r} - \mathbf{r}_1 = \mathbf{r}_2$. Substituting (1.51) into (1.50), we get:

$$C_{ijnp}^* = \langle C_{ijnp} \rangle + \frac{1}{8\pi^3} \int G_{km,lq}(\mathbf{k}) B_{mqnp}^{ijkl}(\mathbf{k}) d\mathbf{k} \quad (1.52)$$

The value of \mathbf{r} was set to be zero, which makes exponential term to be equal to one.

1.3 Spatial Correlation Function. Anisotropic

1.3.1 Green's Tensor

Physically Green's tensor characterizes components of the vector of displacement that occurs along axis r_j at point r as a result of unit force applied at point r_1 and acting along axis r_i . Green's tensor is an important tool in an evaluation of elastic fields especially in an anisotropic and inhomogeneous body with inclusions. Along with Green's tensor we need to know its first and second derivatives the importance and use of which are demonstrated below. Analytically expressions of Green's tensor can be built for an anisotropic medium of any type of symmetry. However, analytically Green's tensor expression can be solved only for anisotropic medium of hexagonal type of symmetry. Therefore, to obtain results for medium of other types of symmetry we analytically build an expression that is further solved using numerical computations. We use technical computing software Maple 14. As in the case of isotropic medium we start with equilibrium equation. Equilibrium equation is a combination of Newton's second law and Hooke's law where acceleration term is equal to zero.

Newton's second law:

$$\frac{\partial \sigma_{ij}}{\partial x_j} + f_i = \rho \frac{\partial^2 u_i}{\partial t^2} \quad (1.53)$$

Here, we consider a unit volume, and therefore our mass is equal to density. If we have a static condition, acceleration term is equal to zero, and second Newton's law becomes:

$$\frac{\partial \sigma_{ij}}{\partial x_j} + f_i = 0 \quad (1.54)$$

Hooke's law of elasticity:

$$\sigma_{ij} = C_{ijkl} \epsilon_{kl} \quad (1.55)$$

Here, σ_{ij} is called a second-rank stress tensor, C_{ijkl} is a fourth-rank stiffness tensor, and ϵ_{kl} is a second-rank strain tensor. Strain tensor can be expressed in terms of a displacement vector u_i :

$$\epsilon_{kl} = \frac{1}{2} \left(\frac{\partial u_k}{\partial x_l} + \frac{\partial u_l}{\partial x_k} \right) \quad (1.56)$$

In the case of assumed symmetry between indices the strain tensor equation becomes:

$$\epsilon_{kl} = \frac{\partial u_k}{\partial x_l} \quad (1.57)$$

Therefore, the equilibrium equation acquires the following form:

$$\frac{\partial}{\partial x_j} C_{ijkl} \frac{\partial}{\partial x_l} u_k + f_i = 0 \quad (1.58)$$

In the case of homogeneity or statistical homogeneity the stiffness tensor term (C_{ijkl}) becomes independent of coordinates and equation (1.58) obtains the following ex-

pression:

$$C_{ijkl} \frac{\partial^2}{\partial x_j \partial x_l} u_k + f_i = 0 \quad (1.59)$$

Statistical homogeneity does not mean that the properties of the medium at every point are the same, however, it implies that the level of inhomogeneity at every point is the same. The differential term in the equilibrium equation is usually substituted by the differential operator (L_{ik}) and the final expression of the equilibrium equation takes the following form:

$$L_{ik} u_k = -f_i \quad (1.60)$$

The solution of the equilibrium equation, as it was described in previous chapters, involves convolution of Green's tensor (G_{ik}) with the density of volume forces distribution (f_i):

$$u_i(\mathbf{r}) = G_{ik} * f_k = \int G_{ik}(\mathbf{r} - \mathbf{r}_1) f_k(\mathbf{r}) d\mathbf{r}_1 \quad (1.61)$$

Substituting equation (1.61) into equation (1.60) we receive:

$$L_{ik} G_{kj}(\mathbf{r}) = -\delta_{ij} \delta(\mathbf{r}) \quad (1.62)$$

Here, δ_{ij} is called a Kronecker delta and $\delta(\mathbf{r})$ is a Dirac's delta function. By applying a Fourier transform and using an expression for differential operator (L_{ik}) we obtain equation (1.62) in a wave number (\mathbf{k}) domain. Fourier transformation integral:

$$G_{ik}(\mathbf{k}) = \int G_{ik}(\mathbf{r}) \exp^{-i\mathbf{k}\mathbf{r}} d\mathbf{r} \quad (1.63)$$

Inverse Fourier transformation integral:

$$G_{ik}(\mathbf{r}) = \frac{1}{(2\pi)^3} \int G_{ik}(\mathbf{k}) \exp^{i\mathbf{k}\cdot\mathbf{r}} d\mathbf{k} \quad (1.64)$$

Therefore, in the wave number domain we have:

$$C_{ijkl}k_jk_lG_{kn}(\mathbf{k}) = \delta_{in} \quad (1.65)$$

Here, we introduced Green-Christoffel tensor:

$$\Gamma_{ik}(\mathbf{k}) = C_{ijkl}k_jk_l \quad (1.66)$$

Therefore, equation (1.65) becomes:

$$\Gamma_{ik}(\mathbf{k})G_{kn}(\mathbf{k}) = \delta_{in} \quad (1.67)$$

Green's tensor solution in the wave number domain can be obtained by finding the inverse of Green-Christoffel tensor:

$$G_{ik}(\mathbf{k}) = \Gamma_{ik}^{-1}(\mathbf{k}) = \frac{\Gamma_{ik}^{adj}(\mathbf{k})}{\det|\Gamma(\mathbf{k})|} \quad (1.68)$$

To obtain a solution to the Green's tensor in the original form, we have to apply the inverse Fourier transformation:

$$G_{ik}(\mathbf{r}) = \frac{1}{(2\pi)^3} \int \frac{\Gamma_{ik}^{adj}(\mathbf{k})}{\det|\Gamma(\mathbf{k})|} \exp^{i\mathbf{k}\cdot\mathbf{r}} d\mathbf{k} \quad (1.69)$$

Integral equation (1.69) does not possess a trivial analytical solution. Therefore, there are several numerical techniques have been developed. One of the approaches is by transforming volume integral into a contour integral. However, to do so we first have to transform volume integral into a surface integral. The first step can be made by applying Radon transformation technique (Wang & Achenbach, 1995). We receive the following expression:

$$G_{ik}(\mathbf{r}) = \frac{1}{8\pi^2} \int \frac{\Gamma_{ik}^{adj}(\mathbf{k})}{\det|\Gamma(\mathbf{k})|} \delta(\mathbf{k} \cdot \mathbf{r}) dS(\mathbf{k}) \quad (1.70)$$

The next step is to transform surface integral into the contour integral. We consider spherical system of coordinates (Figure 1.7) of a unit sphere, meaning that the radius absolute value is equal to one.

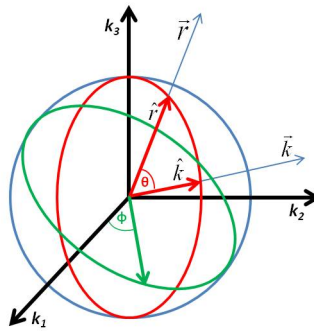


Figure 1.7: Spherical Coordinates

Surface element in a spherical coordinate system is represented in the following form:

$$dS(\hat{\mathbf{k}}) = |k|^2 \sin \theta d\theta d\phi \quad (1.71)$$

Here, $\hat{\mathbf{k}}$ is a unit vector, which is defined as a ratio of the actual vector \mathbf{k} to the absolute value $|k|$. Since we are in wave number domain, the value $|k|$ is equal to one. The dot product of two unit vectors, $\hat{\mathbf{k}}$ and $\hat{\mathbf{r}}$, is equal to $|k||r| \cos \theta$ (Figure 1.7), where $|k|$ and $|r|$ are equal to one.

Then:

$$d(\mathbf{k} \cdot \mathbf{r}) = -\sin \theta d\theta \quad (1.72)$$

$$dS(\hat{\mathbf{k}}) = -d(\hat{\mathbf{k}} \cdot \hat{\mathbf{r}})d\phi$$

Combining equation (1.70) with equation (1.72) and expressing it in terms of unit vectors, we receive:

$$G_{ik}(\mathbf{r}) = \frac{1}{8\pi^2} \int \frac{\Gamma_{ik}^{adj}(\hat{\mathbf{k}})}{\det|\Gamma(\hat{\mathbf{k}})|} \delta(|r|\hat{\mathbf{k}} \cdot \hat{\mathbf{r}}) d(\hat{\mathbf{k}} \cdot \hat{\mathbf{r}}) d\phi \quad (1.73)$$

Here, $|k|$ and $|r|$ are equal to one, however, we substitute only $|k|$ by one and keep $|r|$ in place in the Dirac's delta expression. Applying Dirac's delta scaling property for a non-zero scalar $|r|$, we transform our surface integral into contour integral:

$$G_{ik}(\mathbf{r}) = \frac{1}{8\pi^2|r|} \oint \frac{\Gamma_{ik}^{adj}(\hat{\mathbf{k}})}{\det|\Gamma(\hat{\mathbf{k}})|} d\phi(\hat{\mathbf{k}}) \quad (1.74)$$

Unit vector $\hat{\mathbf{k}}$ can be expressed through new parameter t (Sales & Gray, 1998) that

varies from 0 to 2π , and equation (1.74) changes to:

$$G_{ik}(\mathbf{r}) = \frac{1}{8\pi^2|r|} \int_0^{2\pi} \frac{\Gamma_{ik}^{adj}(\hat{\mathbf{k}}(t))}{\det|\Gamma(\hat{\mathbf{k}}(t))|} dt \quad (1.75)$$

The parametric equation of $\hat{\mathbf{k}}(t)$ for a unit circle has the following form:

$$\hat{\mathbf{k}}(t) = \begin{pmatrix} \sin(\phi) \cos(t) + \cos(\phi) \cos(\psi) \sin(t) \\ -\cos(\phi) \cos(t) + \sin(\phi) \cos(\psi) \sin(t) \\ -\sin(\psi) \sin(t) \end{pmatrix} \quad (1.76)$$

Here, ϕ is an azimuthal angle and ψ is a polar angle (1.8).

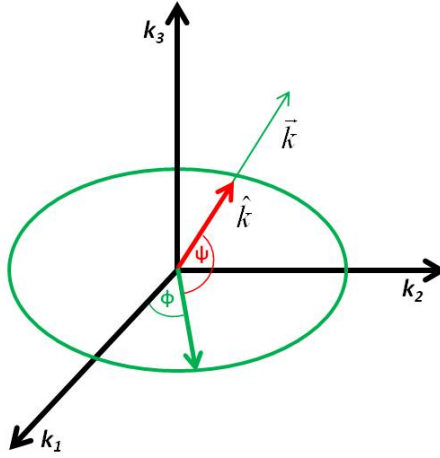


Figure 1.8: Terms of parametric equation in spherical system of coordinates

In order to evaluate integral equation (1.75), the integrand needs to be transformed into a rational function and the range of integration should be expanded (Sales & Gray, 1998). This transformation can be achieved by making following

substitution (Dederichs & Liebfried, 1969):

$$Z = \tan(t) \tag{1.77}$$

Combining equation (1.76) with equation (1.77), we receive:

$$\hat{\mathbf{k}} = \cos(t)s(Z),$$

$$s(Z) = \begin{pmatrix} \sin(\phi) + Z \cos(\phi) \cos(\psi) \\ -\cos(\phi) + Z \sin(\phi) \cos(\psi) \\ -Z \sin(\psi) \end{pmatrix} \tag{1.78}$$

Equation (1.75) then can be written as:

$$G_{ik}(\mathbf{r}) = \frac{1}{8\pi^2|r|} 2 \int_{-\infty}^{\infty} \frac{\cos^4(t)\Gamma_{ik}^{adj}(Z)}{\cos^6(t)\det|\Gamma(Z)|} d(t),$$

$$G_{ik}(\mathbf{r}) = \frac{1}{8\pi^2|r|} 2 \int_{-\infty}^{\infty} \frac{1}{\cos^2(t)} \frac{\Gamma_{ik}^{adj}(Z)}{\det|\Gamma(Z)|} d(t), \tag{1.79}$$

$$G_{ik}(\mathbf{r}) = \frac{1}{4\pi^2|r|} \int_{-\infty}^{\infty} \frac{\Gamma_{ik}^{adj}(Z)}{\det|\Gamma(Z)|} dZ$$

”The factor of 2 in equation (1.79) appears because the change of variables $Z = \tan(t)$ covers the range $(-\infty, \infty)$ twice in the interval $[0, 2\pi]$ ” (Sales & Gray, 1998). Integral equation (1.79) for an arbitrary anisotropic medium can be evaluated using different numerical techniques like Cauchy’s residues theorem (Sales & Gray, 1998; Phan et al., 2004). However, we use technical computing software Maple 14 to perform required

integration.

1.3.2 Correlation Tensor

Spatial correlation function technique has an advantage over simple averaging, VRH averaging or Eshelby's averaging techniques mainly due to its ability to consider elastic properties at micro-scale by studying fluctuation term. Like in the case of mentioned averaging techniques the PCA technique provides best results when the elastic properties of end-members of a composite material have small differences. The general theoretical introduction of PCA method and PCA technique for isotropic media have been described in subsection (1.2.2). In this subsection we extend theory further to the case of an anisotropic media. In this work we specifically concentrate on the elastic properties of the media of orthorhombic and hexagonal types of symmetry, however, this method is applicable to any type of symmetry.

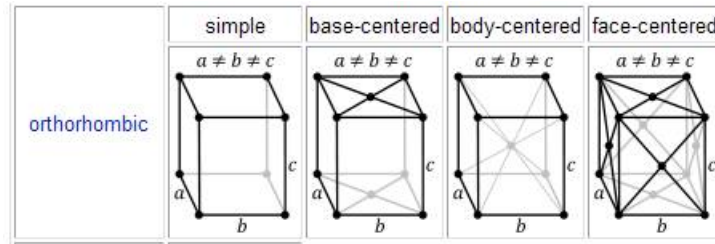


Figure 1.9: Orthorhombic crystal lattices (Prince, 2006)

Medium with orthorhombic type of symmetry is characterized by nine independent coefficients of elastic stiffness tensor. Introducing Voigt notations $[11 \rightarrow 1; 22 \rightarrow$

2; 33 \rightarrow 3; 23 \rightarrow 4; 13 \rightarrow 5; 12 \rightarrow 6], we can express all nine coefficients in the matrix form:

$$C_{ijkl} = \begin{pmatrix} C_{11} & C_{12} & C_{13} & 0 & 0 & 0 \\ C_{12} & C_{22} & C_{23} & 0 & 0 & 0 \\ C_{13} & C_{23} & C_{33} & 0 & 0 & 0 \\ 0 & 0 & 0 & C_{44} & 0 & 0 \\ 0 & 0 & 0 & 0 & C_{55} & 0 \\ 0 & 0 & 0 & 0 & 0 & C_{66} \end{pmatrix} \quad (1.80)$$

Effective elastic stiffness tensor consists of the stiffness tensor averaging term and the term responsible for fluctuation:

$$C_{ijnp}^* = \langle C_{ijnp} \rangle + \int G_{km,lq}(\mathbf{r} - \mathbf{r}_1) B_{mqnp}^{ijkl}(\mathbf{r} - \mathbf{r}_1) d\mathbf{r}_1 \quad (1.81)$$

Here, B_{pqrs}^{ijkl} is the correlation tensor and it is defined as:

$$\begin{aligned} \langle C'_{ijkl}(\mathbf{r}) C'_{pqrs}(\mathbf{r}_1) \rangle &= B_{pqrs}^{ijkl}(\mathbf{r} - \mathbf{r}_1) \\ \langle C'_{ijkl}(\mathbf{r} + \mathbf{r}_1) C'_{pqrs}(\mathbf{r}_1) \rangle &= B_{pqrs}^{ijkl}(\mathbf{r}) \end{aligned} \quad (1.82)$$

As it was shown by Shermergor (1977) all components of correlation tensor in this case have the same coordinate dependence. Therefore, correlation tensor can be

expressed through covariant tensor A_{pqrs}^{ijkl} as:

$$B_{pqrs}^{ijkl}(\mathbf{r}) = A_{pqrs}^{ijkl} \phi(\mathbf{r}) \quad (1.83)$$

$$\phi(0) = 1$$

Here, $\phi(\mathbf{r})$ is a unitless function that describes coordinate dependency, \mathbf{r} is a correlation radius, and A_{pqrs}^{ijkl} takes the following form:

$$A_{pqrs}^{ijkl} = \langle C'_{ijkl}(\mathbf{r}) C'_{pqrs}(\mathbf{r}) \rangle \quad (1.84)$$

Initially, we assume that correlation radius is infinitely small so we equate it to zero. Considering the Fourier image, the equation of effective stiffness tensor takes the following form:

$$C_{ijnp}^* = \langle C_{ijnp} \rangle + \frac{1}{8\pi^3} A_{mqnp}^{ijkl} \int G_{km,lq}(\mathbf{k}) d\mathbf{k} \quad (1.85)$$

where, $\phi(0) = 1$, $G_{km,lq}(\mathbf{k})$ is the Fourier image of the second derivative of Green's tensor. The comma sign between indices denotes differentiation.

Chapter 2

Practical Application

2.1 Data Description

Data that were used in this work are classified as those for theoretical modeling and those obtained through measurements in the laboratory. The theoretical model represents the medium which consists of matrix and gas inclusions. The matrix itself is composed of seventy percent of quartz minerals and thirty percent of illite minerals. Gas inclusions are represented by methane and its concentration varies from zero to ten percent. Usually clay minerals in the medium are not limited solely to illite, however, illite in our case is a dominating clay mineral and other clay minerals have very similar elastic properties, which allows us to combine all of the clay minerals under illite's properties. Data for these composites of the medium are shown in table (2.1) (Tiwary, 2007; Bayuk, Ammerman, & Chesnokov, 2007b; Katahara, 1996; Belikov, Alexandrov, & Ryzhova, 1970). This set of minerals and

Table 2.1: Properties of theoretical model composites

C_{ij} (GPa)	Quartz	Illite	Methane
C_{11}	86	179.9	0.000175
C_{12}	7.4	39.9	0.000175
C_{13}	11.91	14.5	0.000175
C_{14}	-18.04	0	0
C_{22}	86	179.9	0.000175
C_{23}	11.91	14.5	0.000175
C_{24}	18.04	0	0
C_{33}	105.75	55	0.000175
C_{44}	58.2	11.7	0
C_{55}	58.2	11.7	0
C_{56}	-18.04	0	0
C_{66}	39.3	70	0
$\rho(g/cc)$	2.65	2.7	0.0007

inclusion type were chosen based on the composition of the rock samples that were analyzed in the laboratory by the Institute of Applied and Theoretical Geophysics at University of Houston. Laboratory measurements were conducted on twelve rock samples taken from six different wells. However, theoretical model will be compared with samples from one well indicated as JR(III,IV), figure (2.1) (Chen, 2012). Data for this samples obtained through lab measurements are shown in table (2.2).

Table 2.2: Properties of Barnett Shale sample measured in the laboratory

Sample	Deg	V_P (km/sec)	V_{S1} (km/sec)	V_{S2} (km/sec)	$\rho(g/cc)$
JR (III, IV)	90	4.690	2.949	2.305	2.559
JR (III, IV)	0	4.477	2.815	2793	2.716
JR (III, IV)	45	5.238	3.362	3.018	2.714

Table 2.3: Properties of Barnett Shale sample calculated using lab data

Sample	C_{11}	C_{12}	C_{13}	C_{33}	C_{44}	C_{66}
JR (III, IV)	59.389	12.428	48.564	54.118	21.395	23.481

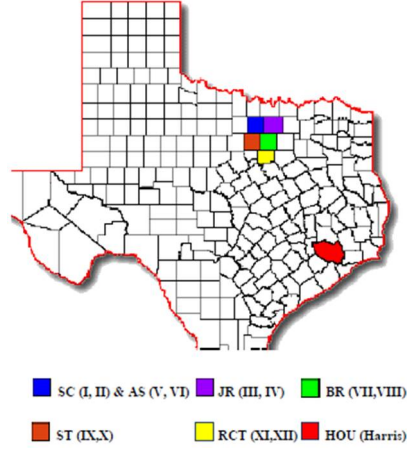


Figure 2.1: Location of Studied Well JR (III, IV) (Courtesy of Di Chen, 2012)

All the samples represent the Barnett Shale and they were taken at the depth from 5105 ft (1556 m) to 7830 ft (2387 m). Porosity has been reported to be over five percent. Elastic stiffness tensor values reported in the table (2.3) have been calculated based on the data obtained through laboratory measurements (2.2).

2.2 Green's Tensor

As it was mentioned in subsection (1.4.1), Green's tensor in the wave number domain can be found by evaluating inverse of the Green-Christoffel tensor. Then, applying Fourier transformation we obtained the following expression:

$$G_{ik}(\mathbf{r}) = \frac{1}{(2\pi)^3} \int \frac{\Gamma_{ik}^{adj}(\mathbf{k})}{\det|\Gamma(\mathbf{k})|} \exp^{i\mathbf{k}\mathbf{r}} d\mathbf{k} \quad (2.1)$$

It has also been demonstrated that volume integral can be expressed as a contour integral and the expression of Green's function became:

$$G_{ik}(\mathbf{r}) = \frac{1}{4\pi^2|r|} \int_{\infty}^{-\infty} \frac{\Gamma_{ik}^{adj}(Z)}{\det|\Gamma(Z)|} dZ \quad (2.2)$$

The Green-Christoffel tensor in this case is a function of Z and it is expressed as:

$$\Gamma_{ik}(Z) = C_{ijkl} s_j(Z) s_l(Z) \quad (2.3)$$

Here, $s_j(Z)$ is characterized by matrix equation (1.78), and expression for stiffness tensor in the case of the medium with orthorhombic type of symmetry in the laboratory system of coordinates has the form:

$$C_{ijkl} = \sum_{n=1}^3 [\lambda_n l_{in} l_{jn} l_{kn} l_{ln} + \mu_n (l_{in} l_{jn} \delta_{kl} + \delta_{ij} l_{kn} l_{ln}) + \nu_n (l_{in} \delta_{jk} l_{ln} + l_{jn} \delta_{ik} l_{ln} + l_{in} \delta_{jl} l_{kn} + l_{jn} \delta_{il} l_{kn})] \quad (2.4)$$

Here, l_{ij} is called direction-cosines tensor, and it's components have the following expression:

$$l_{mn} = \begin{pmatrix} \cos(\phi) \cos(\psi) \cos(\theta) - \sin(\phi) \sin(\theta) & -\cos(\phi) \sin(\theta) - \sin(\phi) \cos(\theta) \cos(\psi) & \sin(\psi) \cos(\theta) \\ \sin(\phi) \cos(\theta) + \cos(\phi) \sin(\theta) \cos(\psi) & -\cos(\psi) \sin(\phi) \sin(\theta) + \cos(\phi) \cos(\theta) & \sin(\psi) \sin(\theta) \\ -\cos(\phi) \sin(\psi) & \sin(\phi) \sin(\psi) & \cos(\psi) \end{pmatrix} \quad (2.5)$$

Here, for the orthorhombic type of symmetry the terms λ_n , μ_n , and ν_n are related to stiffness tensor values through the following expressions:

$$\begin{aligned}
\lambda_1 &= C_{11} + C_{23} + 2C_{44} - (C_{12} + C_{13} + 2C_{55} + 2C_{66}) \\
\lambda_2 &= C_{22} + C_{13} + 2C_{55} - (C_{12} + C_{23} + 2C_{44} + 2C_{66}) \\
\lambda_3 &= C_{33} + C_{12} + 2C_{66} - (C_{13} + C_{23} + 2C_{44} + 2C_{55}) \\
\mu_1 &= \frac{1}{2}(C_{12} + C_{13} - C_{23}); \quad \nu_1 = \frac{1}{2}(C_{55} + C_{66} - C_{44}) \\
\mu_2 &= \frac{1}{2}(C_{12} + C_{23} - C_{13}); \quad \nu_2 = \frac{1}{2}(C_{44} + C_{66} - C_{55}) \\
\mu_3 &= \frac{1}{2}(C_{13} + C_{23} - C_{12}); \quad \nu_3 = \frac{1}{2}(C_{44} + C_{55} - C_{66})
\end{aligned} \tag{2.6}$$

Therefore, combining equation (2.4) with equation (2.3), the Green-Christoffel tensor for the orthorhombic type of symmetry with Euler angles equal to zero becomes:

$$\begin{aligned}
\Gamma_{11} &= C_{11}(\sin(\theta) + Z \cos(\theta) \cos(\psi))^2 + C_{66}(-\cos(\theta) + Z \sin(\theta) \cos(\psi))^2 + C_{55}Z^2 \sin(\psi)^2 \\
\Gamma_{12} &= C_{12}(\sin(\theta) + Z \cos(\theta) \cos(\psi))(-\cos(\theta) + Z \sin(\theta) \cos(\psi)) + C_{66}(-\cos(\theta) + Z \sin(\theta) \cos(\psi))(\sin(\theta) + Z \cos(\theta) \cos(\psi)) \\
\Gamma_{13} &= -C_{13}(\sin(\theta) + Z \cos(\theta) \cos(\psi))Z \sin(\psi) - C_{55}Z \sin(\psi)(\sin(\theta) + Z \cos(\theta) \cos(\psi)) \\
\Gamma_{21} &= C_{12}(\sin(\theta) + Z \cos(\theta) \cos(\psi))(-\cos(\theta) + Z \sin(\theta) \cos(\psi)) + C_{66}(-\cos(\theta) + Z \sin(\theta) \cos(\psi))(\sin(\theta) + Z \cos(\theta) \cos(\psi)) \\
\Gamma_{22} &= C_{66}(\sin(\theta) + Z \cos(\theta) \cos(\psi))^2 + C_{22}(-\cos(\theta) + Z \sin(\theta) \cos(\psi))^2 + C_{44}Z^2 \sin(\psi)^2 \\
\Gamma_{23} &= -C_{23}(-\cos(\theta) + Z \sin(\theta) \cos(\psi))Z \sin(\psi) - C_{44}Z \sin(\psi)(-\cos(\theta) + Z \sin(\theta) \cos(\psi)) \\
\Gamma_{31} &= -C_{13}(\sin(\theta) + Z \cos(\theta) \cos(\psi))Z \sin(\psi) - C_{55}Z \sin(\psi)(\sin(\theta) + Z \cos(\theta) \cos(\psi)) \\
\Gamma_{32} &= -C_{23}(-\cos(\theta) + Z \sin(\theta) \cos(\psi))Z \sin(\psi) - C_{44}Z \sin(\psi)(-\cos(\theta) + Z \sin(\theta) \cos(\psi)) \\
\Gamma_{33} &= C_{55}(\sin(\theta) + Z \cos(\theta) \cos(\psi))^2 + C_{44}(-\cos(\theta) + Z \sin(\theta) \cos(\psi))^2 + (C_{33} + 2C_{55} - 2C_{66})Z^2 \sin(\psi)^2
\end{aligned} \tag{2.7}$$

The terms λ_n , μ_n , and ν_n in the case of the medium of hexagonal type of symmetry take the form:

$$\begin{aligned}
\lambda_1 &= 0; \quad \lambda_2 = 0; \quad \lambda_3 = C_{11} + C_{33} - 2(C_{13} + 2C_{44}) \\
\mu_1 &= \frac{1}{2}C_{12}; \quad \mu_2 = \frac{1}{2}C_{12}; \quad \mu_3 = \frac{1}{2}(2C_{13} - C_{12}) \\
\nu_1 &= \frac{1}{4}(C_{11} - C_{12}); \quad \nu_2 = \frac{1}{4}(C_{11} - C_{12}) \\
\nu_3 &= \frac{1}{4}(4C_{44} + C_{12} - C_{11})
\end{aligned} \tag{2.8}$$

Following the same procedure as in the case of orthorhombic symmetry, we obtain expressions for Green-Christoffel tensor components:

$$\begin{aligned}
\Gamma_{11} &= C_{11}(\sin(\theta) + Z \cos(\theta) \cos(\psi))^2 + (\frac{1}{2}C_{11} - \frac{1}{2}C_{12})(-\cos(\theta) + Z \sin(\theta) \cos(\psi))^2 + C_{44}Z^2 \sin(\psi)^2 \\
\Gamma_{12} &= C_{12}(\sin(\theta) + Z \cos(\theta) \cos(\psi))(-\cos(\theta) + Z \sin(\theta) \cos(\psi)) + (\frac{1}{2}C_{11} - \frac{1}{2}C_{12})(-\cos(\theta) + Z \sin(\theta) \cos(\psi))(\sin(\theta) + Z \cos(\theta) \cos(\psi)) \\
\Gamma_{13} &= -C_{13}(\sin(\theta) + Z \cos(\theta) \cos(\psi))Z \sin(\psi) - C_{44}Z \sin(\psi)(\sin(\theta) + Z \cos(\theta) \cos(\psi)) \\
\Gamma_{21} &= C_{12}(\sin(\theta) + Z \cos(\theta) \cos(\psi))(-\cos(\theta) + Z \sin(\theta) \cos(\psi)) + (\frac{1}{2}C_{11} - \frac{1}{2}C_{12})(-\cos(\theta) + Z \sin(\theta) \cos(\psi))(\sin(\theta) + Z \cos(\theta) \cos(\psi)) \\
\Gamma_{22} &= (\frac{1}{2}C_{11} - \frac{1}{2}C_{12})(\sin(\theta) + Z \cos(\theta) \cos(\psi))^2 + C_{11}(-\cos(\theta) + Z \sin(\theta) \cos(\psi))^2 + C_{44}Z^2 \sin(\psi)^2 \\
\Gamma_{23} &= -C_{23}(-\cos(\theta) + Z \sin(\theta) \cos(\psi))Z \sin(\psi) - C_{44}Z \sin(\psi)(-\cos(\theta) + Z \sin(\theta) \cos(\psi)) \\
\Gamma_{31} &= -C_{13}(\sin(\theta) + Z \cos(\theta) \cos(\psi))Z \sin(\psi) - C_{44}Z \sin(\psi)(\sin(\theta) + Z \cos(\theta) \cos(\psi)) \\
\Gamma_{32} &= -C_{23}(-\cos(\theta) + Z \sin(\theta) \cos(\psi))Z \sin(\psi) - C_{44}Z \sin(\psi)(-\cos(\theta) + Z \sin(\theta) \cos(\psi)) \\
\Gamma_{33} &= C_{44}(\sin(\theta) + Z \cos(\theta) \cos(\psi))^2 + C_{44}(-\cos(\theta) + Z \sin(\theta) \cos(\psi))^2 + C_{33}Z^2 \sin(\psi)^2
\end{aligned} \tag{2.9}$$

The terms λ_n , μ_n , and ν_n in the case of an isotropic medium take the form:

$$\begin{aligned}
\lambda_1 &= 0; \quad \lambda_2 = 0; \quad \lambda_3 = 0 \\
\mu_1 &= \frac{1}{2}C_{12}; \quad \mu_2 = \frac{1}{2}C_{12}; \quad \mu_3 = \frac{1}{2}C_{12} \\
\nu_1 &= \frac{1}{4}(C_{11} - C_{12}); \quad \nu_2 = \frac{1}{4}(C_{11} - C_{12}); \quad \nu_3 = \frac{1}{4}(C_{11} - C_{12})
\end{aligned} \tag{2.10}$$

The Green-Christoffel tensor components for isotropic medium then:

$$\begin{aligned}
\Gamma_{11} &= C_{11}(\sin(\theta) + Z \cos(\theta) \cos(\psi))^2 + (\frac{1}{2}C_{11} - \frac{1}{2}C_{12})(-\cos(\theta) + Z \sin(\theta) \cos(\psi))^2 + (\frac{1}{2}C_{11} - \frac{1}{2}C_{12})Z^2 \sin(\psi)^2 \\
\Gamma_{12} &= C_{12}(\sin(\theta) + Z \cos(\theta) \cos(\psi))(-\cos(\theta) + Z \sin(\theta) \cos(\psi)) + (\frac{1}{2}C_{11} - \frac{1}{2}C_{12})(-\cos(\theta) + Z \sin(\theta) \cos(\psi))(\sin(\theta) + Z \cos(\theta) \cos(\psi)) \\
\Gamma_{13} &= -C_{12}(\sin(\theta) + Z \cos(\theta) \cos(\psi))Z \sin(\psi) - (\frac{1}{2}C_{11} - \frac{1}{2}C_{12})Z \sin(\psi)(\sin(\theta) + Z \cos(\theta) \cos(\psi)) \\
\Gamma_{21} &= C_{12}(\sin(\theta) + Z \cos(\theta) \cos(\psi))(-\cos(\theta) + Z \sin(\theta) \cos(\psi)) + (\frac{1}{2}C_{11} - \frac{1}{2}C_{12})(-\cos(\theta) + Z \sin(\theta) \cos(\psi))(\sin(\theta) + Z \cos(\theta) \cos(\psi)) \\
\Gamma_{22} &= (\frac{1}{2}C_{11} - \frac{1}{2}C_{12})(\sin(\theta) + Z \cos(\theta) \cos(\psi))^2 + C_{11}(-\cos(\theta) + Z \sin(\theta) \cos(\psi))^2 + (\frac{1}{2}C_{11} - \frac{1}{2}C_{12})Z^2 \sin(\psi)^2 \\
\Gamma_{23} &= -C_{12}(-\cos(\theta) + Z \sin(\theta) \cos(\psi))Z \sin(\psi) - (\frac{1}{2}C_{11} - \frac{1}{2}C_{12})Z \sin(\psi)(-\cos(\theta) + Z \sin(\theta) \cos(\psi)) \\
\Gamma_{31} &= -C_{12}(\sin(\theta) + Z \cos(\theta) \cos(\psi))Z \sin(\psi) - (\frac{1}{2}C_{11} - \frac{1}{2}C_{12})Z \sin(\psi)(\sin(\theta) + Z \cos(\theta) \cos(\psi)) \\
\Gamma_{32} &= -C_{12}(-\cos(\theta) + Z \sin(\theta) \cos(\psi))Z \sin(\psi) - (\frac{1}{2}C_{11} - \frac{1}{2}C_{12})Z \sin(\psi)(-\cos(\theta) + Z \sin(\theta) \cos(\psi)) \\
\Gamma_{33} &= (\frac{1}{2}C_{11} - \frac{1}{2}C_{12})(\sin(\theta) + Z \cos(\theta) \cos(\psi))^2 + (\frac{1}{2}C_{11} - \frac{1}{2}C_{12})(-\cos(\theta) + Z \sin(\theta) \cos(\psi))^2 + C_{11}Z^2 \sin(\psi)^2
\end{aligned} \tag{2.11}$$

The expressions for Γ_{ik}^{adj} and $det|\Gamma|$ for different media are obtained using computational software Maple14, and are too big to fit in one page. Solving the integral equations with respect to Z we receive the expression for Green's function in the medium of described above types of symmetry. However, we also need to calculate

the first and second derivatives of Green's function. These derivatives are to be taken with respect to the angles ϕ and ψ . The equation of the first derivative of Green's function then becomes:

$$\frac{\partial}{\partial \phi} G_{ik} = \frac{1}{4\pi^2|r|} \int_{-\infty}^{\infty} \frac{\partial}{\partial \phi} \frac{\Gamma_{ik}^{adj}(Z)}{\det|\Gamma(Z)|} dZ \quad (2.12)$$

The equation of the second derivative of Green's function then becomes:

$$\frac{\partial^2}{\partial \phi \partial \psi} G_{ik} = \frac{1}{4\pi^2|r|} \int_{-\infty}^{\infty} \frac{\partial^2}{\partial \phi \partial \psi} \frac{\Gamma_{ik}^{adj}(Z)}{\det|\Gamma(Z)|} dZ \quad (2.13)$$

The computation of the integral of the second derivative of the inverse of Green-Christoffel tensor requires the calculation of the sixth degree polynomial equation and is performed numerically using the software Maple14.

2.3 Applications of Averaging Techniques

This section consists of four subsections that show practical implication of mentioned earlier averaging techniques. First two subsections describe application of VRH technique for single-phase and multi-phase polycrystalline media. For each case VRH technique has quite different formulation. The third subsection describes the practical use of Eshelby's method for isotropic and anisotropic media. The last subsection compares two techniques highlighting their advantages and limitations.

2.3.1 VRH. Single-phase Polycrystalline Media

In this section we express the application of Voigt-Reuss-Hill method to isotropic and anisotropic media. Averaging is represented arithmetically through integration by volume:

$$\langle C_{ijkl} \rangle = \frac{1}{V} \iiint C_{ijkl} F(V) dV \quad (2.14)$$

Here, angular brackets denote averaging, V is a volume, C_{ijkl} is the elastic stiffness tensor in laboratory system of coordinates, and $F(V)$ is a distribution function. Wave propagating through continuum polycrystalline media has to have the wavelength longer than the grain size; otherwise this averaging technique might not be applicable. The Voigt approximation shows that average value of the stiffness tensor can be obtained from effective stiffness tensor, since the fluctuating component of strain is equal to zero. In this case only stress will contain fluctuating component. The goal is to calculate average values of stiffness and compliance tensors for isotropic and anisotropic media, considering that elastic constants of each crystal in our polycrystalline body are known. Several methods exist for the calculation of elastic parameters. Using the Voigt-Reuss-Hill model we calculate elastic constants for isotropic and homogeneous polycrystalline media, and then choosing appropriate distribution function, we find elastic constants for anisotropic media. Crystallographic system of coordinates is characterized by Euler angles (ϕ, ψ, θ) , figure 2.2.

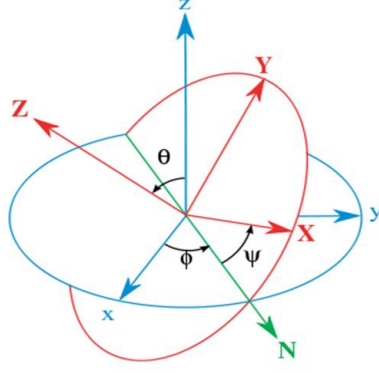


Figure 2.2: Euler angles

For polycrystalline media the equation in the case of random orientation of crystals:

$$C_{ijkl} = l_{ip}l_{jq}l_{kr}l_{ls}C''_{pqrs} \quad (2.15)$$

where, C''_{pqrs} is a stiffness tensor of crystals in crystallographic system of coordinates; $l_{ip}l_{jq}l_{kr}l_{ls}$ are the direction cosines that represent Euler angles of showing minerals orientations:

$$l_{mn} = \begin{pmatrix} \cos(\phi) \cos(\psi) \cos(\theta) - \sin(\phi) \sin(\theta) & -\cos(\phi) \sin(\theta) - \sin(\phi) \cos(\theta) \cos(\psi) & \sin(\psi) \cos(\theta) \\ \sin(\phi) \cos(\theta) + \cos(\phi) \sin(\theta) \cos(\psi) & -\cos(\psi) \sin(\phi) \sin(\theta) + \cos(\phi) \cos(\theta) & \sin(\psi) \sin(\theta) \\ -\cos(\phi) \sin(\psi) & \sin(\phi) \sin(\psi) & \cos(\psi) \end{pmatrix} \quad (2.16)$$

When we are solving for isotropic medium, the distribution function has to be constant, $F(V) = \text{const.}$, and volume $V = \sin \phi d\phi d\psi d\theta$. Therefore, our final equation

takes the form:

$$\langle C_{ijkl} \rangle = \frac{\iiint C''_{ijkl}(\phi, \psi, \theta) \sin \phi d\phi d\psi d\theta}{\iiint \sin \phi d\phi d\psi d\theta} = \frac{1}{8\pi^2} \iiint C''_{ijkl}(\phi, \psi, \theta) \sin \phi d\phi d\psi d\theta \quad (2.17)$$

The same technique is applied in the case of Reuss approximation, where calculating the average elastic constants, we consider media without stress fluctuation. Hence, the equation for average compliance tensor will look like:

$$\langle S_{ijkl} \rangle = \frac{\iiint S''_{ijkl}(\phi, \psi, \theta) \sin \phi d\phi d\psi d\theta}{\iiint \sin \phi d\phi d\psi d\theta} = \frac{1}{8\pi^2} \iiint S''_{ijkl}(\phi, \psi, \theta) \sin \phi d\phi d\psi d\theta \quad (2.18)$$

To calculate elastic constants for an anisotropic media we have to consider the distribution function of crystal axes. The distribution function in this case depends only on Euler angles:

$$\langle C_{ijkl} \rangle = \frac{\iiint C''_{ijkl}(\phi, \psi, \theta) F(\phi, \psi, \theta) \sin \phi d\phi d\psi d\theta}{\iiint F(\phi, \psi, \theta) \sin \phi d\phi d\psi d\theta} \quad (2.19)$$

One of those distribution functions that we apply is a Dirac's delta function:

$$\int_{-\infty}^{\infty} \delta(\mathbf{x}) d\mathbf{x} = 1; \quad \delta(\mathbf{x}) = \begin{cases} \infty, & \mathbf{x} = 0 \\ 0, & \mathbf{x} \neq 0 \end{cases} \quad (2.20)$$

Therefore, the distribution function will take the form: $F(\phi, \psi, \theta) = \delta(\phi - \phi_0) f(\psi, \theta)$, where $f(\psi, \theta)$ is a constant value. This is an example of distribution over one angle,

meaning that only one angle is controlled, and other two angles can acquire random values. Introducing the delta (δ) function into equation (2.19), we receive:

$$\langle C_{ijkl} \rangle = \frac{\iiint C''_{ijkl}(\phi, \psi, \theta) \delta(\phi - \phi_0) \sin \phi d\phi d\psi d\theta}{\iiint \delta(\phi - \phi_0) \sin \phi d\phi d\psi d\theta} \quad (2.21)$$

Solving equation (2.21) we find the averaged elastic stiffness moduli for anisotropic medium of hexagonal type of symmetry. Therefore, by introducing delta functions that control the other two angles, we will receive the averaged value of elastic stiffness tensor for anisotropic media of orthorhombic type of symmetry:

$$\langle C_{ijkl} \rangle = \frac{\iiint C''_{ijkl}(\phi, \psi, \theta) \delta(\phi - \phi_0) \delta(\psi - \psi_0) \delta(\theta - \theta_0) \sin \phi d\phi d\psi d\theta}{\iiint \delta(\phi - \phi_0) \delta(\psi - \psi_0) \delta(\theta - \theta_0) \sin \phi d\phi d\psi d\theta} \quad (2.22)$$

2.3.2 VRH. Multi-phase Polycrystalline Media

This subsection describes the application of Voigt-Reuss-Hill (VRH) averaging technique to the medium that consists of multiple phases. Application of the distribution function in this averaging technique allows us to take into consideration different scenarios: isotropic medium composed of isotropic solid phases, isotropic media composed of anisotropic solid phases, anisotropic media composed of isotropic solid phases, anisotropic medium composed of anisotropic solid phases, and isotropic or anisotropic media composed of isotropic or anisotropic solid phases that also contains liquid inclusions. Below, we demonstrate the Voigt isostrain scheme, meaning that under applied stress, all phases are assumed to have the same strain, and that elastic

properties are described in terms of elastic stiffness tensor. The limitation of this method is that it considers only the volume fraction and elastic properties of each component, and does not take into consideration geometry of each phase. Therefore, we are unable to observe the variations of elastic properties with the variations of the shapes of all phases and their orientations. The model of the medium consists of three different material: quartz, illite-rich clay, and liquid inclusion. At first, we consider only solid composition, which is 70 percent of quartz and 30 percent of illite-rich clay. Then, we introduce liquid inclusion, which is methane gas, and its composition goes up to 10 percent, evenly reducing the composition of quartz and illite-rich clay, meaning that having 10 percent of methane we will have 65 percent of quartz and 25 percent of illite-rich clay in the medium.

First, we consider simple case when the medium is isotropic with isotropic inclusions, figure (2.3).

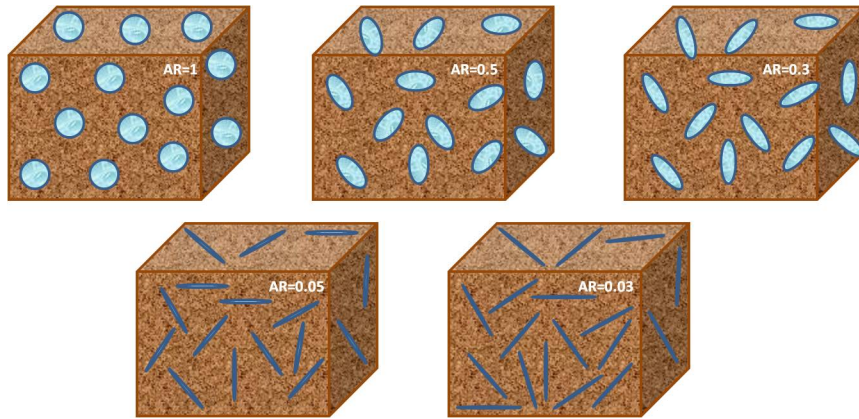


Figure 2.3: Isotropic medium with inclusions

We know that quartz is of trigonal symmetry system and illite-rich clay is of

hexagonal symmetry system. Therefore, in order to obtain isotropic medium VRH averaging should be applied in two steps: a) averaging over crystallographic axis of each mineral using equation (2.19) described in subsection (2.3.1); b) volume weighted averaging over all phases of the medium, using the following equation:

$$C_{ijkl} = \sum_{\alpha} X_{\alpha} \langle C_{ijkl}^{\alpha} \rangle \quad (2.23)$$

Here, α indicates the number of constituents, X_{α} is a volume fraction of the phase α , and $\langle C_{ijkl}^{\alpha} \rangle$ is the stiffness tensor value of the component α averaged over crystallographic axis. Even though we have media with inclusions of different shape and orientation, the VRH method is not affected by their geometrical arrangement.

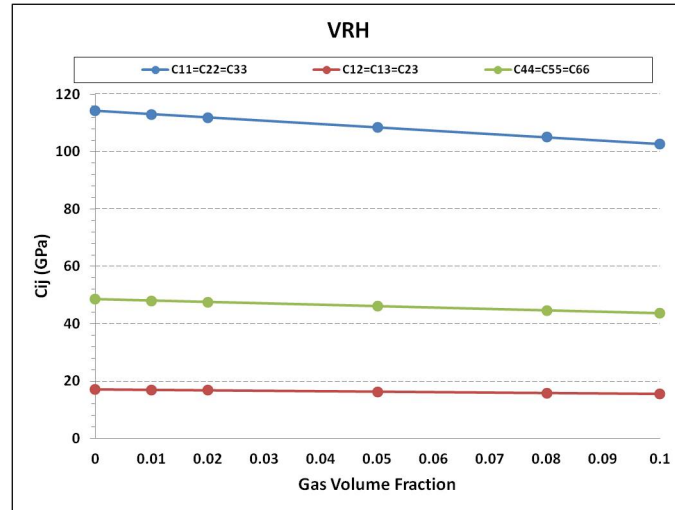


Figure 2.4: Variation of stiffness tensor with gas content (VRH Isotropic)

Stiffness tensor values show a linear decrease as the gas volume concentration increases. The gas content does not exceed 10 percent; however stiffness of gas is up

to six orders of magnitude lower than solid. That is why we observe decrease in effective elastic stiffness values. Data from the figure (2.4) are shown in table (2.4).

Table 2.4: Variation of stiffness tensor with gas content (VRH Isotropic)

Gas Fraction	C_{11}	C_{12}	C_{44}	ρ
0	114.17	17.15	48.51	2.665
0.01	113.028	16.979	48.025	2.638
0.02	111.887	16.807	47.539	2.612
0.05	108.462	16.293	46.085	2.532
0.08	105.036	15.778	44.629	2.452
0.1	102.753	15.435	43.659	2.399

Based on the elastic stiffness tensor and density values, velocities have been calculated as a function of gas volume fraction. As it is shown on the figure (2.5), velocities show similar behavior, meaning that they are not affected by the geometrical arrangement of inclusions and demonstrate a linear decrease as the gas content increases. Data from the figure (2.5) are shown in table (2.5).

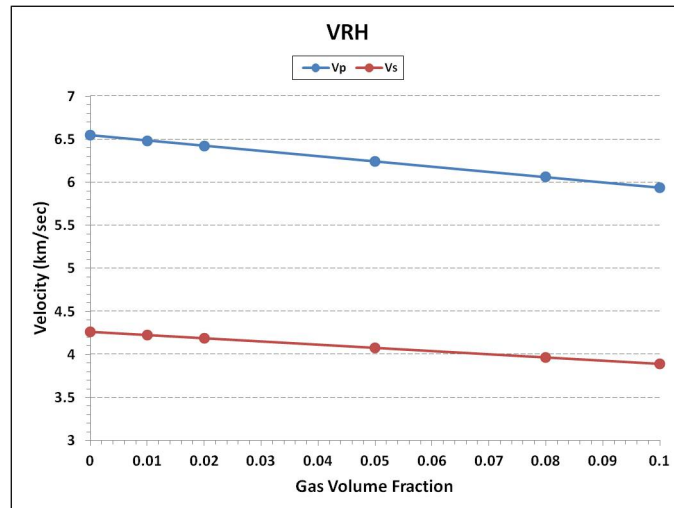


Figure 2.5: Variation of velocities with gas content (VRH Isotropic)

Table 2.5: Variation of velocities with gas content (VRH Isotropic)

Gas Fraction	V_p (km/sec)	V_s (km/sec)
0	6.545	4.266
0.01	6.484	4.229
0.02	6.424	4.191
0.05	6.243	4.078
0.08	6.062	3.965
0.1	5.941	3.889

In the case of anisotropy we consider medium to be of hexagonal type of symmetry that contains isotropic liquid inclusions, figure (2.6). In this case we need to do averaging over the crystallographic axis only for quartz mineral using equation (2.21) to transform it from trigonal to hexagonal type of symmetry. There is no need to do crystallographic rotation for illite since this mineral has hexagonal symmetry.

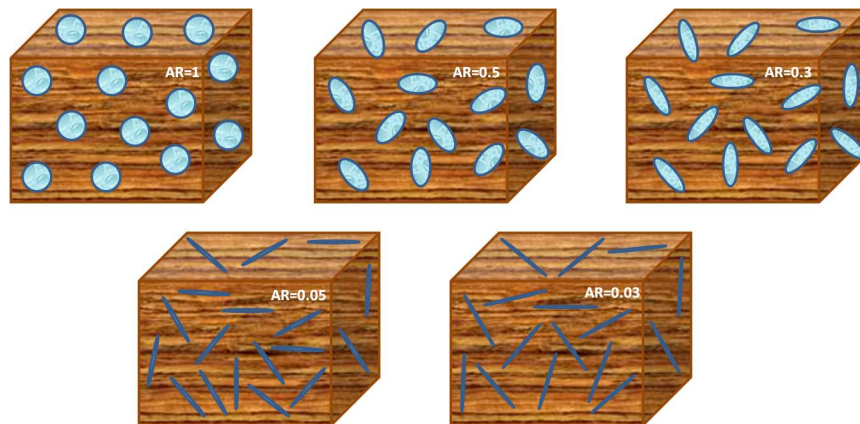


Figure 2.6: Anisotropic media with inclusions

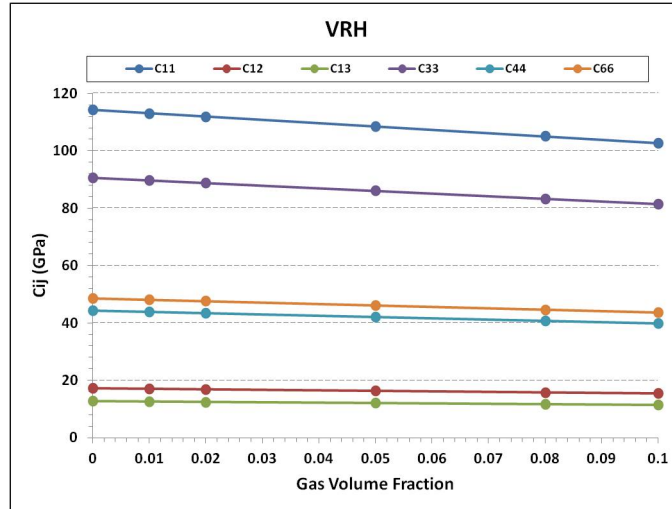


Figure 2.7: Variation of stiffness tensor with gas content (VRH Anisotropic)

Table 2.6: Variation of stiffness tensor with gas content (VRH Anisotropic)

Gas Fraction	C ₁₁	C ₁₂	C ₁₃	C ₃₃	C ₄₄	C ₆₆	ρ
0	114.17	17.15	12.687	90.525	44.25	48.51	2.665
0.01	113.028	16.979	12.560	89.619	43.808	48.024	2.638
0.02	111.887	16.807	12.433	88.715	43.365	47.539	2.612
0.05	108.462	16.293	12.053	85.999	42.038	46.085	2.532
0.08	105.036	15.778	11.672	83.283	40.71	44.629	2.452
0.1	102.753	15.435	11.418	81.473	39.825	43.659	2.399

As in the case of isotropic medium with inclusions, the elastic properties of anisotropic medium are invariant with variation of shape and orientation of inclusions, figure (2.7). Table (2.6) shows the data based on which figure (2.7) was constructed. In this case we analyze five independent parameters of stiffness tensor. All five parameters show a linear decrease as gas content increases. Velocities behavior with the variation of gas saturation are shown in figure (2.8). As gas saturation increases from zero to ten percent, we observe a linear decrease in velocities of

about nine percent. Velocities are invariant to the change in shape and orientation of inclusions.

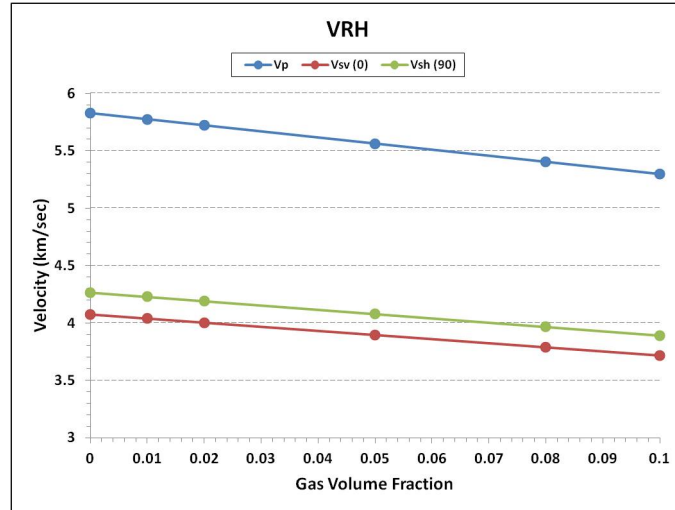


Figure 2.8: Variation of velocities with gas content (VRH Anisotropic)

Table 2.7: Variation of velocities with gas content (VRH Anisotropic)

Gas Fraction	V_P (km/sec)	V_{SV} (km/sec)	V_{SH} (km/sec)
0	5.828	4.075	4.266
0.01	5.775	4.039	4.229
0.02	5.722	4.003	4.191
0.05	5.562	3.896	4.078
0.08	5.402	3.789	3.965
0.1	5.295	3.717	3.889

From the calculated velocities results we clearly observe in both isotropic and anisotropic cases variations with increase of gas saturation. This behavior might be explained by observing variation of elastic stiffness tensor values and density values. As the gas saturation increases, the stiffness tensor values decrease at higher rates than density.

2.3.3 Eshelby's Method

In this section we show the solution for elastic stiffness tensor that was first reported by Eshelby. To do so we need to consider energy of the body, i.e. we need to know what happens with energy of the body that is affected by surface stress, and some part of it has been changed and represents different elastic constants. If only surface stress is applied, the change of energy is equal to negative value of internal energy $\Delta E = -E_{int}$, and the negative value defines the direction in which stress is applied. If our deformation field is constant, then: $\Delta E = E_{int}$. In both cases:

$$E_{int} = -\frac{1}{2}V_{inc}\sigma_{ij}^A\epsilon_{ij}^T \quad (2.24)$$

V_{inc} is a volume of inclusion. The energy of a unit volume considering effective elastic constants is equal to:

$$\frac{1}{2}C_{ijkl}^*\epsilon_{ij}^A\epsilon_{kl}^A = \frac{1}{2}S_{ijkl}^*\sigma_{ij}^A\sigma_{kl}^A \quad (2.25)$$

If our media consist of N inclusions, then the energy of the body will be equal to $E_0 + \Sigma_N E_{inc}$, where E_0 is the energy of the body without inclusion. For the total representative volume (whole medium) with N inclusions, our equation takes the following form (R is a number of inclusion):

$$\frac{1}{2}V_{rep}C_{ijkl}^*\epsilon_{ij}^A\epsilon_{kl}^A = \frac{1}{2}V_{rep}C_{ijkl}^M\epsilon_{ij}^A\epsilon_{kl}^A - \frac{1}{2}\sum_{R=1}^N(V_{inc}^R C_{ijkl}^M\epsilon_{ij}^A(\epsilon_{kl}^T)_R) \quad (2.26)$$

This method is called Eshelby-1. Finally, if we break down all inclusion into groups with the same volume, and represent each inclusion in terms of shape and orientation, we will receive:

$$C_{ijkl}^* \epsilon_{ij}^A \epsilon_{kl}^A = C_{ijkl}^M \epsilon_{ij}^A \epsilon_{kl}^A - C_{ijkl}^M \epsilon_{ij}^A \sum_{P=1}^K V_P \int_{\alpha_1} \int_{\alpha_2} \int_0^\pi \int_0^{2\pi} f_P(\phi, \psi, \theta, \alpha_1, \alpha_2) [\epsilon_{kl}^T(\phi, \psi, \theta, \alpha_1, \alpha_2)]_P \sin \phi d\phi d\psi d\theta d\alpha_1 d\alpha_2 \quad (2.27)$$

V_P is a volume concentration of inclusions of group P , K is a number of groups, and f_P is a distribution function of inclusions of group P in terms of orientation and shape characterized by aspect parameters. Effective elastic properties can also be represented through compliance tensor (Eshelby-2):

$$\frac{1}{2} V_{rep} S_{ijkl}^* \sigma_{ij}^A \sigma_{kl}^A = \frac{1}{2} V_{rep} S_{ijkl}^M \sigma_{ij}^A \sigma_{kl}^A - \frac{1}{2} \sum_{R=1}^N (V_{inc}^R S_{ijkl}^M \sigma_{ij}^A (\sigma_{kl}^T)_R) \quad (2.28)$$

Therefore, in analogous way we can find the elastic compliance tensor:

$$S_{ijkl}^* \sigma_{ij}^A \sigma_{kl}^A = S_{ijkl}^M \sigma_{ij}^A \sigma_{kl}^A - S_{ijkl}^M \sigma_{ij}^A \sum_{P=1}^K V_P \int_{\alpha_1} \int_{\alpha_2} \int_0^\pi \int_0^{2\pi} f_P(\phi, \psi, \theta, \alpha_1, \alpha_2) [\sigma_{kl}^T(\phi, \psi, \theta, \alpha_1, \alpha_2)]_P \sin \phi d\phi d\psi d\theta d\alpha_1 d\alpha_2 \quad (2.29)$$

Eshelby's method can be applied for both isotropic and anisotropic porous and fractured media. Pores and fractures of the media can have different shape and orientation and have to be isolated. The amount of pores and fractures should be small. Below, we present results of calculations that were made on exactly the same model as VRH calculations. In the case of isotropy both minerals and inclusions are randomly oriented. Figure (2.9) along with tables (2.8), (2.9) and (2.10) show results

of calculation using Eshelby's method for three media of the same composition, but with different geometries of inclusions. Inclusion shapes are specified by aspect ratio.

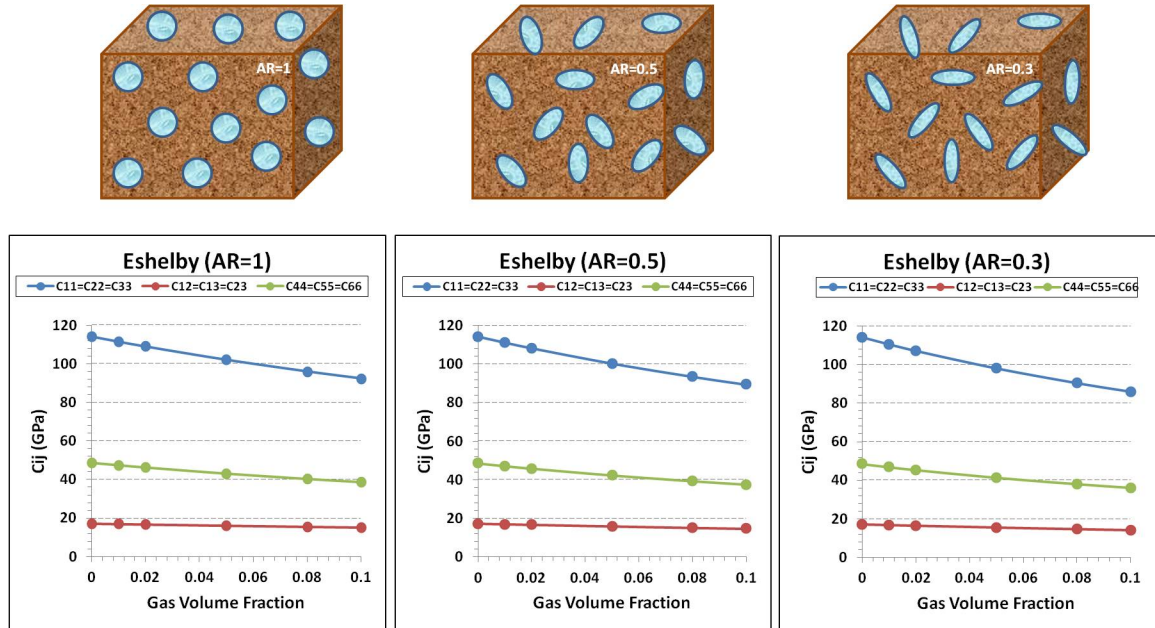


Figure 2.9: Variation of stiffness with gas content for high AR (Eshelby Isotropic)

These calculations were made using the Eshelby-2 method. The Eshelby-2 method calculates elastic compliance tensor and then transforms it to elastic stiffness tensor. Analyzing received results (inclusions aspect ratios of 1, 0.5, and 0.3) we may clearly observe the decrease of stiffness tensor values as gas saturation increases, and the variation of inclusion's shape or aspect ratios affects stiffness tensor dramatically.

Results of calculations for the media with inclusions of lower aspect ratios show even higher rates of decrease in stiffness tensor values and are presented in figure (2.10). It is also observed that, unlike in VRH averaging technique, the behavior of stiffness tensor values computed using Eshelby's method is slightly non-linear.

Table 2.8: Stiffness tensor vs. gas content. Aspect ratio is 1 (Eshelby Isotropic)

Gas Fraction	C_{11}	C_{12}	C_{44}	ρ
0	114.17	17.15	48.51	2.665
0.01	111.532	16.93	47.301	2.638
0.02	109.014	16.713	46.15	2.612
0.05	102.102	16.078	43.012	2.532
0.08	96.02	15.473	40.274	2.452
0.1	92.355	15.087	38.634	2.399

Table 2.9: Stiffness tensor vs. gas content. Aspect ratio is 0.5 (Eshelby Isotropic)

Gas Fraction	C_{11}	C_{12}	C_{44}	ρ
0	114.17	17.15	48.51	2.665
0.01	111.093	16.878	47.107	2.638
0.02	108.179	16.612	45.784	2.612
0.05	100.291	15.844	42.224	2.532
0.08	93.481	15.126	39.178	2.452
0.1	89.435	14.675	37.38	2.399

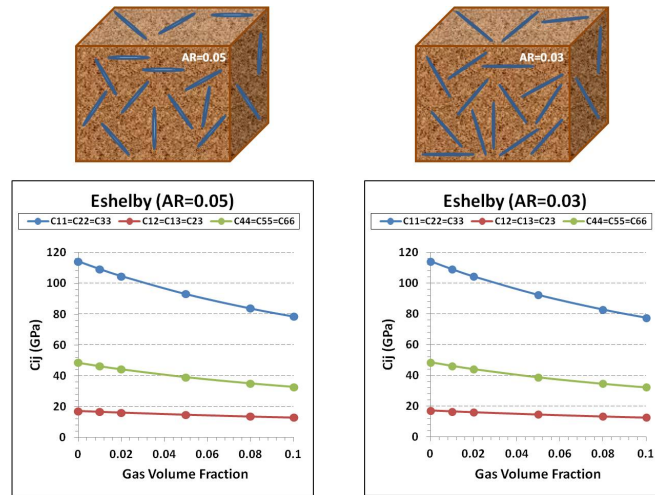


Figure 2.10: Variation of stiffness with gas content for low AR (Eshelby Isotropic)

Table 2.10: Stiffness tensor vs. gas content. Aspect ratio is 0.3 (Eshelby Isotropic)

Gas Fraction	C_{11}	C_{12}	C_{44}	ρ
0	114.17	17.15	48.51	2.665
0.01	110.529	16.801	46.864	2.638
0.02	107.114	16.461	45.326	2.612
0.05	98.033	15.505	41.264	2.532
0.08	90.376	14.636	37.87	2.452
0.1	85.906	14.103	35.901	2.399

Table 2.11: Stiffness tensor vs. gas content. AR is 0.05 (Eshelby Isotropic)

Gas Fraction	C_{11}	C_{12}	C_{44}	ρ
0	114.17	17.15	48.51	2.665
0.01	109.207	16.621	46.293	2.638
0.02	104.659	16.12	44.27	2.612
0.05	93.041	14.764	39.138	2.532
0.08	83.749	13.603	35.073	2.452
0.1	78.522	12.92	32.801	2.399

Table 2.12: Stiffness tensor vs. gas content. AR is 0.03 (Eshelby Isotropic)

Gas Fraction	C_{11}	C_{12}	C_{44}	ρ
0	114.17	17.15	48.51	2.665
0.01	109.02	16.595	46.212	2.638
0.02	104.315	16.071	44.122	2.612
0.05	92.364	14.662	38.851	2.532
0.08	82.874	13.464	34.705	2.452
0.1	77.564	12.764	32.4	2.399

Velocity behavior for isotropic medium with inclusions of high and low aspect ratios are shown on figures (2.11) and (2.12) respectively. The decrease of velocity with gas content is non-linear and reaches about seven percent at high aspect ratios and around 15 percent at lower aspect ratios.

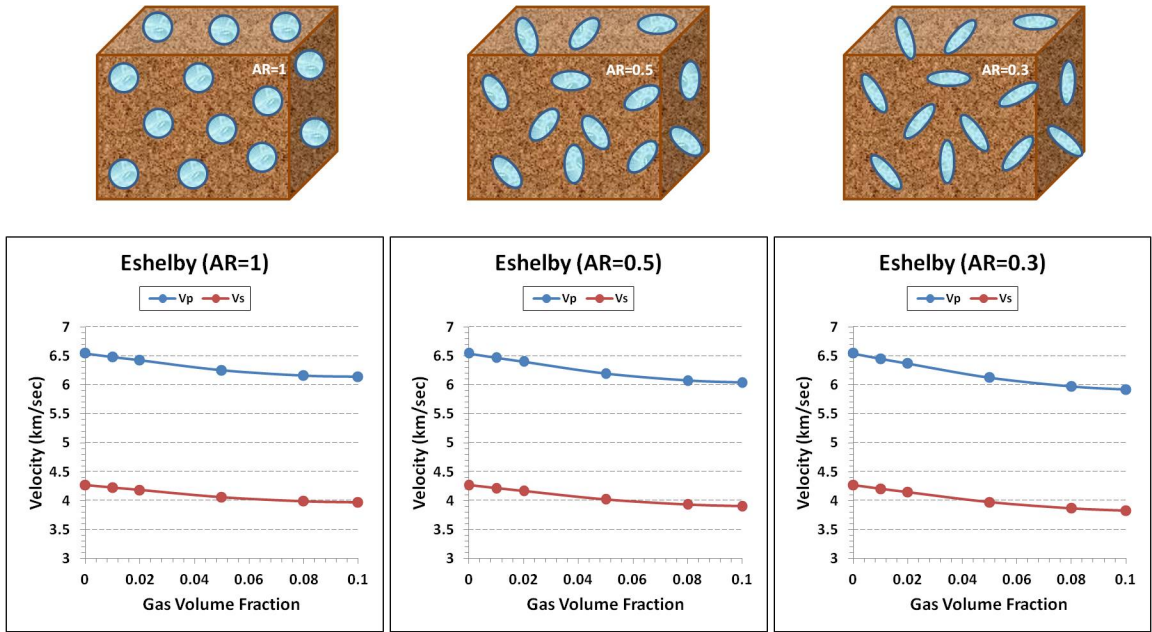


Figure 2.11: Variation of velocity with gas content for high AR (Eshelby Isotropic)

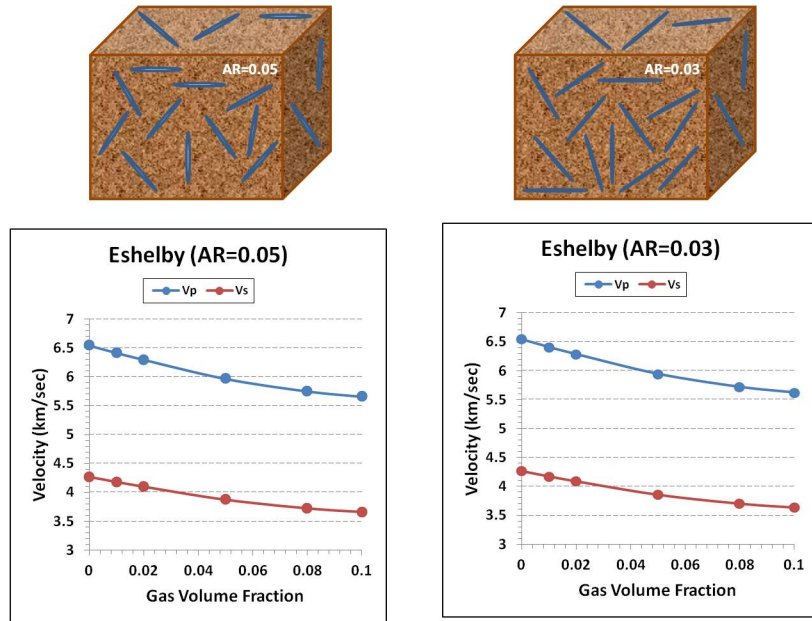


Figure 2.12: Variation of velocity with gas content for low AR (Eshelby Isotropic)

In the case of anisotropy we have preferred orientation of minerals in the media;

however inclusions remain randomly oriented. Figure (2.13) describes the model and the results of calculations of elastic stiffness tensor as a function of both gas volume concentration and higher aspect ratios ($AR = 1$, $AR = 0.5$ and $AR = 0.3$). Tables (2.13), (2.14), and (2.15) contain numerical results of figure (2.13).

Table 2.13: Stiffness tensor vs. gas content. Aspect ratio is 1 (Eshelby Anisotropic)

Gas Fraction	C_{11}	C_{12}	C_{13}	C_{33}	C_{44}	C_{66}	ρ
0	114.17	17.15	12.687	90.525	44.25	48.51	2.665
0.01	111.399	16.79	12.475	88.46	43.168	47.304	2.638
0.02	108.759	16.445	12.27	86.487	42.138	46.157	2.612
0.05	101.543	15.49	11.686	81.065	39.323	43.027	2.532
0.08	95.225	14.638	11.15	76.284	36.86	40.294	2.452
0.1	91.434	14.12	10.816	73.398	35.383	38.657	2.399

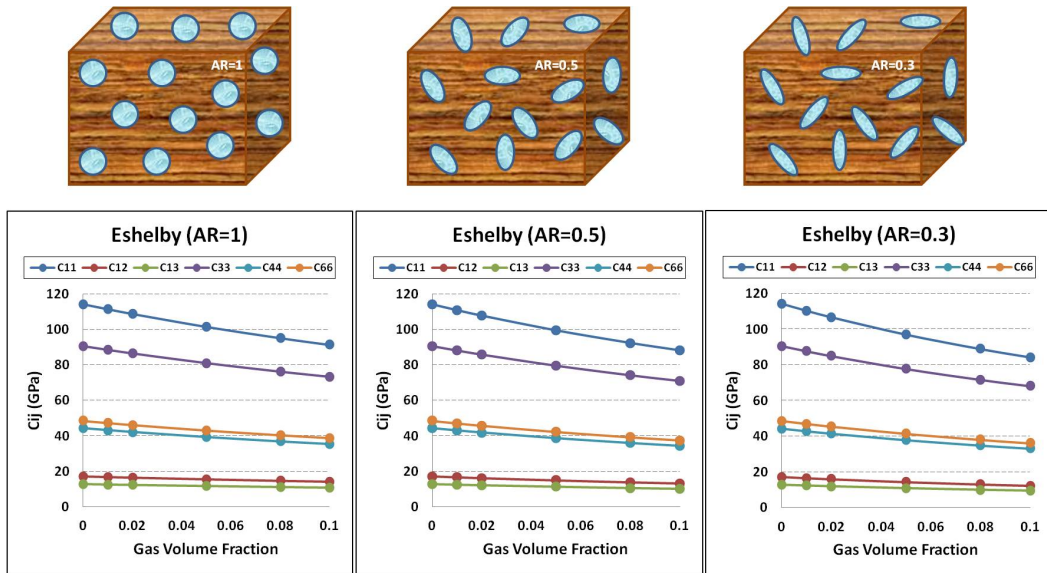


Figure 2.13: Variation of stiffness with gas content for high AR (Eshelby Anisotropic)

Table 2.14: Variation of stiffness with gas content. AR is 0.5 (Eshelby Anisotropic)

Gas Fraction	C_{11}	C_{12}	C_{13}	C_{33}	C_{44}	C_{66}	ρ
0	114.17	17.15	12.687	90.525	44.25	48.51	2.665
0.01	110.895	16.655	12.38	88.1	43.004	47.12	2.638
0.02	107.803	16.187	12.087	85.801	41.827	45.808	2.612
0.05	99.482	14.93	11.284	79.573	38.653	42.276	2.532
0.08	92.354	13.855	10.58	74.188	35.926	39.25	2.452
0.1	88.144	13.22	10.157	70.986	34.312	37.462	2.399

Table 2.15: Variation of stiffness with gas content. AR is 0.3 (Eshelby Anisotropic)

Gas Fraction	C_{11}	C_{12}	C_{13}	C_{33}	C_{44}	C_{66}	ρ
0	114.17	17.15	12.687	90.525	44.25	48.51	2.665
0.01	110.254	16.478	12.254	87.641	42.798	46.888	2.638
0.02	106.598	15.857	11.85	84.935	41.438	45.371	2.612
0.05	96.954	14.241	10.784	77.735	37.831	41.357	2.532
0.08	88.911	12.921	9.894	71.66	34.802	37.955	2.452
0.1	84.251	12.168	9.378	68.111	33.038	36.042	2.399

The behavior of stiffness tensor in a medium with inclusions of low aspect ratios are shown in the figure (2.14) and data are recorded in tables (2.16) and (2.17).

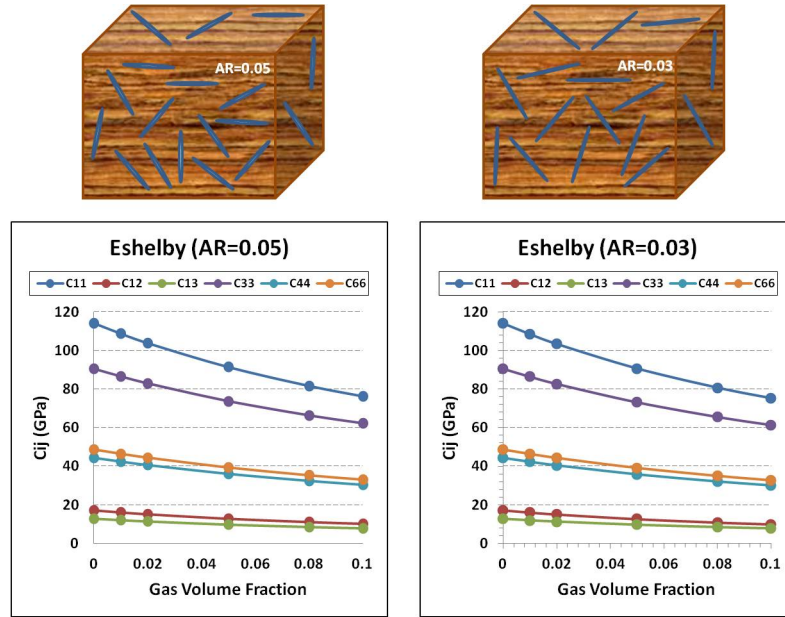


Figure 2.14: Variation of stiffness with gas content for low AR (Eshelby Anisotropic)

Table 2.16: Variation of stiffness with gas content. AR is 0.05 (Eshelby Anisotropic)

Gas Fraction	C_{11}	C_{12}	C_{13}	C_{33}	C_{44}	C_{66}	ρ
0	114.17	17.15	12.687	90.525	44.25	48.51	2.665
0.01	108.756	16.073	11.967	86.566	42.311	46.342	2.638
0.02	103.834	15.116	11.321	82.94	40.536	44.359	2.612
0.05	91.426	12.799	9.737	73.683	36.002	39.314	2.532
0.08	81.671	11.075	8.534	66.288	32.381	35.299	2.452
0.1	76.249	10.153	7.882	62.132	30.346	33.049	2.399

Table 2.17: Variation of stiffness with gas content. AR is 0.03 (Eshelby Anisotropic)

Gas Fraction	C_{11}	C_{12}	C_{13}	C_{33}	C_{44}	C_{66}	ρ
0	114.17	17.15	12.687	90.525	44.25	48.51	2.665
0.01	108.546	16.017	11.927	86.415	42.242	46.264	2.638
0.02	103.451	15.017	11.251	82.663	40.409	44.217	2.612
0.05	90.687	12.616	9.604	73.139	35.754	39.036	2.532
0.08	80.732	10.851	8.369	65.586	32.06	34.942	2.452
0.1	75.229	9.915	7.705	61.231	29.995	32.658	2.399

Based on the elastic stiffness tensor data and density values, we have calculated velocities as a function of gas content and aspect ratios. The variation of V_P , V_{SV} , and V_{SH} velocities with the increase of gas content is dramatic compared to the velocity values calculated using VRH averaging technique. Figure (2.15), along with the tables (2.18), (2.19), and (2.20), describe the data for higher (1, 0.5, and 0.3) aspect ratios.

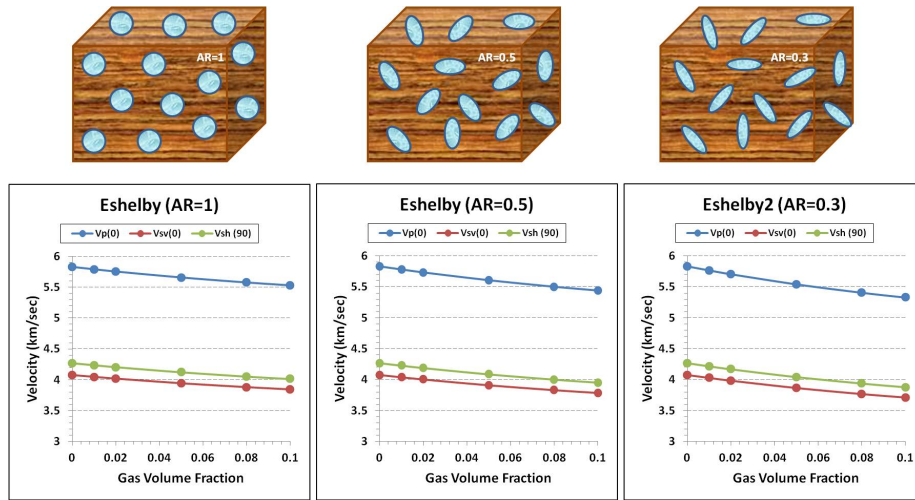


Figure 2.15: Variation of velocity with gas content for high AR (Eshelby Anisotropic)

Table 2.18: Velocity vs. gas content. Aspect ratio is 1 (Eshelby Anisotropic)

Gas Fraction	V_P (km/sec)	V_{SV} (km/sec)	V_{SH} (km/sec)
0	5.828	4.075	4.266
0.01	5.791	4.045	4.235
0.02	5.754	4.017	4.204
0.05	5.658	3.941	4.122
0.08	5.578	3.877	4.054
0.1	5.531	3.840	4.014

Table 2.19: Velocity vs. gas content. Aspect ratio is 0.5 (Eshelby Anisotropic)

Gas Fraction	V_P (km/sec)	V_{SV} (km/sec)	V_{SH} (km/sec)
0	5.828	4.075	4.266
0.01	5.779	4.038	4.226
0.02	5.731	4.002	4.188
0.05	5.606	3.907	4.086
0.08	5.501	3.828	4.000
0.1	5.439	3.782	3.952

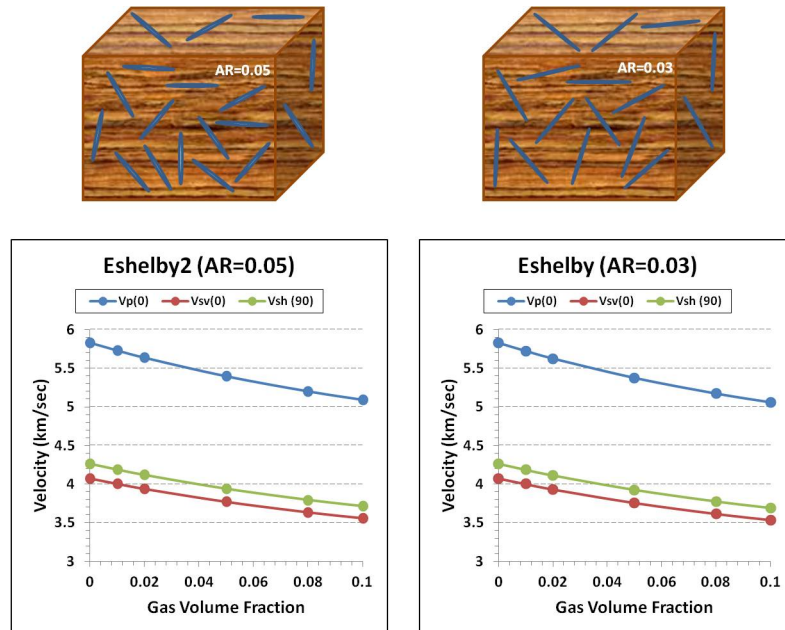


Figure 2.16: Variation of velocity with gas content for low AR (Eshelby Anisotropic)

Table 2.20: Velocity vs. gas content. Aspect ratio is 0.3 (Eshelby Anisotropic)

Gas Fraction	V_p (km/sec)	V_{SV} (km/sec)	V_{SH} (km/sec)
0	5.828	4.075	4.266
0.01	5.764	4.028	4.216
0.02	5.702	3.983	4.168
0.05	5.541	3.865	4.042
0.08	5.406	3.767	3.936
0.1	5.328	3.711	3.876

Figure (2.16) shows the models and results for media with inclusion of low aspect ratios. It is observed that as aspect ratios decrease, velocity values tend to decrease as well, however very slightly. Data are represented in tables (2.21) and (2.22).

Table 2.21: Velocity vs. gas content. Aspect ratio is 0.05 (Eshelby Anisotropic)

Gas Fraction	V_p (km/sec)	V_{SV} (km/sec)	V_{SH} (km/sec)
0	5.828	4.075	4.266
0.01	5.728	4.005	4.191
0.02	5.635	3.939	4.121
0.05	5.395	3.771	3.940
0.08	5.199	3.634	3.794
0.1	5.089	3.557	3.712

Table 2.22: Velocities vs. gas content. Aspect ratio is 0.03 (Eshelby Anisotropic)

Gas Fraction	V_p (km/sec)	V_{SV} (km/sec)	V_{SH} (km/sec)
0	5.828	4.075	4.266
0.01	5.723	4.002	4.188
0.02	5.626	3.933	4.114
0.05	5.375	3.758	3.926
0.08	5.172	3.616	3.775
0.1	5.057	3.536	3.689

2.3.4 Discussion and Comparison of VRH with Eshelby

In this subsection we present the differences between elastic properties calculated using VRH and Eshelby methods for both isotropic and anisotropic media. Figure (2.17) shows the percentage difference between elastic stiffness tensor values calculated by VRH and Eshelby techniques for the isotropic media.

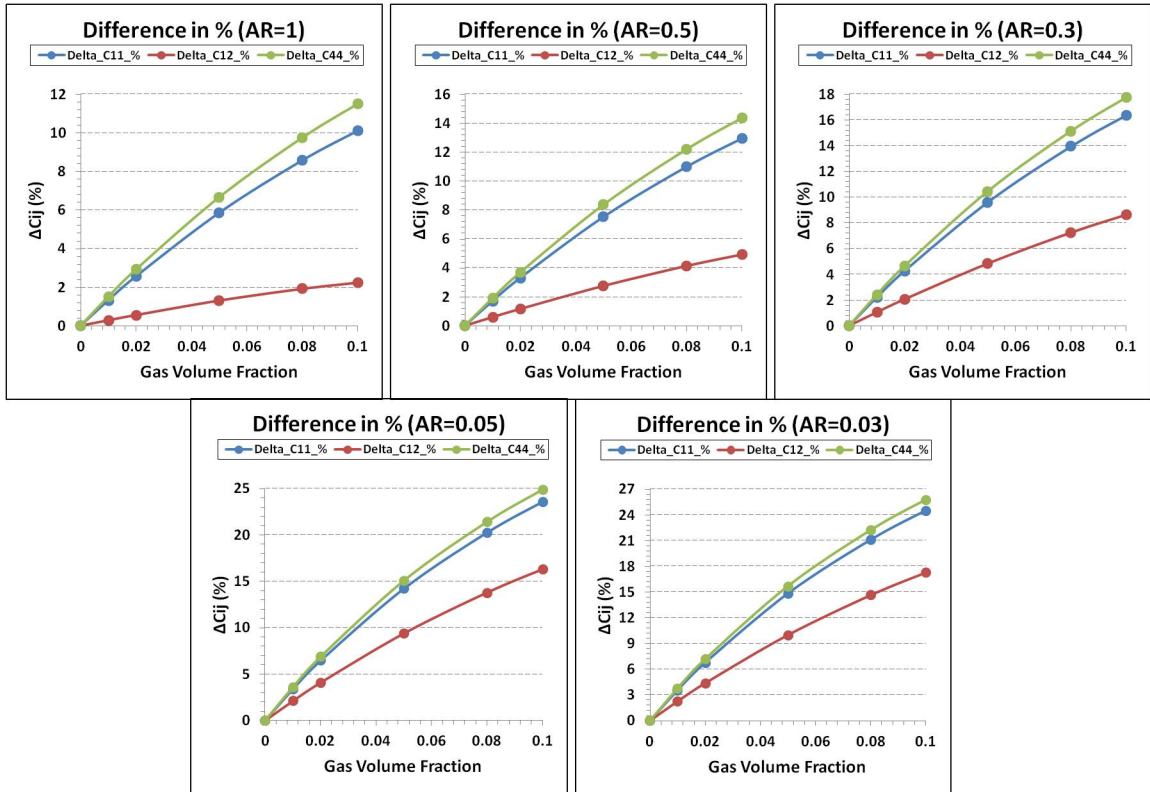


Figure 2.17: Difference between VRH and Eshelby stiffness tensor value. Isotropic

The difference between elastic stiffness tensor values calculated by VRH technique and those calculated by Eshelby technique tends to increase as the gas content increases. As aspect ratio decreases the ΔC_{ij} increases even faster with gas content. This might be explained by the observation that elastic stiffness tensor values ob-

tained by Eshelby method decrease as aspect ratio of inclusions decreases and VRH method is independent of inclusions geometrical arrangement, figure (2.18).

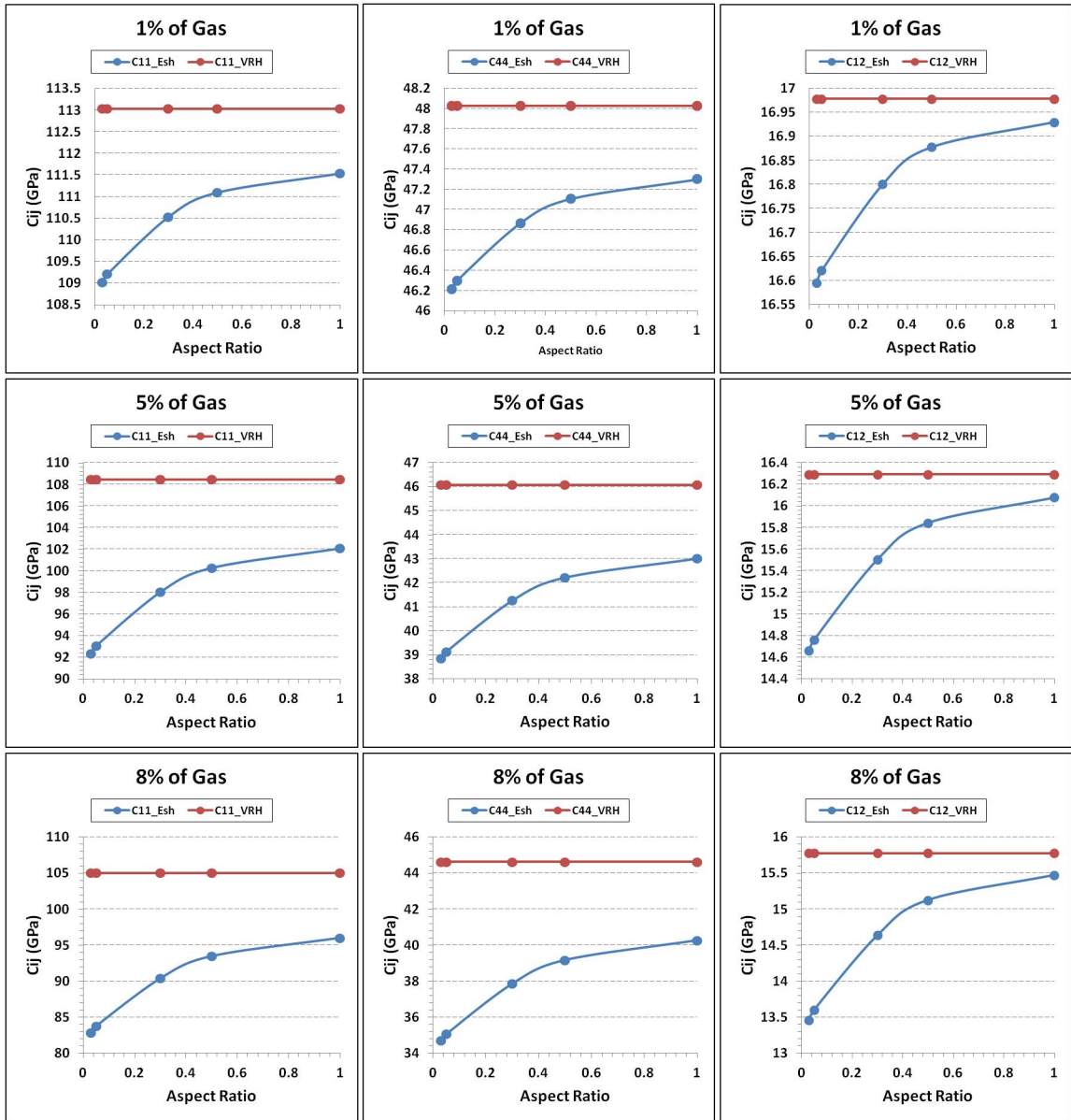


Figure 2.18: Variations of stiffness tensor with aspect ratio. Isotropic

Another way to show the dependence of ΔC_{ij} on aspect ratio is by keeping gas content constant. Figure (2.19) shows an example for the gas content of one percent.

Tables (2.23) and (2.24) show the data of the figure (2.19) in GPa and percentage.

Table 2.23: Variations of ΔC_{ij} with aspect ratio at one percent of gas. Isotropic

Gas Fraction	ΔC_{11} (GPa)	ΔC_{12} (GPa)	ΔC_{44} (GPa)
1	1.496	0.049	0.724
0.5	1.935	0.101	0.918
0.3	2.499	0.178	0.161
0.05	3.821	0.358	1.732
0.03	4.008	0.384	1.813

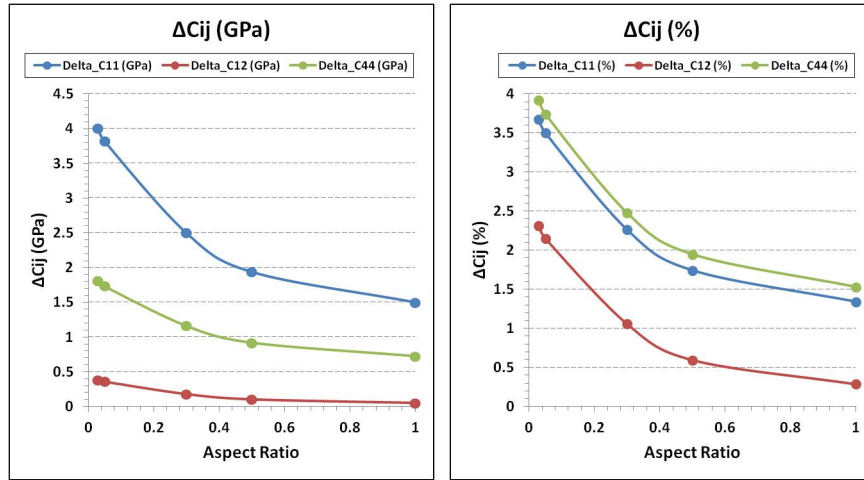


Figure 2.19: Variations of ΔC_{ij} with aspect ratio at one percent of gas. Isotropic

Similar behavior is observed when we plot calculated velocities as a function of gas content and aspect ratios of inclusions. We subtract velocity values calculated by Eshelby's method from velocity values calculated by VRH method and plot the differences versus gas content and aspect ratios, figure (2.20).

Table 2.24: Variations of ΔC_{ij} (%) with aspect ratio at one percent of gas. Isotropic

Gas Fraction	ΔC_{11} (%)	ΔC_{12} (%)	ΔC_{44} (%)
1	1.342	0.286	1.530
0.5	1.742	0.595	1.949
0.3	2.261	1.056	2.477
0.05	3.499	2.151	3.741
0.03	3.677	2.311	3.923

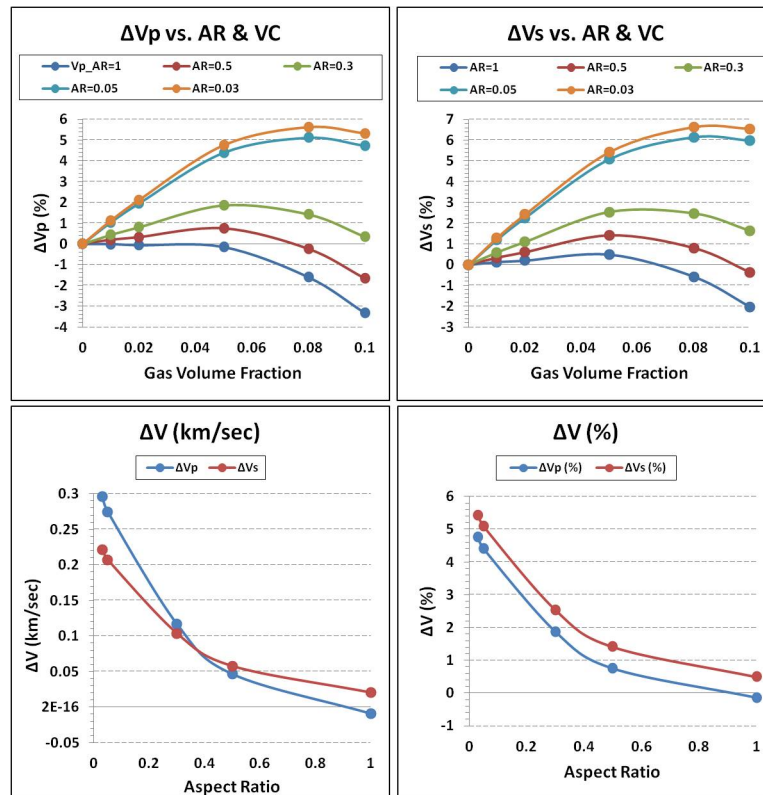


Figure 2.20: Velocity differences as a function of gas content and aspect ratio. Isotropic

Similar conclusions were derived observing the results of calculations for anisotropic media. Anisotropic media is characterized by hexagonal type of symmetry of the solid matrix; however inclusions of varying aspect ratios oriented randomly. The differ-

ence between VRH and Eshelby in terms of elastic stiffness tensor is much higher than that for isotropic media, and it tends to increase as gas concentration increases and/or aspect ratio decreases, figure (2.21). This can be explained by figure (2.22), where we observed independence of stiffness tensor calculated by the VRH method on aspect ratio and big dependence of stiffness tensor calculated by the Eshelby's method.

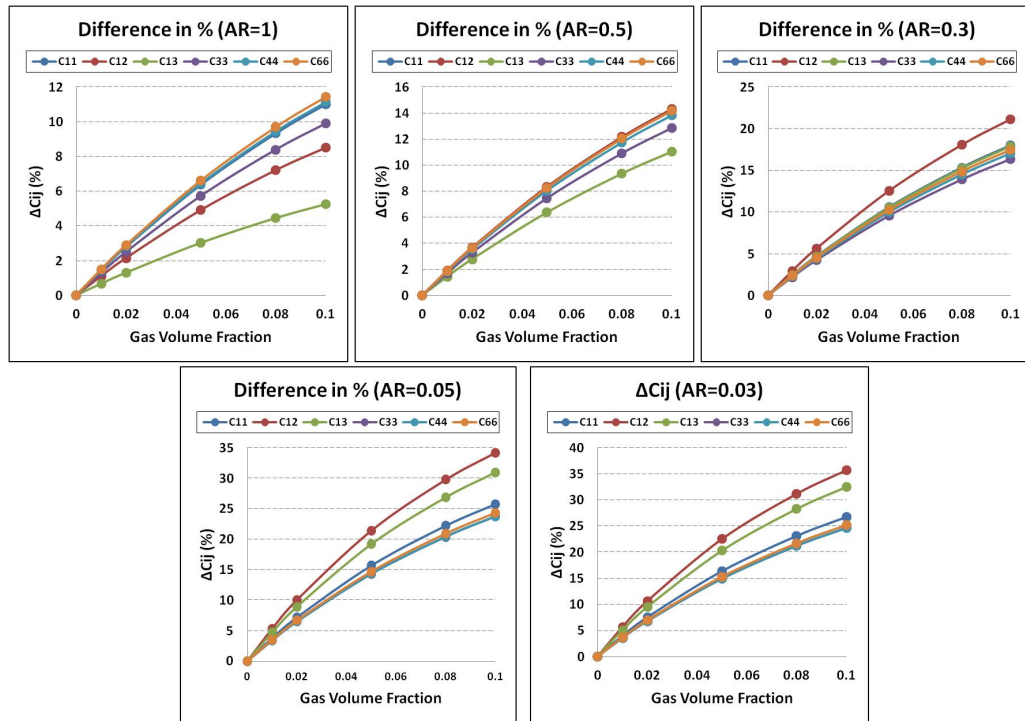


Figure 2.21: Difference between VRH and Eshelby stiffness tensor. Anisotropic

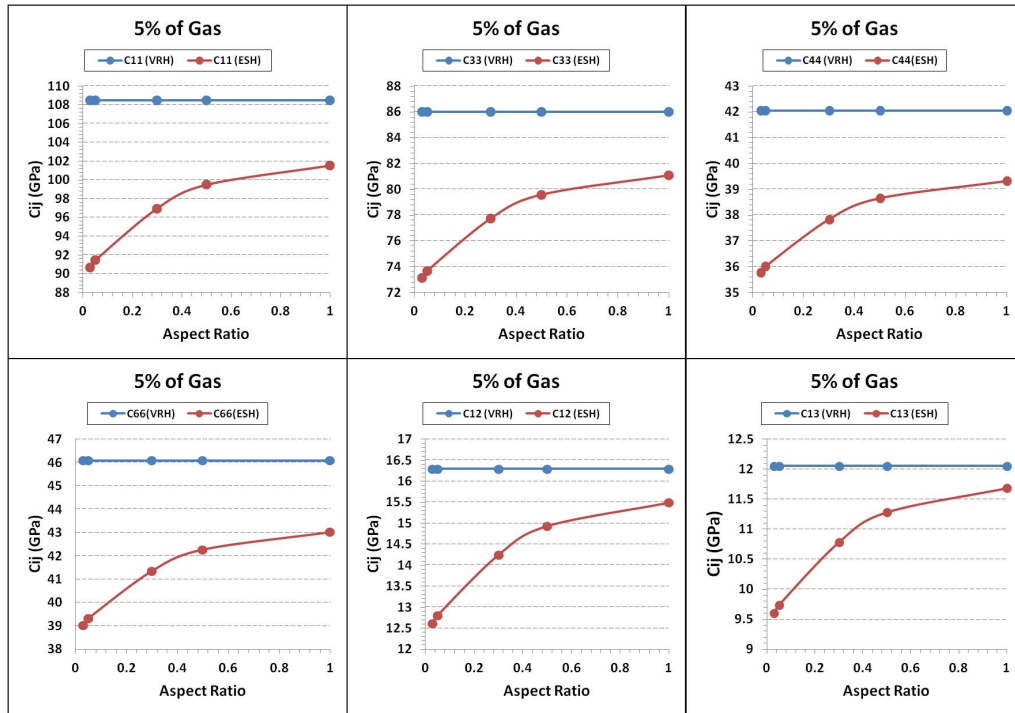


Figure 2.22: Variations of stiffness tensor with aspect ratio. Anisotropic

Figure (2.23) is another way to represent the data in figure (2.21) in order to directly observe the variation of elastic stiffness tensor differences as a function of aspect ratio. The gas content is one percent. As aspect ratio increases these differences decrease.

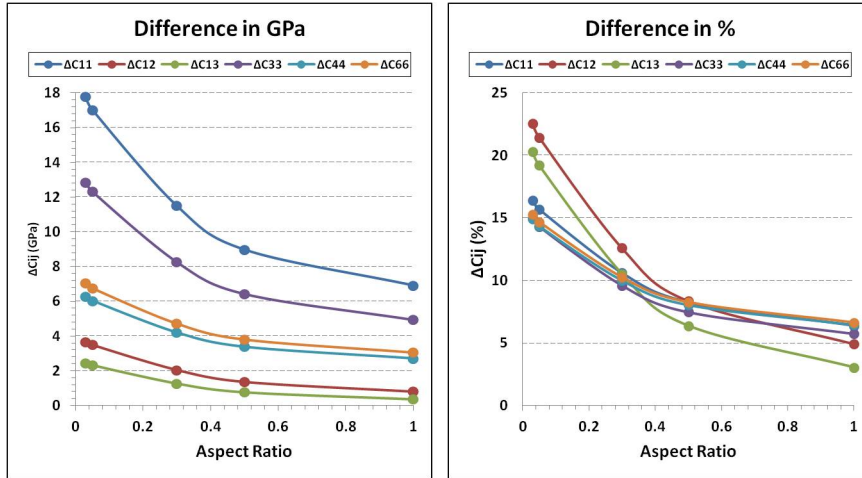


Figure 2.23: Variations of ΔC_{ij} with aspect ratio at one percent of gas. Anisotropic

In the case of velocity differences between VRH and Eshelby, we also observe an increase in values as gas content increased, figure (2.24), and an abrupt decrease in values as aspect ratio increased, figure(2.25). This observation can be explained by the physical characteristic behind the VRH and Eshelby averaging techniques. The VRH method is invariant with any geometrical changes of inclusions but size, while the Eshelby methods shows huge dependence on the geometry of inclusion. Therefore, the differences between two methods are dependent of geometrical arrangement of inclusions as well. As gas content increases, the dependence on aspect ratio also increases. Figure(2.25) shows examples for the medium with one and five percent of gas content respectively.

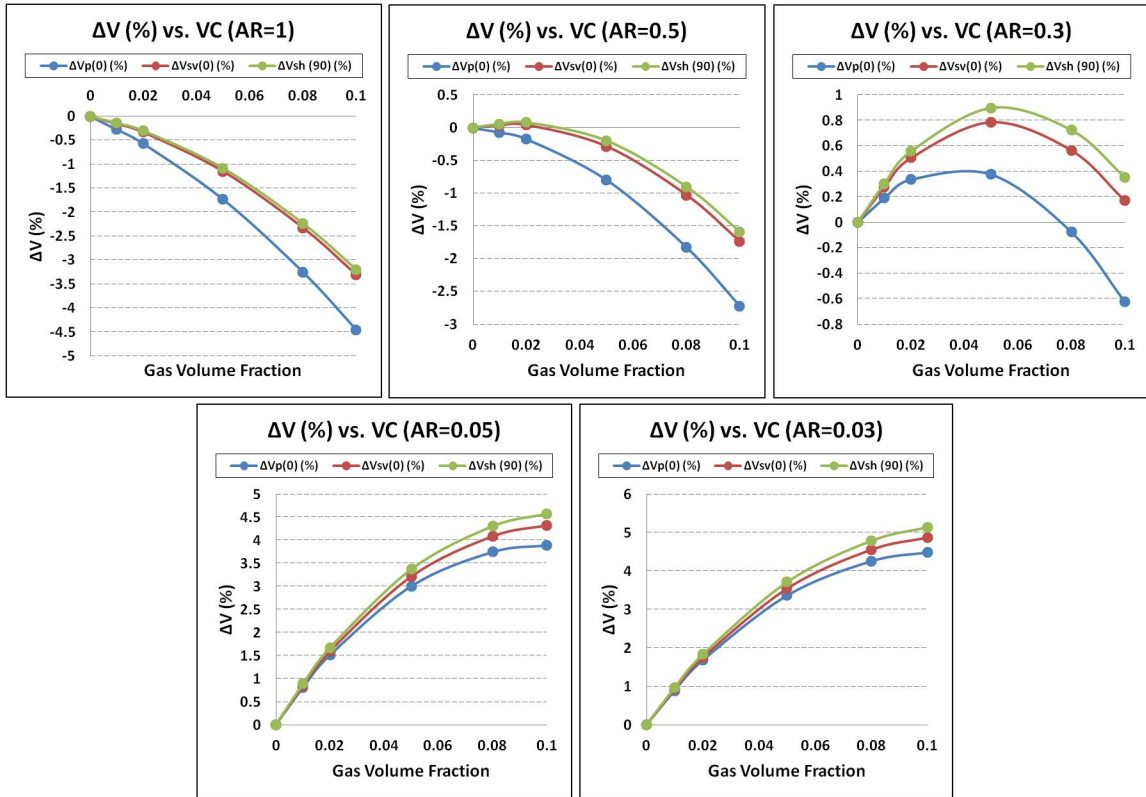


Figure 2.24: Velocity differences versus gas content. Anisotropic

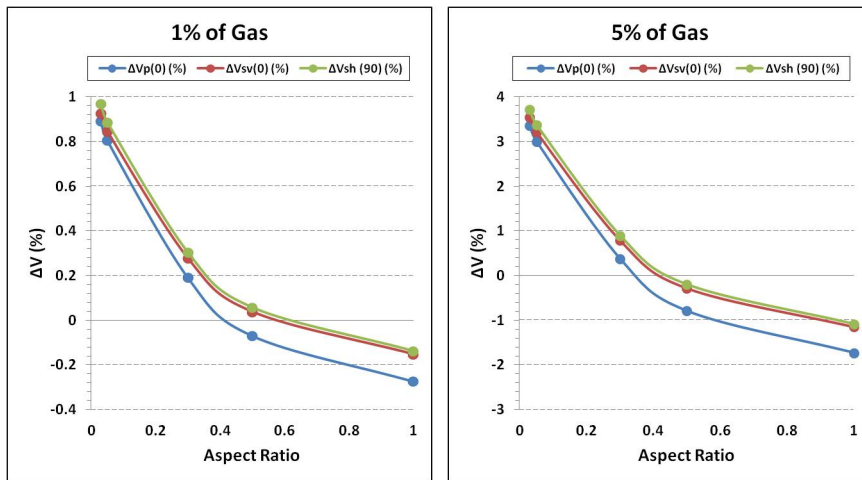


Figure 2.25: Velocity differences versus aspect ratio. Anisotropic

For the anisotropic case it is also useful to analyze the behavior of anisotropy co-

efficient. Figure (2.26) shows the variation of the anisotropy coefficient as a function of gas volume concentration at aspect ratio of 0.03. As gas content decreases, the significant increase in anisotropy coefficient in both P-wave and S-wave is observed due to the matrix having hexagonal symmetry.

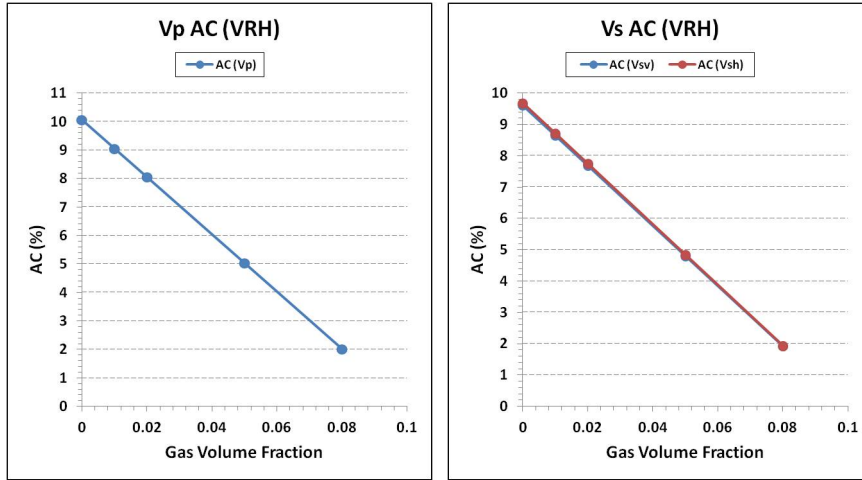


Figure 2.26: Anisotropy coefficient as a function of aspect ratio

Table 2.25: Anisotropy coefficients data

Aspect Ratio	$AC_{VRH}(Vp)$	$AC_{VRH}(Vs)$	$AC_{Eshelby}(Vp)$	$AC_{Eshelby}(Vs)$
1	10.062	9.617	5.368	6.103
0.5	10.062	9.617	7.143	7.746
0.3	10.062	9.617	9.381	9.804
0.05	10.062	9.617	14.523	14.570
0.03	10.062	9.617	15.238	15.239

Thomsen's parameters to characterise anisotropy have also been computed and presented in figure (2.27). The anisotropy parameters that were computed based on the VRH method are invariant to the change in gas content, while parameters that were computed based on Eshelby's method decrease as gas content increases.

This might be explained by the same rate of stiffness variation in the case of VRH averaging and different rates of variation in the case of Eshelby's averaging that is controlled by geometry of inclusions.

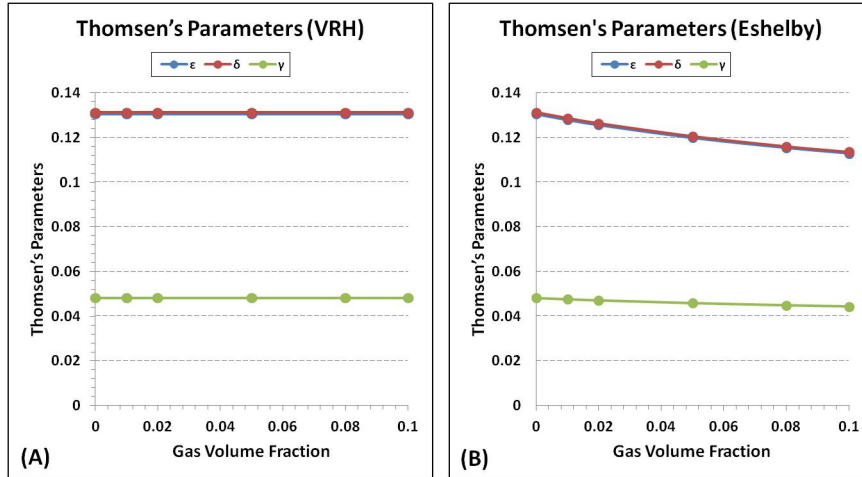


Figure 2.27: Thomsen's parameters vs. gas content. (A) VRH method (B) Eshelby's method at AR=0.03

In conclusion, we suggest to use VRH technique in the case when the properties of inclusions are very similar in values to the properties of the matrix. In this case VRH results are very close to Eshelby's results, and the VRH method is simpler and faster. However, in the case of big variations in properties between inclusions and matrix, it is recommended to apply Eshelby's method as an averaging technique.

2.4 Applications of Spatial Correlation Function

This section describes the application of spatial correlation approximation technique in both isotropic and anisotropic cases.

2.4.1 Application of PCA in an Isotropic Media

The general expression of elastic stiffness tensor in crystallographic system of coordinates for the medium of orthorhombic type of symmetry is shown in the following form:

$$C_{ijkl} = \sum_{n=1}^3 [\lambda_n \delta_{in} \delta_{jn} \delta_{kn} \delta_{ln} + \mu_n (\delta_{in} \delta_{jn} \delta_{kl} + \delta_{ij} \delta_{kn} \delta_{ln}) + \nu_n (\delta_{in} \delta_{jk} \delta_{ln} + \delta_{jn} \delta_{ik} \delta_{ln} + \delta_{in} \delta_{jl} \delta_{kn} + \delta_{jn} \delta_{il} \delta_{kn})] \quad (2.30)$$

To represent equation (2.30) in laboratory system of coordinates, we have to involve direction-cosines that we receive through the rotation using Euler angles. Therefore, equation (2.30) becomes:

$$C_{ijkl} = \sum_{n=1}^3 [\lambda_n l_{in} l_{jn} l_{kn} l_{ln} + \mu_n (l_{in} l_{jn} \delta_{kl} + \delta_{ij} l_{kn} l_{ln}) + \nu_n (l_{in} \delta_{jk} l_{ln} + l_{jn} \delta_{ik} l_{ln} + l_{in} \delta_{jl} l_{kn} + l_{jn} \delta_{il} l_{kn})] \quad (2.31)$$

The direction-cosines (l_{ij}) are characterized by matrix equation (2.16). In order to obtain an equation of elastic stiffness tensor for the isotropic medium, the required parameters (λ_n , μ_n and ν_n) should take form:

$$\begin{aligned}
\lambda_1 &= 0; \lambda_2 = 0; \lambda_3 = 0 \\
\mu_1 &= \frac{1}{2}C_{12}; \mu_2 = \frac{1}{2}C_{12}; \mu_3 = \frac{1}{2}C_{12} \\
\nu_1 &= \frac{1}{4}(C_{11} - C_{12}) \\
\nu_2 &= \frac{1}{4}(C_{11} - C_{12}) \\
\nu_3 &= \frac{1}{4}(C_{11} - C_{12})
\end{aligned} \tag{2.32}$$

In order to calculate effective elastic stiffness tensor of the medium, we need to obtain averaged stiffness tensor value and add to it the term responsible for fluctuation. Averaged stiffness tensor value is computed using the VRH or Eshelby's approximation technique. Equation (2.17) is VRH averaging for isotropic medium, and equation (2.21) is VRH averaging for anisotropic medium. Results of averaging are presented in section (2.2). The term responsible for fluctuation also consists of two parts. The first part, which is the second derivative of Green's function, is described in subsection (1.3.1) for isotropic medium and in subsection (1.4.1) for anisotropic medium. The second part, which is correlation tensor or covariant tensor (under certain assumptions), describes the amplitude of spatial correlation function. The solution for the effective stiffness tensor in isotropic case can be obtained analytically. The equation for effective stiffness tensor has been shown in chapter one in the following form:

$$C_{ijnp}^* = \langle C_{ijnp} \rangle + \frac{1}{8\pi^3} A_{mqnp}^{ijkl} \int G_{km,lq}(\mathbf{k}) d\mathbf{k} \tag{2.33}$$

Based on the equation (2.33) we need to have Fourier transformed second derivative of Green's function. Therefore, applying Fourier transformation to the equation (1.34) we receive:

$$\begin{aligned}\bar{G}_{mn,pq}(\mathbf{k}) &= -\frac{1}{\langle\mu\rangle} \frac{k_n k_q}{k k} \left(\delta_{mp} - \frac{\langle\lambda + \mu\rangle}{\langle\lambda + 2\mu\rangle} \frac{k_m k_p}{k k} \right) \\ \langle\mu\rangle &= \frac{1}{15} \sum_{n=1}^3 (\lambda_n + 10\mu_n)\end{aligned}\tag{2.34}$$

Substituting equation (2.34) into equation (2.33) and applying Kronecker's delta properties along with tensor convolution (Shermergor, 1977), we obtain analytical solution for effective elastic stiffness tensor in an isotropic medium. Therefore, solving this integral equation we obtain our final solution in the following form:

$$\begin{aligned}C_{ijnp}^* &= \langle C_{ijnp} \rangle - \frac{1}{225\langle\mu\rangle} \left\{ 5 \left[\alpha_2 \left(5 - 2 \frac{\langle\lambda + \mu\rangle}{\langle\lambda + 2\mu\rangle} \right) - \alpha_1 \frac{\langle\lambda + \mu\rangle}{\langle\lambda + 2\mu\rangle} \right] V_{ijnp} \right. \\ &\quad \left. + 3 \left[\alpha_3 \left(5 - 2 \frac{\langle\lambda + \mu\rangle}{\langle\lambda + 2\mu\rangle} \right) - \frac{1}{3} \alpha_2 \left(5 + \frac{\langle\lambda + \mu\rangle}{\langle\lambda + 2\mu\rangle} \right) + \alpha_1 \frac{\langle\lambda + \mu\rangle}{\langle\lambda + 2\mu\rangle} \right] D_{ijnp} \right\}\end{aligned}\tag{2.35}$$

The second part of the right-hand side in the equation (2.35) represents the term responsible for fluctuation in the isotropic medium with isotropic inclusions. Figure (2.28) shows the values of that term as a function of gas volume concentration that need to be added to the averaged stiffness tensor values to obtain effective C_{11}^* , C_{44}^* , and C_{12}^* values.

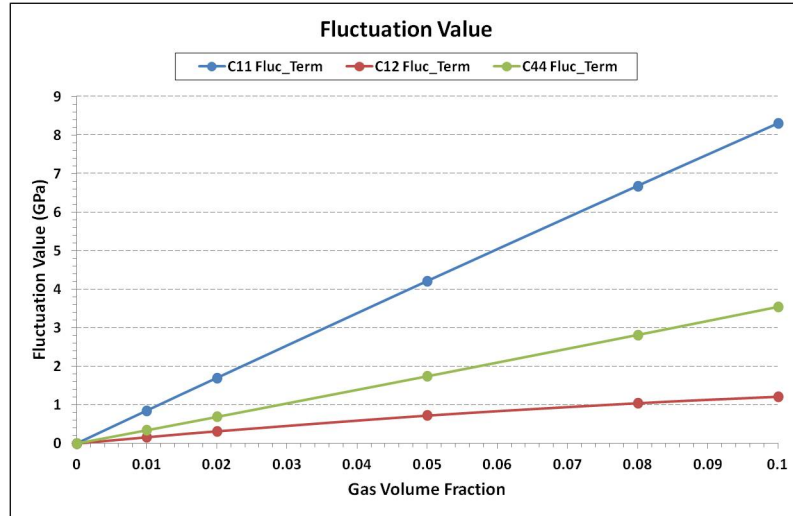


Figure 2.28: Terms responsible for fluctuation. Isotropic

Table (2.26) represents the fluctuation terms values plotted on figure (2.28). If the medium is pure isotropic solid matrix with very similar elastic properties between end-members, the term responsible for fluctuation will be equal to zero.

Table 2.26: Terms responsible for fluctuation. Isotropic

Gas content	$C_{11}(Fluc)$	$C_{12}(Fluc)$	$C_{44}(Fluc)$
0	0	0	0
0.01	0.853	0.164	0.344
0.02	1.701	0.319	0.691
0.05	4.214	0.727	1.744
0.08	6.682	1.05	2.816
0.1	8.303	1.218	3.542

However, if the medium contains fluid inclusions that are of significantly different elastic properties than the matrix, the fluctuation term will be introduced. The fluctuation term consists of correlation tensor that tends to increase in amplitude as the variation in the elastic properties between end-members increases. Analysis of

obtained results shows that fluctuation terms increase as the gas content increases.

Undefined terms in equation (2.35) can be expressed as:

$$\begin{aligned}
\alpha_1 &= \left[\sum_{n=1}^3 (\lambda_n + 3\mu_n^o + 4\nu_n^o) + 3(\mu_1^o + \mu_2^o + \mu_3^o) \right]^2 \\
\alpha_2 &= \sum_{n=1}^3 [\lambda_n + \mu_1^o + \mu_2^o + \mu_3^o + 3\mu_n^o + 4\nu_n^o]^2 \\
\alpha_3 &= \sum_{n=1}^3 [(\lambda_n + 2\mu_n^o + 4\nu_n^o)^2 + 4(\mu_n^{o2} + 2\nu_n^{o2})] + 4(\mu_1^o\mu_2^o + \mu_2^o\mu_3^o + \mu_3^o\mu_1^o) + 8(\nu_1^o\nu_2^o + \nu_2^o\nu_3^o + \nu_3^o\nu_1^o) \\
\mu_n^o &\equiv \mu_n - \frac{1}{2}\langle\lambda\rangle, \quad \nu_n^o \equiv \nu_n - \frac{1}{2}\langle\mu\rangle; \quad \langle\lambda\rangle = \frac{1}{15} \sum_{n=1}^3 (\lambda_n + 10\mu_n) \\
V_{ijnp} &= \frac{1}{3}\delta_{ij}\delta_{np}; \quad D_{ijnp} = \frac{1}{2}(\delta_{in}\delta_{jp} + \delta_{ip}\delta_{jn} - \frac{2}{3}\delta_{ij}\delta_{np})
\end{aligned} \tag{2.36}$$

Effective stiffness tensor values have been calculated using both VRH averaging plus fluctuation and Eshelby's averaging plus fluctuation. Results are presented on tables (2.27), (2.28), (2.29), (2.30), and figure (2.29) as a function of both gas content and aspect ratios of inclusions.

Table 2.27: PCA effective stiffness tensor values. VRH averaging. Isotropic

Gas content	$C_{11}^*(VRH)$	$C_{12}^*(VRH)$	$C_{44}^*(VRH)$
0	114.17	17.15	48.51
0.01	112.175	16.815	47.681
0.02	110.186	16.488	46.849
0.05	104.248	15.566	44.341
0.08	98.354	14.728	41.813
0.1	94.45	14.217	40.117

Effective elastic stiffness tensor values tend to decrease with an increase of gas content and decrease of aspect ratio.

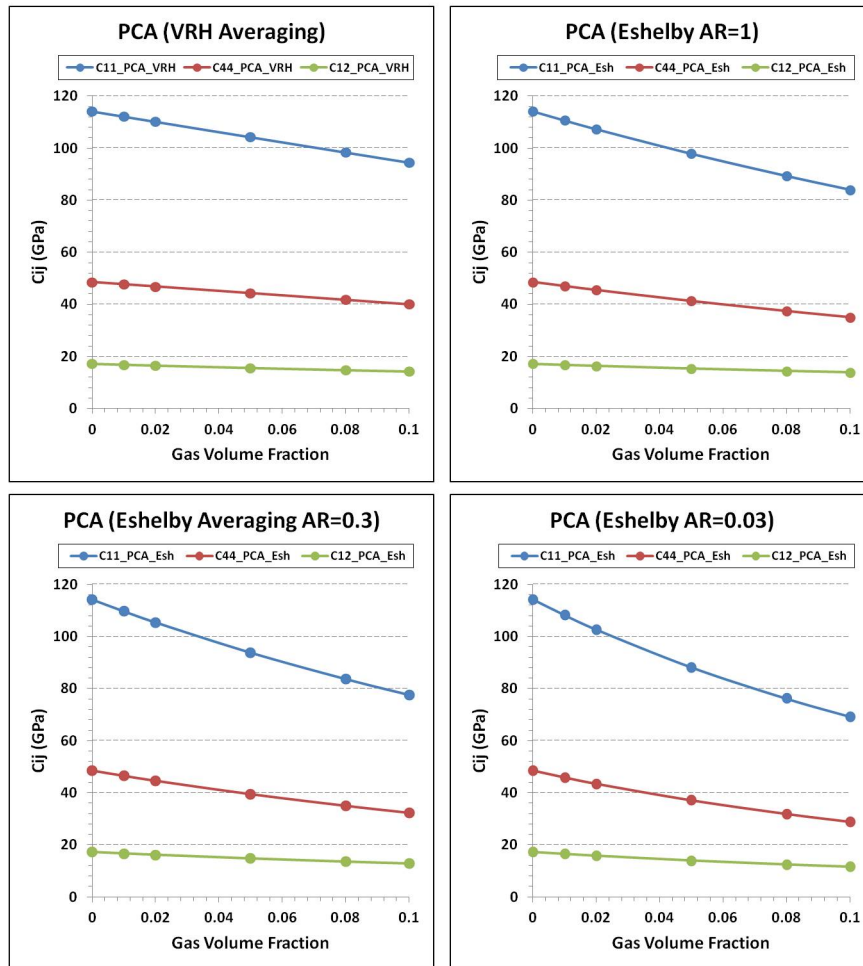
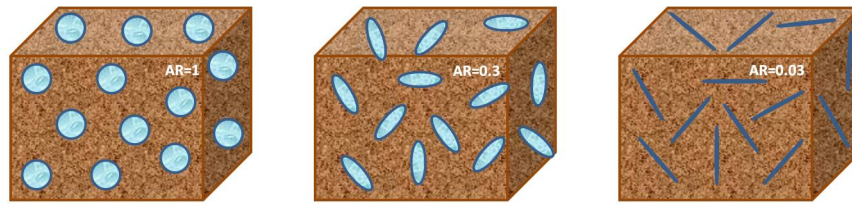


Figure 2.29: Effective stiffness tensor values. Isotropic

It is observed that when we apply the VRH averaging method in the PCA technique, the effective stiffness tensor values decrease linearly, while in the case of Eshelby's averaging, the effective stiffness tensor values decrease non-linearly as gas content increases. At small gas content (two to three percent), both averaging methods might

be applied in PCA technique, because their values are almost the same. However, as gas content increases, two averaging methods provide significantly different results.

Table 2.28: PCA effective stiffness tensor values. Eshelby AR=1. Isotropic

Gas content	$C_{11}^*(Esh)$	$C_{12}^*(Esh)$	$C_{44}^*(Esh)$
0	114.17	17.15	48.51
0.01	110.679	16.766	46.957
0.02	107.313	16.394	45.459
0.05	97.888	15.351	41.268
0.08	89.338	14.423	37.458
0.1	84.052	13.869	35.092

Table 2.29: PCA effective stiffness tensor values. Eshelby AR=0.3. Isotropic

Gas content	$C_{11}^*(Esh)$	$C_{12}^*(Esh)$	$C_{44}^*(Esh)$
0	114.17	17.15	48.51
0.01	109.676	16.637	46.52
0.02	105.413	16.142	44.635
0.05	93.819	14.778	39.52
0.08	83.694	13.586	35.054
0.1	77.603	12.885	32.359

Table 2.30: PCA effective stiffness tensor values. Eshelby AR=0.03. Isotropic

Gas content	$C_{11}^*(Esh)$	$C_{12}^*(Esh)$	$C_{44}^*(Esh)$
0	114.17	17.15	48.51
0.01	108.167	16.431	45.868
0.02	102.614	15.752	43.431
0.05	88.15	13.935	37.107
0.08	76.192	12.414	31.889
0.1	69.261	11.546	28.858

Figure (2.30) represents the variation of effective elastic stiffness tensor with

aspect ratio at gas content of one and 5 percent. It is observed that effective stiffness tensor values tend to increase as aspect ratio increases.

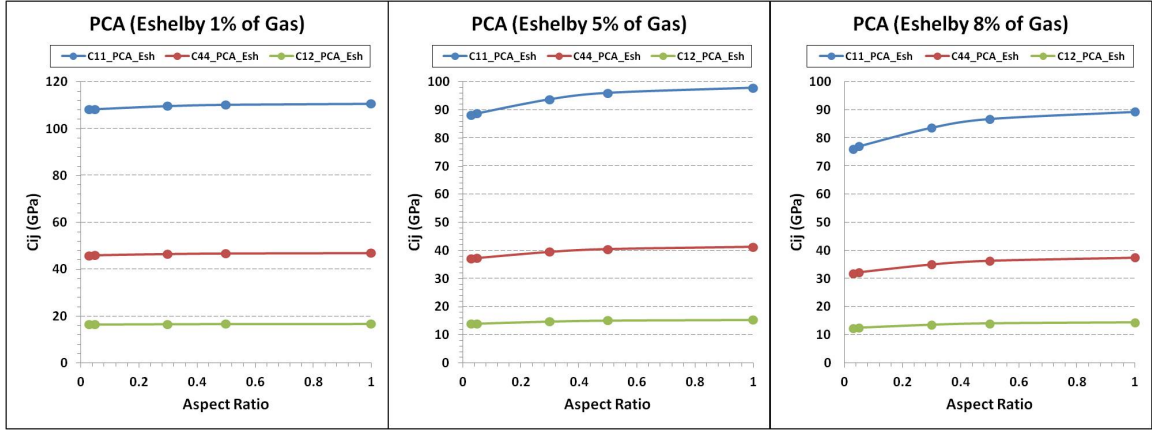


Figure 2.30: Effective stiffness tensor values vs. aspect ratio. Isotropic

P-wave and S-wave velocities can also be calculated from effective stiffness tensor and density values. Tables (2.31), (2.32), and figure (2.31) represent the calculated velocities. At low content (two to three percent) it does not matter what averaging method is applied since velocity values are very similar. However, as content increases variation of velocity is significant.

Table 2.31: PCA velocity values. VRH and Eshelby averaging, AR=1. Isotropic

Gas content	$V_P(VRH)$	$V_S(VRH)$	$V_P(Esh)$	$V_S(Esh)$
0	6.545	4.266	6.545	4.266
0.01	6.521	4.251	6.460	4.208
0.02	6.495	4.235	6.378	4.151
0.05	6.417	4.185	6.122	3.975
0.08	6.334	4.129	5.939	3.846
0.1	6.275	4.089	5.855	3.783

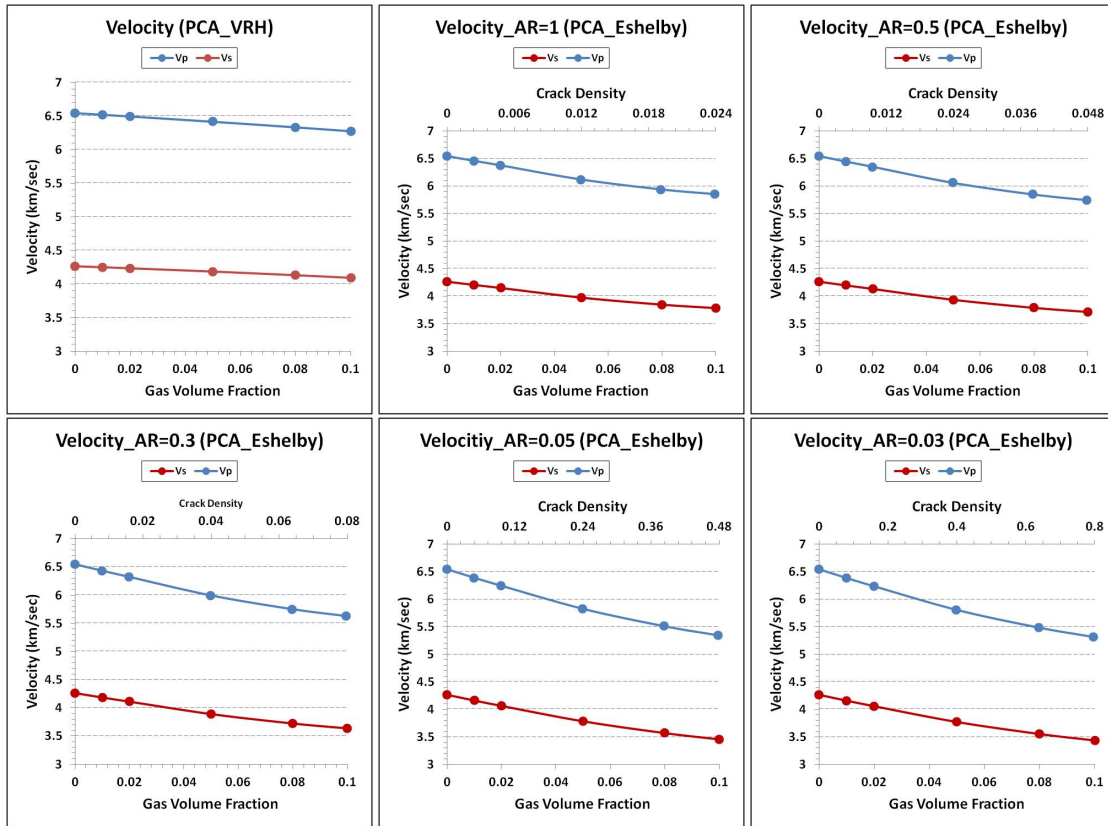


Figure 2.31: Velocities vs. gas content. Isotropic

Table 2.32: PCA velocity values. Eshelby, AR=0.3 and AR=0.03. Isotropic

Gas content	$V_P(Esh0.3)$	$V_S(Esh0.3)$	$V_P(Esh0.03)$	$V_S(Esh0.03)$
0	6.545	4.266	6.545	4.266
0.01	6.431	4.188	6.386	4.159
0.02	6.321	4.113	6.237	4.058
0.05	5.993	3.889	5.809	3.769
0.08	5.749	3.721	5.486	3.549
0.1	5.626	3.633	5.315	3.431

As a function of gas content both P-wave and S-wave velocities show inverse relationship. As aspect ratio increases velocity values tend to increase non-linearly.

In chapter one, the correlation tensor $B_{pqrs}^{ijkl}(\mathbf{r})$ has been expressed through covariant tensor (A_{pqrs}^{ijkl}) and a function ($\phi(\mathbf{r})$) that describes coordinate dependency (1.83). The covariant tensor is independent of coordinates, and therefore can be taken out of integration (1.85). Function $\phi(\mathbf{r})$ for isotropic medium is independent of rotation angles and becomes $\phi(r)$. Function $\phi(r)$ has been assigned a value of one to represent the situation when correlation radius or the distance between two point of correlation is zero. In this case we observed the highest correlation that represented the correlation right at the boundary of two end-members in the medium. In order to understand the behavior of correlation tensor as a function of correlation distance, it is required to introduce a distribution function. In our case, function $\phi(\mathbf{r})$ has been replaced by a Gaussian normal distribution:

$$\phi(r) = \frac{1}{\sqrt{2\pi}\sigma} \exp \left[-\frac{1}{2} \left(\frac{r - \mu}{\sigma} \right)^2 \right] \quad (2.37)$$

Equation 2.37 can be represented in wave-number domain by applying a Fourier transformation:

$$\phi(k) = \exp \left[i\mu k - \frac{1}{2} (\sigma k)^2 \right] \quad (2.38)$$

Here, i is an imaginary number, μ is a mean value and σ is standard deviation. Squared standard deviation σ^2 is called variance. Equation (1.85) then becomes:

$$C_{ijnp}^* = \langle C_{ijnp} \rangle + \frac{1}{8\pi^3} A_{mqnp}^{ijkl} \int \exp \left[i\mu k - \frac{1}{2} (\sigma k)^2 \right] G_{km,lq}(\mathbf{k}) d\mathbf{k} \quad (2.39)$$

Integration of the second derivative of Green's function is represented by equation (2.34). Integrating the Gaussian distribution function we obtain:

$$\phi(k) = \lim_{k \rightarrow \infty} \left[\frac{1}{2} \operatorname{erf} \left(\frac{1}{2} \frac{\sqrt{2}(k - \mu)}{\sigma} \right) + \frac{1}{2} \operatorname{erf} \left(\frac{1}{2} \frac{\mu\sqrt{2}}{\sigma} \right) \right] \quad (2.40)$$

Substituting equation (2.40) and equation (2.34) into equation (2.39), we obtain:

$$\begin{aligned} C_{ijnp}^* = & \langle C_{ijnp} \rangle - \frac{1}{8\pi^3} A_{mnp}^{ijkl} \lim_{k \rightarrow \infty} \left[\frac{1}{2} \operatorname{erf} \left(\frac{1}{2} \frac{\sqrt{2}(k - \mu)}{\sigma} \right) \right. \\ & \left. + \frac{1}{2} \operatorname{erf} \left(\frac{1}{2} \frac{\mu\sqrt{2}}{\sigma} \right) \right] \frac{1}{\langle \mu \rangle} \frac{k_n}{k} \frac{k_q}{k} \left(\delta_{mp} - \frac{\langle \lambda + \mu \rangle}{\langle \lambda + 2\mu \rangle} \frac{k_m}{k} \frac{k_p}{k} \right) \end{aligned} \quad (2.41)$$

Applying convolution and other simple mathematical operations, and setting $\mu = 0$ and $\sigma = 1$, we can rearrange equation (2.41) into simpler form:

$$\begin{aligned} C_{ijnp}^* = & \langle C_{ijnp} \rangle - \frac{\sqrt{2\pi}}{12\pi^2 \langle \mu \rangle} \frac{1}{5} \left[\left(5 - 2 \frac{\langle \lambda + \mu \rangle}{\langle \lambda + 2\mu \rangle} \right) \left(\frac{1}{3} \alpha_2 V_{ijnp} + \frac{1}{5} \left(\alpha_3 - \frac{1}{3} \alpha_2 \right) D_{ijnp} \right) \right. \\ & \left. - \frac{\langle \lambda + \mu \rangle}{\langle \lambda + 2\mu \rangle} \left(\frac{1}{3} \alpha_1 V_{ijnp} + \frac{1}{5} \left(\alpha_2 - \frac{1}{3} \alpha_1 \right) D_{ijnp} \right) \right] \end{aligned} \quad (2.42)$$

Expressions for α_1 , α_2 , α_3 , μ_n^o , $\langle \lambda \rangle$, V_{ijnp} , and D_{ijnp} are shown in equation (2.36). Figure (2.32) compares stiffness tensor (C_{11}) values computed using PCA, based on VRH averaging technique with pressure wave velocity as a function of gas content for different standard deviations (σ).

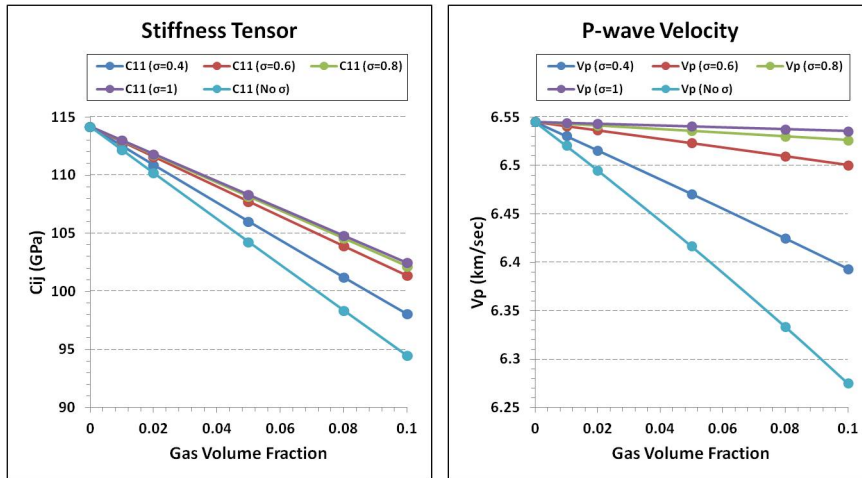


Figure 2.32: Stiffness and V_p vs. gas content for different sigma. VRH Isotropic

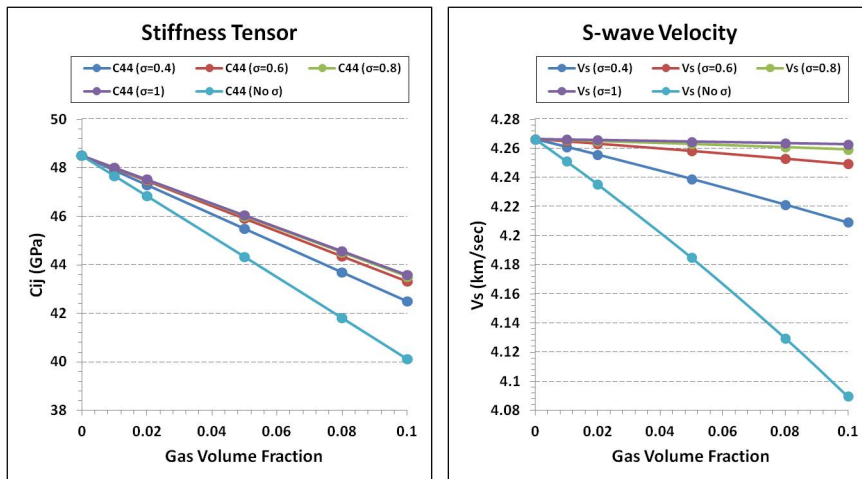


Figure 2.33: Stiffness and V_s vs. gas content for different sigma. VRH Isotropic

Figure (2.33) represents similar comparisons between stiffness tensor (C_{44}) and shear wave velocity as a function of gas content for different standard deviation values. In both cases, values decrease with gas content; the lower the standard deviation the higher the correlation. Results approach those values that were computed without distribution function, meaning at zero correlation radius. To highlight the

influence of correlation radius on velocities, we plotted velocities and their ratio versus standard deviation for five percent of gas, figure (2.34).

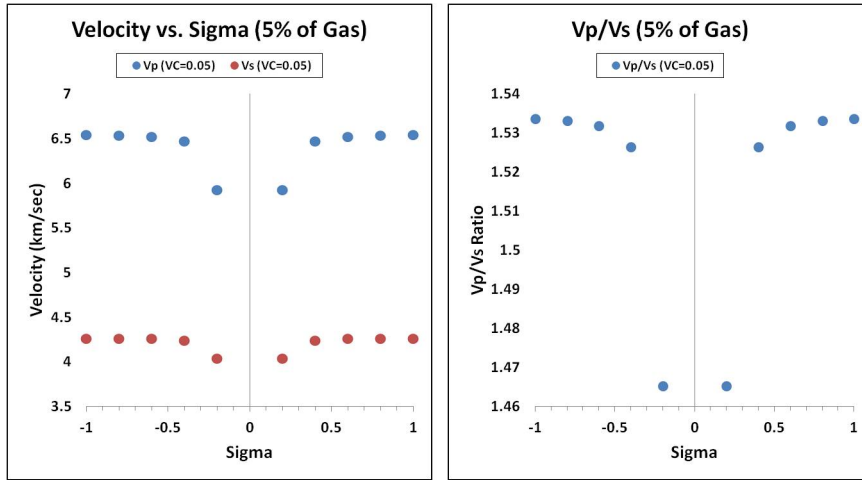


Figure 2.34: Velocities vs. sigma. Isotropic

Similar calculations were run for PCA based on Eshelby's averaging method. Results are plotted in figure (2.35) for stiffness tensor values (C_{11}) and pressure wave velocities (V_P) and in figure (2.36) for stiffness tensor (C_{44}) and shear wave velocities (V_S). Aspect ratio is kept constant at the value of 0.03 and gas content varies along with the crack density.

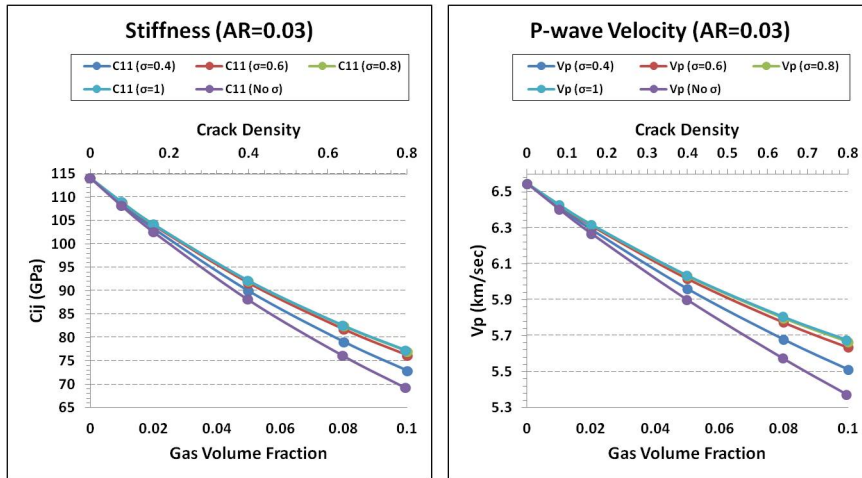


Figure 2.35: PCA (Eshelby's Averaging) stiffness tensor and V_p vs. gas content for different σ at $AR=0.03$. Isotropic

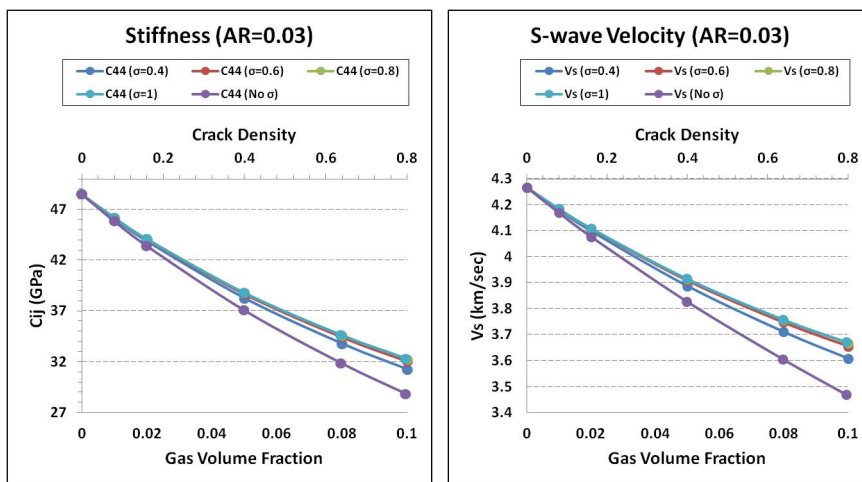


Figure 2.36: PCA (Eshelby's Averaging) stiffness tensor and V_s vs. gas content for different σ at $AR=0.03$. Isotropic

Poisson's ratio has also been computed and plotted on figure (2.37). This figure represents the comparison of Poisson's ratio computed using PCA based on VRH with PCA based on Eshelby's method. The behavior of both sets of curves is similar, however Poisson's ratio based on Eshelby's method shows slightly higher values.

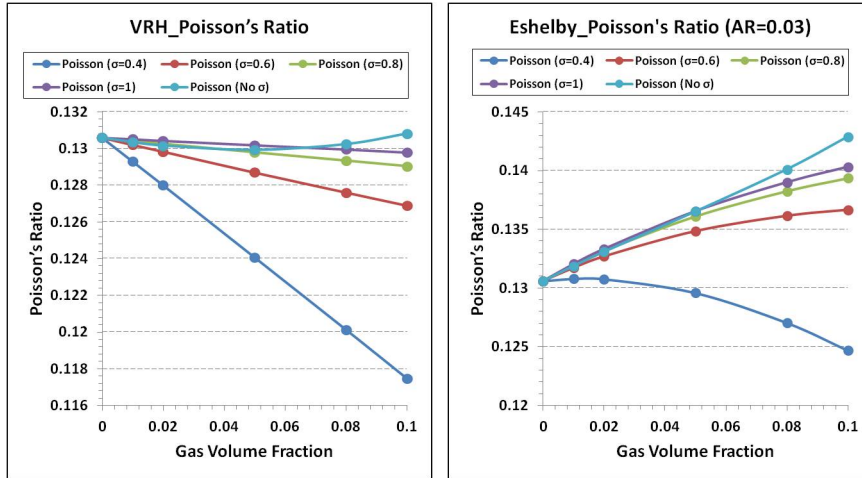


Figure 2.37: PCA Poisson's ratio vs.gas content for different sigma at AR=0.03

2.4.2 Application of PCA in an Anisotropic Media

Numerical solution for effective elastic stiffness tensor is primarily referred to the solution of Green's function, because the rest of the terms (averaged value and co-variant tensor) can be estimated analytically. To understand the behavior of the amplitude of spacial correlation approximation technique, we show the analysis of the covariant tensor separately. We know the covariant tensor operates with fluctuation terms only. Therefore, we need to introduce the fluctuation component of the elastic stiffness tensor. To do so, we need to find the averaged value of equation (2.30) and then subtract the result from the equation (2.30). The fluctuation

component for orthorhombic symmetry then takes the following form:

$$C'_{ijkl} = \sum_{n=1}^3 [\lambda_n \delta_{in} \delta_{jn} \delta_{kn} \delta_{ln} + \mu_n^o (\delta_{in} \delta_{jn} \delta_{kl} + \delta_{ij} \delta_{kn} \delta_{ln}) + \nu_n^o (\delta_{in} \delta_{jl} \delta_{kn} + \delta_{jn} \delta_{ik} \delta_{ln} + \delta_{in} \delta_{jk} \delta_{ln} + \delta_{jn} \delta_{il} \delta_{kn})] \quad (2.43)$$

Equation (2.43) represents the fluctuation component of stiffness tensor in the crystallographic system of coordinates. Therefore, by using the direction-cosines we transform equation (2.43) to the laboratory system of coordinates:

$$C'_{ijkl} = \sum_{n=1}^3 [\lambda_n l_{in} l_{jn} l_{kn} l_{ln} + \mu_n^o (l_{in} l_{jn} \delta_{kl} + \delta_{ij} l_{kn} l_{ln}) + \nu_n^o (l_{in} \delta_{jl} l_{kn} + l_{jn} \delta_{ik} l_{ln} + l_{in} \delta_{jk} l_{ln} + l_{jn} \delta_{il} l_{kn})] \quad (2.44)$$

Here, the direction-cosines (l_{ij}) are described by matrix equation (2.16). From equation (1.84) we know that covariant tensor has the form:

$$A_{pqrs}^{ijkl} = \langle C'_{ijkl}(\mathbf{r}) C'_{pqrs}(\mathbf{r}) \rangle \quad (2.45)$$

Angular brackets here represent averaging, and we have already introduced that averaging might be taken by integration over the volume. Here, we assumed that the correlation radius (\mathbf{r}) is zero, therefore, $\phi(\mathbf{r}) = \phi(0) = 1$. Similarly, without a distribution function we have an isotropic medium, and introducing the distribution function, we obtain covariant tensor values for an anisotropic medium of different kinds of symmetry. The distribution function is a Dirac's delta distribution. The

covariant tensor expression for an isotropic medium is:

$$A_{pqrs}^{ijkl} = \frac{\iiint C'_{ijkl}(\phi, \psi, \theta) C'_{pqrs}(\phi, \psi, \theta) \sin \phi d\phi d\psi d\theta}{\iiint \sin \phi d\phi d\psi d\theta} \quad (2.46)$$

Limits of integration for angle ϕ are from 0 to π , for angle ψ from 0 to 2π , and for angle θ from 0 to 2π as well. The covariant tensor for an anisotropic medium of orthorhombic symmetry can be calculated by introducing any distribution function $F(\phi, \psi, \theta)$:

$$A_{pqrs}^{ijkl} = \frac{\iiint C'_{ijkl}(\phi, \psi, \theta) C'_{pqrs}(\phi, \psi, \theta) F(\phi, \psi, \theta) \sin \phi d\phi d\psi d\theta}{\iiint F(\phi, \psi, \theta) \sin \phi d\phi d\psi d\theta} \quad (2.47)$$

In the simplest case we can use Dirac's delta function as a distribution that controls all three Euler angles. The expression takes form:

$$A_{pqrs}^{ijkl} = \frac{\iiint C'_{ijkl}(\phi, \psi, \theta) C'_{pqrs}(\phi, \psi, \theta) \delta(\phi - \phi_0) \delta(\psi - \psi_0) \delta(\theta - \theta_0) \sin \phi d\phi d\psi d\theta}{\iiint \delta(\phi - \phi_0) \delta(\psi - \psi_0) \delta(\theta - \theta_0) \sin \phi d\phi d\psi d\theta} \quad (2.48)$$

Here, ϕ_0 , ψ_0 , and θ_0 are known and take any value within the integration limits.

The covariant tensor for an anisotropic medium of hexagonal symmetry can be calculated by introducing Dirac's delta distribution functions that controls only one or two angles. The expression takes form:

$$A_{pqrs}^{ijkl} = \frac{\iiint C'_{ijkl}(\phi, \psi, \theta) C'_{pqrs}(\phi, \psi, \theta) \delta(\phi - \phi_0) \sin \phi d\phi d\psi d\theta}{\iiint \delta(\phi - \phi_0) \sin \phi d\phi d\psi d\theta} \quad (2.49)$$

In this case we control only one angle (ϕ), and the other two angles take completely random values. To obtain effective stiffness tensor values we need to take averaged stiffness tensor values and combine them with fluctuation terms. Averaging for anisotropic medium can be performed using the VRH or Eshelby's methods, equations (2.19) and (2.23), or (2.27), respectively. The fluctuation term consists of an anisotropic covariant tensor (A_{pqrs}^{ijkl}), that can be computed using equation (2.49), and an anisotropic Green's function, that can be calculated using equation (2.13). Calculated effective stiffness tensor values for both cases of averaging methods (VRH and Eshelby) are presented in figure (2.39). Anisotropic model in this case consists of anisotropic matrix of hexagonal type of symmetry and randomly oriented isotropic inclusions. Fluctuation values for anisotropic medium are shown in figure (2.38).

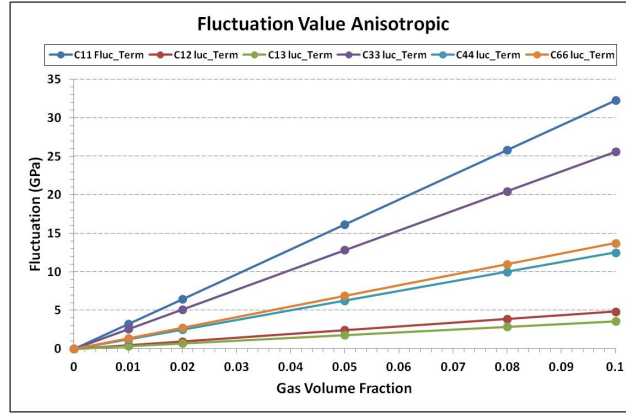


Figure 2.38: Terms responsible for fluctuation. Anisotropic

The behavior of anisotropic elastic stiffness tensor are shown on figure (2.39).

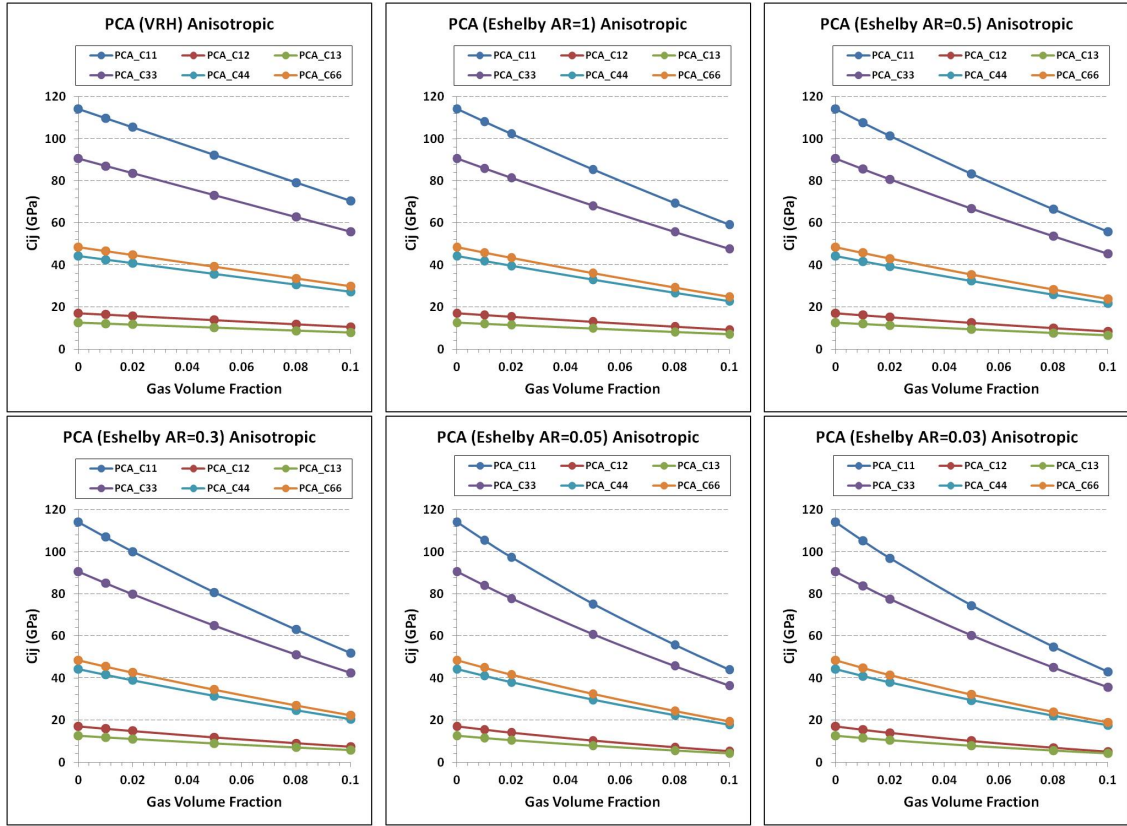


Figure 2.39: Effective stiffness tensor vs. gas content. Anisotropic

Elastic stiffness tensor values tend to decrease as gas concentration increases. Numerical data of stiffness tensor that were shown on figure (2.39) are presented in tables (2.33), (2.34), (2.35), (2.36), (2.37), and (2.38). All data of stiffness tensor are in gigapascal (GPa) units.

We observe that as gas concentration increases, stiffness tensor curves coincide. Specifically, C_{11} coincides with C_{33} , C_{12} coincides with C_{13} , and C_{44} coincides with C_{66} . Current phenomenon is especially noticeable when the aspect ratio of inclusions is small. This suggests that anisotropy tends to disappear and it can be explained by random orientation of inclusion in the medium. As an aspect ratio decreases, the

Table 2.33: PCA stiffness tensor values. VRH averaging. Anisotropic

Gas content	C_{11}	C_{12}	C_{13}	C_{33}	C_{44}	C_{66}
0	114.17	17.15	12.687	90.525	44.25	48.51
0.01	109.793	16.493	12.200	87.055	42.554	46.649
0.02	105.431	15.837	11.716	83.596	40.863	44.797
0.05	92.291	13.864	10.256	73.177	35.769	39.214
0.08	79.187	11.895	8.800	62.788	30.692	33.646
0.1	70.469	10.586	7.831	55.875	27.312	29.942

Table 2.34: PCA stiffness tensor values. Eshelby AR=1. Anisotropic

Gas content	C_{11}	C_{12}	C_{13}	C_{33}	C_{44}	C_{66}
0	114.17	17.15	12.687	90.525	44.25	48.51
0.01	108.164	16.304	12.115	85.895	41.914	45.929
0.02	102.303	15.475	11.553	81.368	39.636	43.414
0.05	85.372	13.061	9.889	68.243	33.055	36.156
0.08	69.376	10.755	8.278	55.789	26.842	29.311
0.1	59.15	9.271	7.229	47.8	22.87	24.94

Table 2.35: PCA stiffness tensor values. Eshelby AR=0.5. Anisotropic

Gas content	C_{11}	C_{12}	C_{13}	C_{33}	C_{44}	C_{66}
0	114.17	17.15	12.687	90.525	44.25	48.51
0.01	107.66	16.169	12.02	85.535	41.75	45.745
0.02	101.347	15.217	11.37	80.682	39.325	43.065
0.05	83.311	12.501	9.487	66.751	32.385	35.405
0.08	66.505	9.972	7.708	53.693	25.908	28.267
0.1	55.86	8.371	6.57	45.388	21.799	23.745

number of inclusions or crack density increases, preserving the same total volume fraction of inclusions; therefore their random orientation makes medium behave more like isotropic at gas concentration of ten and higher percentage, even though the matrix is of hexagonal symmetry.

Table 2.36: PCA stiffness tensor values. Eshelby AR=0.3. Anisotropic

Gas content	C_{11}	C_{12}	C_{13}	C_{33}	C_{44}	C_{66}
0	114.17	17.15	12.687	90.525	44.25	48.51
0.01	107.019	15.992	11.894	85.076	41.544	45.513
0.02	100.142	14.887	11.133	79.816	38.936	42.628
0.05	80.783	11.812	8.987	64.913	31.563	34.486
0.08	63.062	9.038	7.002	51.165	24.784	27.012
0.1	51.967	7.319	5.791	42.513	20.525	22.325

Table 2.37: PCA stiffness tensor values. Eshelby AR=0.05. Anisotropic

Gas content	C_{11}	C_{12}	C_{13}	C_{33}	C_{44}	C_{66}
0	114.17	17.15	12.687	90.525	44.25	48.51
0.01	105.521	15.587	11.607	84.001	41.057	44.967
0.02	97.378	14.146	10.604	77.821	38.034	41.616
0.05	75.255	10.37	7.94	60.861	29.734	32.443
0.08	55.822	7.192	5.662	45.793	22.363	24.316
0.1	43.965	5.304	4.295	36.534	17.833	19.332

Table 2.38: PCA stiffness tensor values. Eshelby AR=0.03. Anisotropic

Gas content	C_{11}	C_{12}	C_{13}	C_{33}	C_{44}	C_{66}
0	114.17	17.15	12.687	90.525	44.25	48.51
0.01	105.311	15.531	11.567	83.85	40.988	44.889
0.02	96.995	14.047	10.534	77.544	37.907	41.474
0.05	74.516	10.187	7.807	60.317	29.486	32.165
0.08	54.883	6.968	5.497	45.091	22.042	23.959
0.1	42.945	5.066	4.118	35.765	17.482	18.941

Based on the estimated stiffness tensor values and knowing densities, we can calculate velocities using the following expressions for vertical transversely isotropic (VTI) medium:

$$V_P(0) = \sqrt{\frac{C_{33}}{\rho}}; \quad V_{SV}(0) = \sqrt{\frac{C_{44}}{\rho}}; \quad V_{SH}(90) = \sqrt{\frac{C_{66}}{\rho}} \quad (2.50)$$

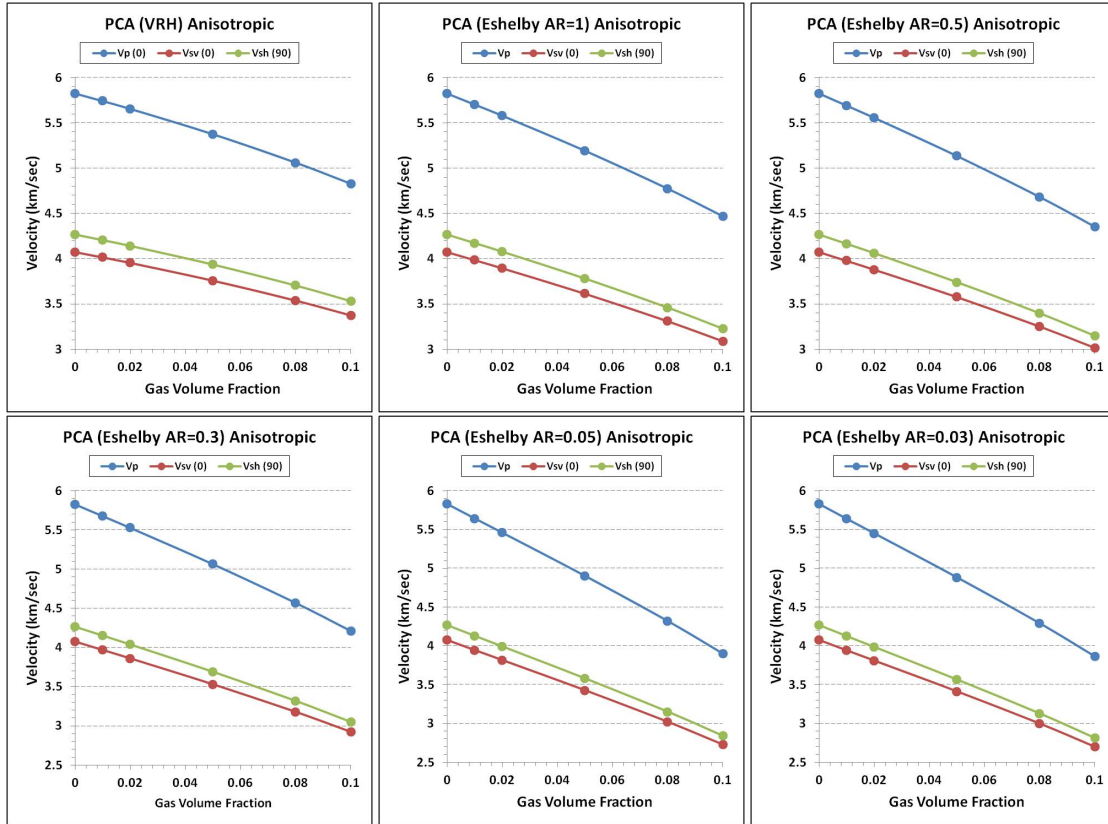


Figure 2.40: Velocity vs. gas content. Anisotropic

Table 2.39: PCA velocities. VRH. Anisotropic

Gas content	V_P (km/sec)	V_{SV} (km/sec)	V_{SH} (km/sec)	ρ (g/cc)
0	5.828	4.075	4.266	2.665
0.01	5.744	4.016	4.205	2.638
0.02	5.658	3.956	4.142	2.612
0.05	5.376	3.759	3.936	2.531
0.08	5.060	3.538	3.704	2.451
0.1	4.826	3.374	3.533	2.398

Velocities behavior is similar to the behavior of stiffness tensor. As gas concentration increases, velocities tend to decrease, and when gas concentration reaches ten percent at low aspect ratio (0.03), shear-wave velocities (V_{SV} and V_{SH}) tend to

Table 2.40: PCA velocities. Eshelby AR=1. Anisotropic

Gas content	V_P (km/sec)	V_{SV} (km/sec)	V_{SH} (km/sec)	ρ (g/cc)
0	5.828	4.075	4.266	2.665
0.01	5.706	3.986	4.172	2.638
0.02	5.582	3.896	4.077	2.612
0.05	5.192	3.614	3.779	2.531
0.08	4.771	3.309	3.458	2.451
0.1	4.465	3.089	3.225	2.398

Table 2.41: PCA velocities. Eshelby AR=0.5. Anisotropic

Gas content	V_P (km/sec)	V_{SV} (km/sec)	V_{SH} (km/sec)	ρ (g/cc)
0	5.828	4.075	4.266	2.665
0.01	5.694	3.978	4.164	2.638
0.02	5.558	3.881	4.061	2.612
0.05	5.135	3.577	3.739	2.531
0.08	4.680	3.251	3.396	2.451
0.1	4.351	3.015	3.147	2.398

Table 2.42: PCA velocities. Eshelby AR=0.3. Anisotropic

Gas content	V_P (km/sec)	V_{SV} (km/sec)	V_{SH} (km/sec)	ρ (g/cc)
0	5.828	4.075	4.266	2.665
0.01	5.679	3.968	4.153	2.638
0.02	5.528	3.861	4.040	2.612
0.05	5.064	3.531	3.691	2.531
0.08	4.569	3.179	3.319	2.451
0.1	4.211	2.926	3.051	2.398

coincide indicating an isotropic behavior. Again this behavior is due to the random orientation of larger number of inclusions having small aspect ratios.

Table 2.43: PCA velocities. Eshelby AR=0.05. Anisotropic

Gas content	V_P (km/sec)	V_{SV} (km/sec)	V_{SH} (km/sec)	ρ (g/cc)
0	5.828	4.075	4.266	2.665
0.01	5.643	3.945	4.128	2.638
0.02	5.459	3.816	3.992	2.612
0.05	4.903	3.427	3.580	2.531
0.08	4.322	3.021	3.149	2.451
0.1	3.904	2.727	2.839	2.398

Table 2.44: PCA velocities. Eshelby AR=0.03. Anisotropic

Gas content	V_P (km/sec)	V_{SV} (km/sec)	V_{SH} (km/sec)	ρ (g/cc)
0	5.828	4.075	4.266	2.665
0.01	5.638	3.942	4.125	2.638
0.02	5.449	3.809	3.985	2.612
0.05	4.881	3.413	3.565	2.531
0.08	4.289	2.999	3.126	2.451
0.1	3.862	2.700	2.811	2.398

Elastic anisotropy might be clearly visualized by plotting anisotropy coefficient as a function of gas volume concentration, figure (2.41).

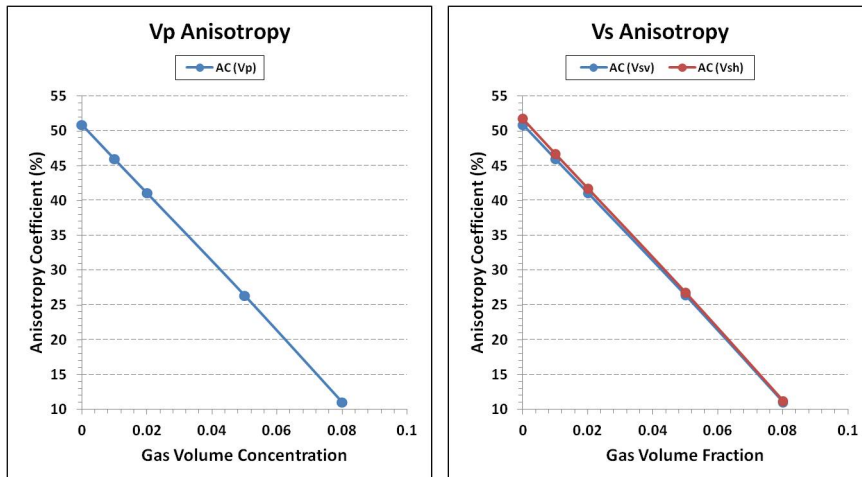


Figure 2.41: Anisotropy coefficient vs. gas content at aspect ratio of 0.03

The anisotropy coefficient based on SV-wave velocity is higher than the one based on P-wave velocity. Statistically, it has been reported (Brodov et al., 1991) that the commonly observed aspect ratio of cracks is around 0.02 - 0.03. This is the reason why this particular aspect ratio was chosen. As a gas volume concentration increases, anisotropy coefficient tend to decrease because crack density increases. If we have no inclusions in the media, the anisotropy coefficient due to layering may acquire the value of over 20 percent. As in the previous subsection, we would like to understand the behavior of fluctuation as a function of correlation radius. In the same manner we introduce Gaussian normal distribution to equation (2.33), where initially distribution function was equal one. Therefore, we obtain the following expression:

$$C_{ijnp}^* = \langle C_{ijnp} \rangle + \frac{1}{8\pi^3} A_{mqnp}^{ijkl} \int \exp \left[i\mu \mathbf{k} - \frac{1}{2} (\sigma \mathbf{k})^2 \right] \frac{\Gamma_{ik}^{adj}(\mathbf{k})}{\det|\Gamma(\mathbf{k})|} \exp^{i\mathbf{k}r} d\mathbf{k} \quad (2.51)$$

Integration was performed numerically using package Maple14. Figure (2.42) represents calculated stiffness tensor values obtained without Gaussian distribution (2.42(A)) and as a function of sigma (2.42(B)) at five percent of gas content.

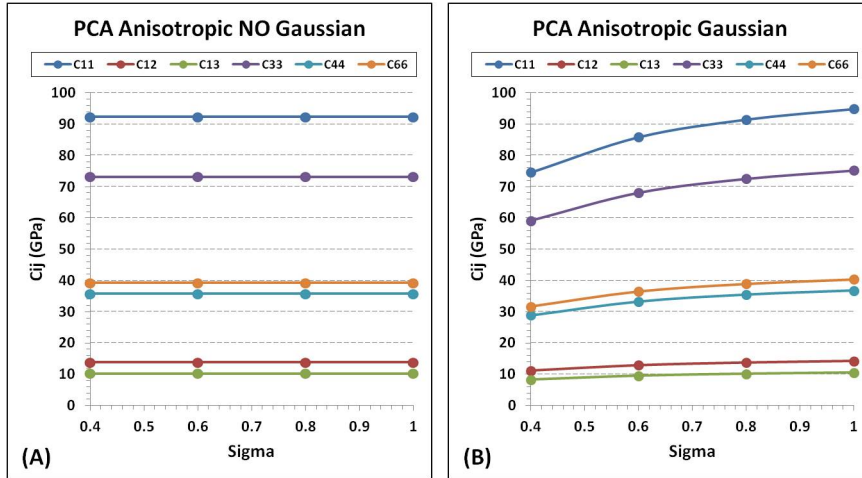


Figure 2.42: PCA stiffness tensor vs. σ at gas content of five percent. VRH averaging is implemented. (A) No Gaussian (B) With Gaussian

The highest correlation is observed at low values of standard deviation (σ), and as the distance increases the stiffness tensor values approach the values of stiffness tensor calculated without applying Gaussian distribution. The mean value in normal distribution (μ) is set to be zero, representing the boundary between correlating end-members. Stiffness tensor values presented in figure (2.42) were calculated using VRH averaging. In the case of Eshelby's averaging we show values for medium with gas content of five percent and with aspect ratio of inclusion equal to 0.03, figure (2.43).

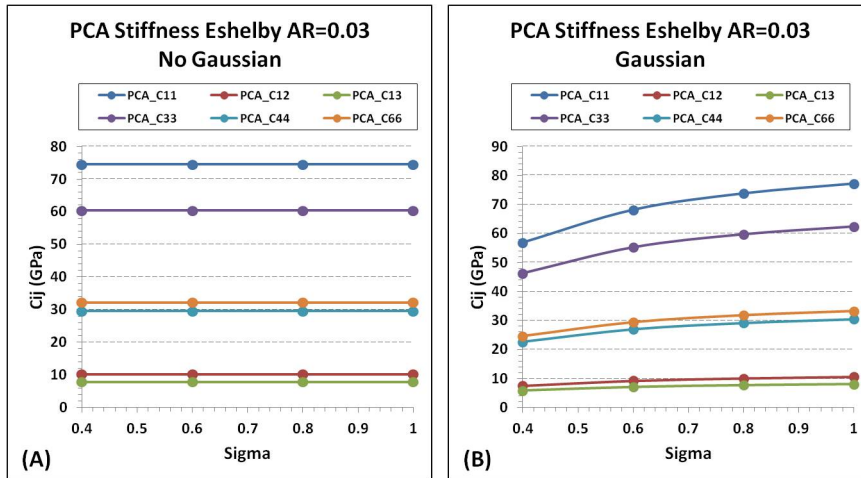


Figure 2.43: PCA stiffness tensor vs. sigma at gas content of five percent and AR=0.03. Eshelby's averaging is implemented. (A) No Gaussian (B) With Gaussian

Figure (2.43(A)) represents the values of stiffness tensor without applying Gaussian distribution function, and figure (2.43(B)) represents the values of stiffness tensor with Gaussian distribution applied. Similar behavior of higher correlation at lower sigma values is observed on velocities shown on figure (2.44) for VRH averaging and on figure (2.45) for Eshelby's averaging. As standard deviation increases, the correlation amplitude decreases until it reaches the point of no correlation at all. Again, the gas content is five percent and aspect ratio of inclusions is 0.03, making the crack density to be 0.398. This value of crack density is high, and the random distribution of inclusions may result in the reduction of anisotropy that was observed and discussed earlier.

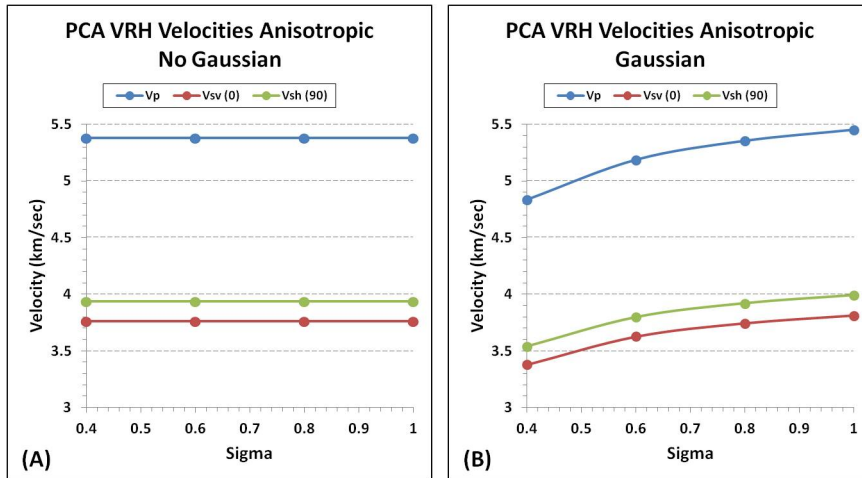


Figure 2.44: PCA velocities vs. sigma at gas content of five percent. VRH averaging is implemented. (A) No Gaussian (B) With Gaussian

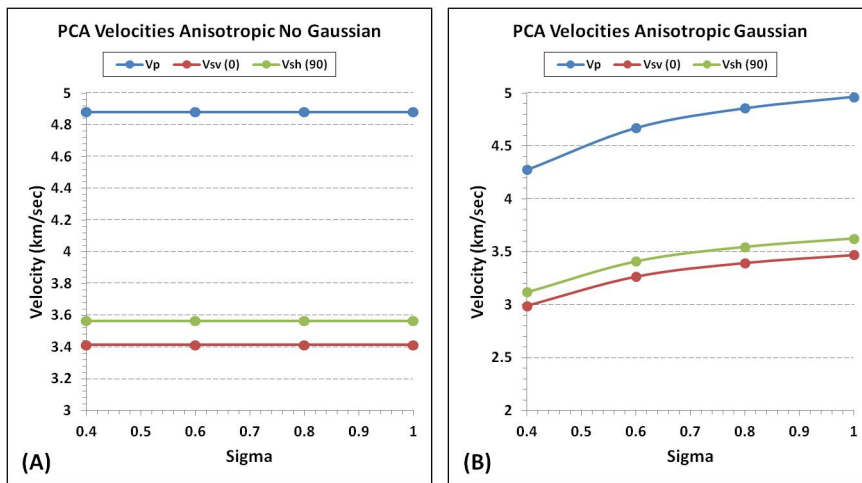


Figure 2.45: PCA velocities vs. sigma at gas content of five percent and AR=0.03. Eshelby's averaging is implemented. (A) No Gaussian (B) With Gaussian

The Poisson's ratios for an anisotropic medium have also been computed using PCA technique based on both the VRH and Eshelby's averaging methods. Results are presented on figure (2.46) for different values of standard deviation. The gas volume concentration is five percent and aspect ratio for Eshelby's case is 0.03.

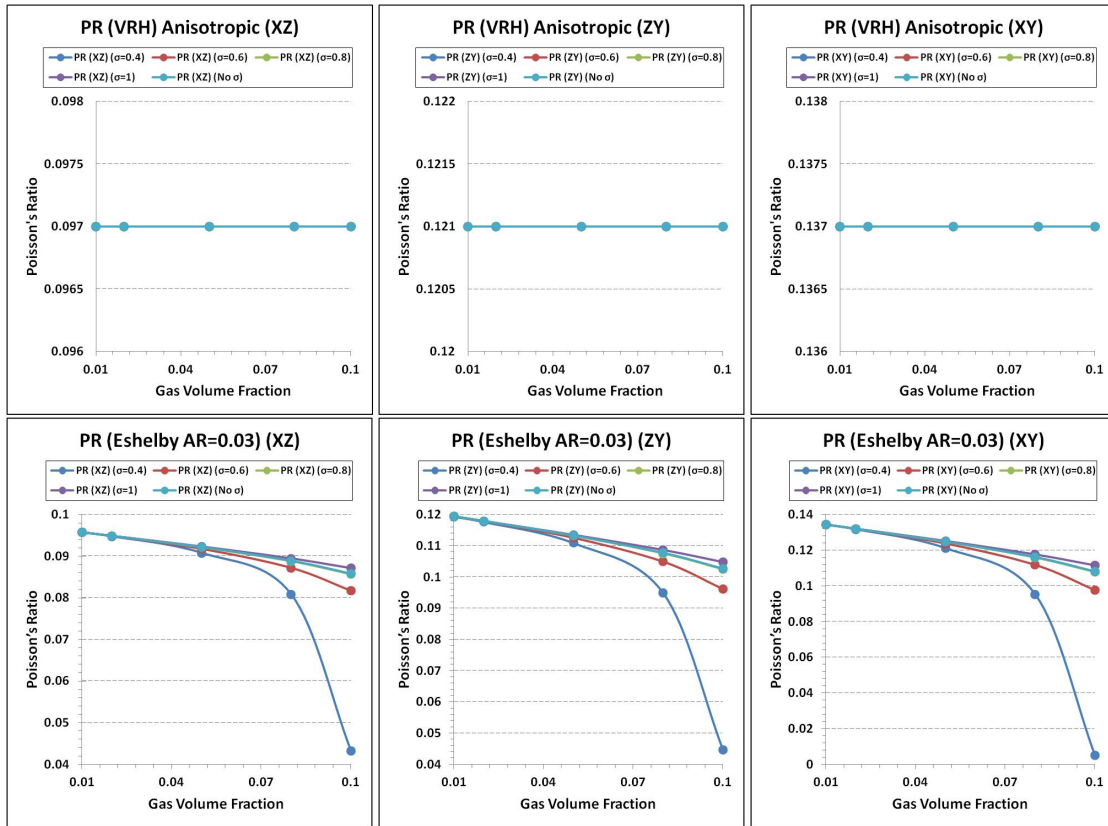


Figure 2.46: PCA Poisson's ratio vs. sigma at five percent of gas and AR=0.03.

Anisotropy can also be expressed through Thomsen's parameters, figure (2.47). Usually in the case of shales Thomsen's parameters ϵ and γ are positive and δ goes from positive to negative (Wenk, Lonardelli, Franz, Nihei, & Nakagawa, 2007). However, in our case all three parameters take positive values.

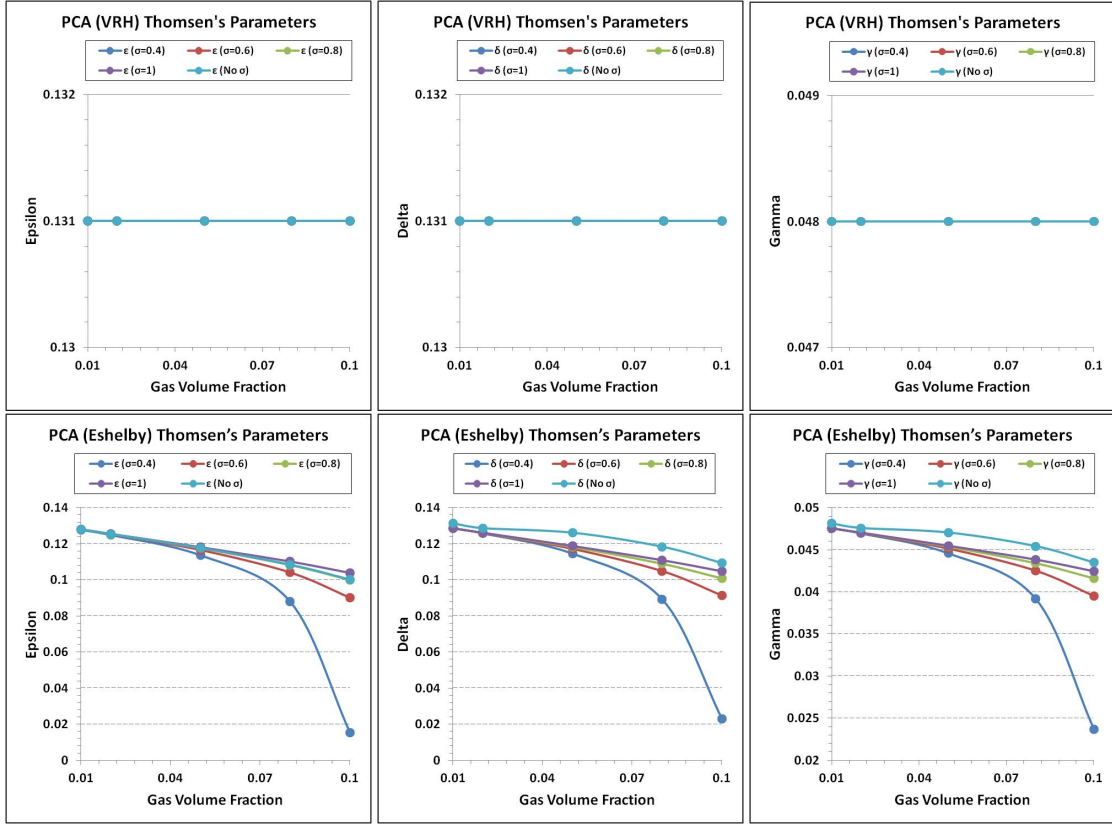


Figure 2.47: PCA Thomsen's parameters vs. gas content and vs. sigma at AR=0.03.

2.5 Comparison With Laboratory Data

In this section we report the comparison of the data calculated using PCA technique for anisotropic medium of hexagonal type of symmetry with the data obtained through the measurements in the laboratory. Laboratory data have been reported in section (2.1). Porosity measured in the laboratory is reported to be over five percent. Theoretical calculations were made over the range of porosity from zero to ten percent; however in this section we report the range of porosity from five to

eight percent. Table (2.45) shows the values of elastic stiffness tensor obtained both theoretically and experimentally.

Table 2.45: Comparison of calculated (PCA) with measured stiffness tensor values

Name	PCA (Por 5%)	PCA (Por 8%)	Exp (Por > 5%)
C_{11}	74.516	54.883	73.064
C_{12}	10.187	6.968	12.864
C_{13}	7.007	5.007	10.217
C_{33}	60.317	45.091	53.376
C_{44}	29.486	22.042	21.102
C_{66}	32.165	23.959	30.100

Elastic stiffness tensor values obtained theoretically through the PCA method show a reasonable match with experimental data, figure (2.48).

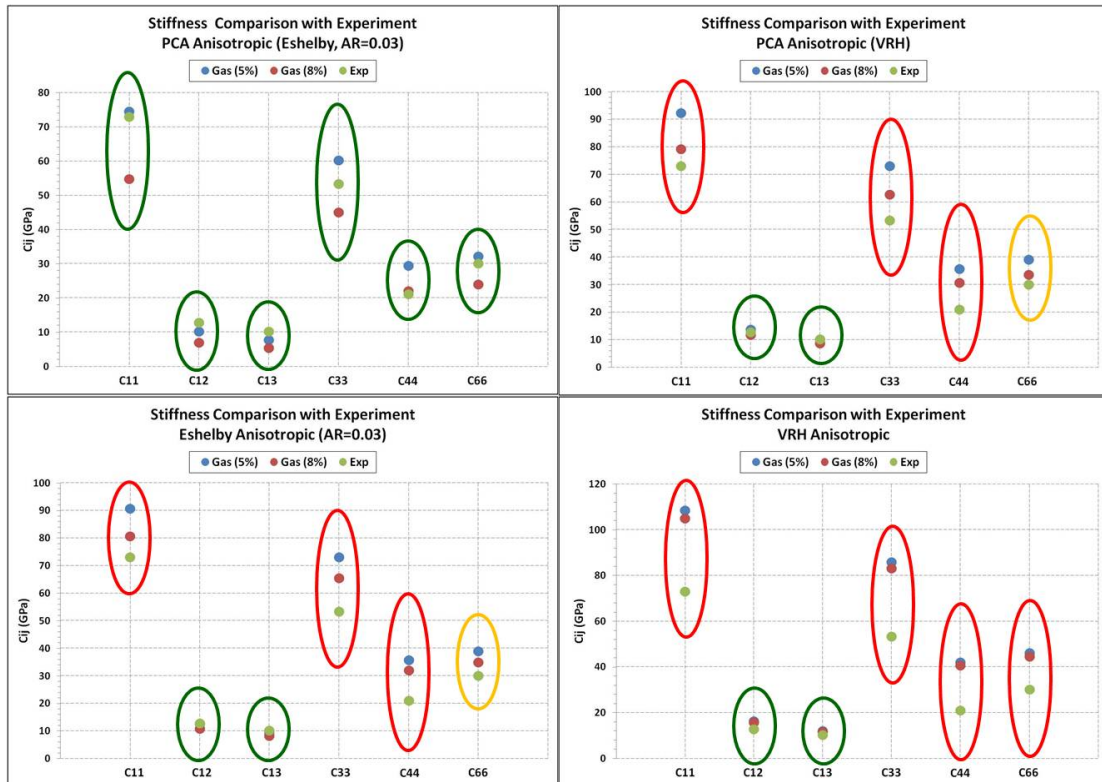


Figure 2.48: Comparison of calculated (PCA) with measured stiffness tensor values

In the figure (2.49), green circles indicate a good match, meaning that experimentally obtained results lie within the range of theoretically calculated values. Yellow circles indicate that the match is acceptable, while red circles highlight erroneous results. The calculations of C_{13} is slightly more complicated than the calculations of other stiffness tensor parameters. To calculate C_{13} it is required to have accurate measurements of velocity at an angle of 45 degrees to the bedding, which in turn is a hard task to accomplish and the error bar might be high. However, we observed a very good agreement between our calculations and measurements. Velocity comparisons are shown on figure (2.49) and recorded in table (2.46).

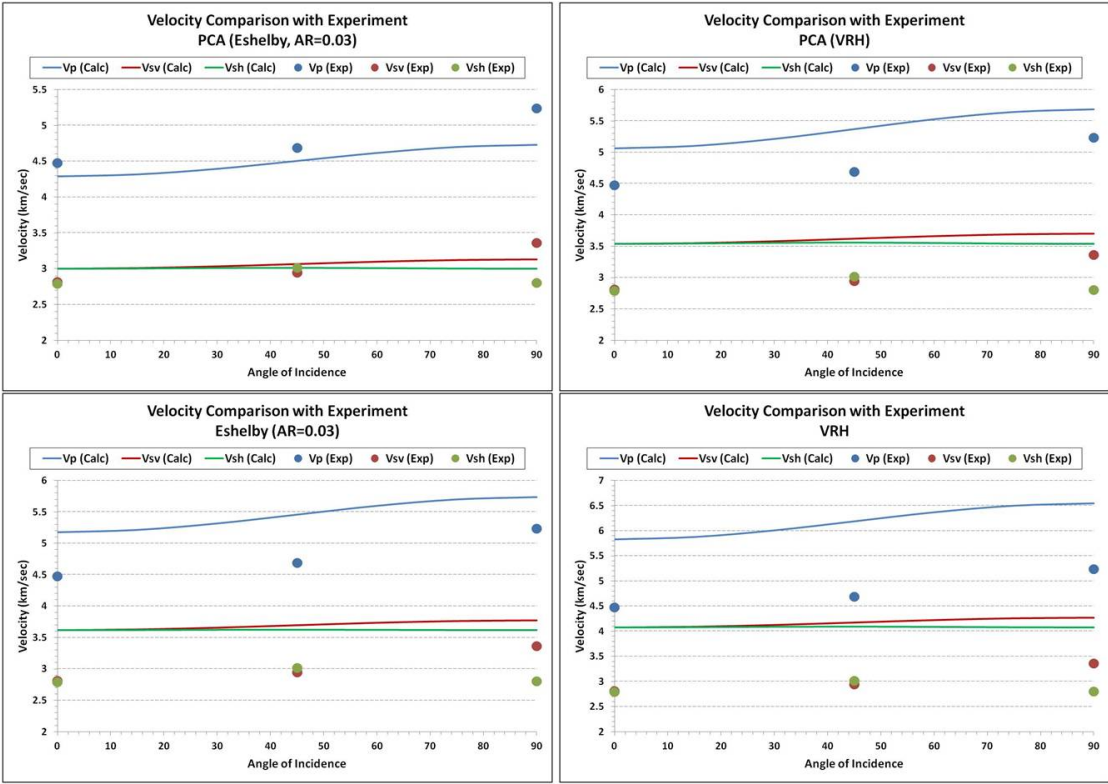


Figure 2.49: Comparison of calculated (PCA) with measured velocity values

Table 2.46: Comparison of calculated (PCA) with measured (Lab) velocity values

Name	PCA (Por 5%)	PCA (Por 8%)	Exp (Por > 5%)
V_P (0)	4.882	4.289	4.477
V_P (45)	5.147	4.506	4.690
V_P (90)	5.426	4.732	5.238
V_{SV} (0)	3.413	2.999	2.815
V_{SV} (45)	3.49	3.063	2.949
V_{SV} (90)	3.565	3.127	3.362
V_{SH} (0)	3.413	2.999	2.793
V_{SH} (45)	3.435	3.014	3.018
V_{SH} (90)	3.413	2.999	2.805

Usually, we observe minor inconsistency on the velocities values measured in the lab at 45 degrees to the bedding due to the inability to conduct measurement at exactly 45 degrees. Calculations show that velocity parallel to the bedding is the highest, perpendicular to the bedding is the lowest, and at 45 degrees to the bedding velocity value is between those two. Most lab measurements on rock samples as well as our sample (JR(III, IV)) display similar behavior. The behavior of Thomsen's parameters is shown on figure (2.50). As in the cases of stiffness tensor and velocity results, Thomsen's parameters are in agreement between calculations and measurements.

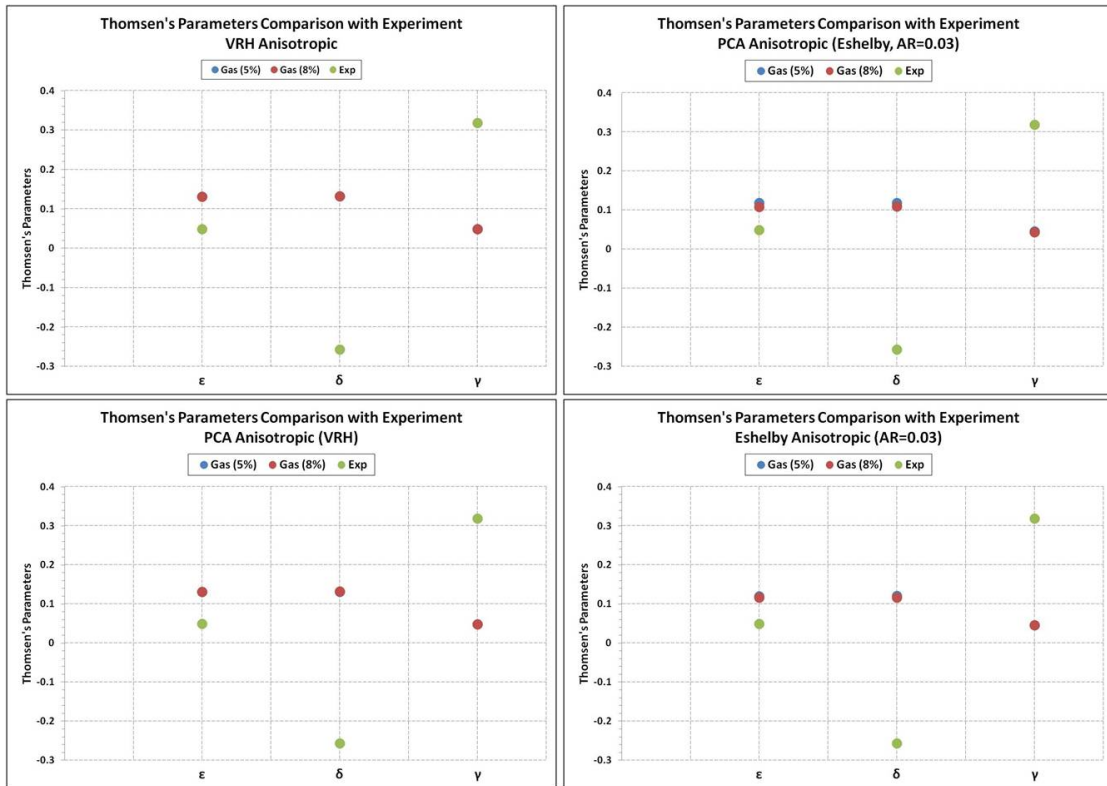


Figure 2.50: Comparison of theory with measurements of Thomsen's parameters

Analysis of calculations based on the theoretical model and comparison with the experimental results allows us to conclude that in general there is a good match in stiffness tensor values. Velocities and Thomsen's parameters also confirm the validity of theoretical results.

Conclusions

Spatial correlation function in the form of pair correlation approximation (PCA) has been implemented to characterize elastic properties of an isotropic and an anisotropic medium. PCA consists of an averaged value, which in our case is computed using either the VRH or Eshelby's method, and a fluctuation term that appears as a result of elastic interactions between constituents. To consider interactions between end-members, PCA uses Green's function along with its first and second derivatives. PCA has the ability to consider different types of symmetries; however we mostly concentrate on anisotropic medium with hexagonal symmetry due to the ability to compare our results with the laboratory measurements on the core samples of Barnett Shale, with hexagonal symmetry. Theoretical model has been built based on the mineralogical composition of the core sample. The medium consists of a solid matrix, which is an aggregated of quartz and illite, and gas inclusions which are represented by methane. Gas content varies from zero to ten percent; however laboratory measurements showed porosity of five to eight percent. Therefore, more attention was paid to the theoretical model with five to eight percent of gas inclusion.

PCA has been shown to be a more accurate technique for evaluating effective elastic properties of the medium compared to VRH (Voigt scheme) volume weighted averaging and Eshelby's averaging techniques. VRH averaging provides reliable results when the end-members of the medium are of the similar elastic properties, meaning that if we would be limited by quartz and illite in the medium, VRH averaging would provide a reasonable effective elastic properties. However, analyzed medium contains up to ten percent of gas, elastic properties of which vary dramatically, up to six orders of magnitude in stiffness tensor values. In this case it is more appropriate to consider a fluctuation term that characterizes the influence of each end-member on each other. In the case of isotropy the difference between the VRH and PCA techniques reached seven percent for stiffness tensor values at eight percent of gas concentration. The difference in an effective elastic stiffness tensor for an anisotropic medium reaches 25 percent at eight percent of gas concentration. In the case of velocities the difference in an isotropic medium reached about 3.3 percent while for an anisotropic medium it becomes around 6.5 percent. VRH averaging tends to oversimplify the medium by taking into consideration only the properties of each end-member and its volume fraction. PCA, on the other hand, demonstrates more solid physical background by taking into consideration all the properties that VRH considers and adding to it the fluctuations in elasticity that arises due to the influence of constituents on each other.

As an alternative to the VRH averaging technique, we implemented the Eshelby's method to obtain effective elastic properties. The advantage of Eshelby's method is that it allows us to consider the geometrical arrangement of inclusions by controlling their aspect ratio and orientation. Calculations were done for different values of aspect ratio; however more attention was focused on the inclusions with aspect ratio of 0.03 due to the higher frequency of their occurrence (Brodov et al., 1991). For the isotropic case, the difference between the VRH and Eshelby techniques with aspect ratio of inclusion of 0.03 is around 22 percent. This difference is high due to the significant influence of the low aspect ratio. If we consider a higher aspect ratio, the difference decreases; for example, if aspect ratio equals to one the difference drops to around 8 percent. In the case of anisotropy these differences are higher. For an aspect ratio of 0.03 this difference is around 30 percent, while for an aspect ratio of one the difference is 10 percent. Since we are working with shales with gas concentration of less than 10 percent which accumulates in very thin cracks, it is more reasonable to use Eshelby's technique due to two main reasons. The first reason is that it allows us to control aspect ratio, and the second reason is that Eshelby's model assumes no interaction between inclusions, which might satisfy our model with such low gas concentration.

In this work, the PCA technique, based on the Eshelby's averaging method with an added fluctuation term, is considered to be the closest approximation to the real geological situation due to the ability to control geometry of the gas-filled inclusions

and their interaction with the solid end-members. The difference in elastic stiffness tensor values between Eshelby's method alone and PCA technique for an isotropic medium reaches 8 percent, while for an anisotropic medium the difference is around 32 percent. Comparison between the PCA technique based on VRH averaging and the PCA technique based on Eshelby's averaging method shows the difference in elastic properties of 20.7 percent for an isotropic medium and up to 32.3 percent for an anisotropic medium. These differences are influential and might lead to a significant errors if we do not chose the right model.

Analysis of the obtained results shows that an anisotropic medium with inclusions of random orientation tends to reduce its anisotropy as the volume fraction of inclusions increases. At zero percent of gas in the medium the anisotropy is controlled by the alignment of clay minerals and anisotropy value is high. The effect of gas saturation on anisotropy is more profound when the the aspect ratio of the inclusions is low, meaning that at a constant aspect ratio an increase of inclusion's volume fraction increases the crack density, and eventually their random distribution reduces anisotropy dramatically. For example, with aspect ratio of 0.03 and gas volume concentration from zero to eight percent, anisotropy values based on P-wave decrease from about 50 percent to around 11 percent.

Comparison with the data obtained through laboratory measurements shows that the PCA model based on Eshelby's averaging technique is the closest approximation

to the real geological case. The porosity of the shale varies with direction, therefore, to obtain the exact value of porosity is a complicated task. However, the porosity for the sample described in this work has been measured to be over five percent. The theoretical model that was compared to the rock sample has a porosity range from five to eight percent. Calculated values of stiffness tensor are very similar to those obtained through measurements, the values are in the range of the reported porosity. The velocity values and Thomsen's anisotropy parameters calculated theoretically are in very good agreement with measurements.

Averaging techniques reported in this work have been programmed for both isotropic and anisotropic cases with different types of symmetry. Algorithms analytically derived for isotropic medium and numerically derived for anisotropic medium to compute Green's function along with its first and second derivatives have been coded. Finally, the PCA technique for isotropic and anisotropic medium has been programmed and tested on different models. The PCA technique has also been applied for the global Earth studies. Appendix shows results of PCA calculations for uppermost mantle beneath Gakkel Ridge. Based on PCA results, the elastic stiffness tensor values vary from about 14 to 23 percent with depth (averaging at around 18 percent). The variation with offset is from five to ten percent (averaging at around seven percent). The variation with depth is much more dramatic, with a factor of four variation between the uppermost 0-5km bin and the next 5-10km bin. The kinematic model of anisotropy that has been built based on the behavior of P-wave

velocities shows that anisotropy at Gakkel Ridge is the strongest (about eight percent) at the ridge crest, and varies strongly with depth and horizontal distance. At the depth of 20 km we observe the predomination of isotropy. At the offset of 80 km the anisotropy is three percent. The main cause of anisotropy in our area of study is considered to be the crystal preferred orientation and possibly the anisotropic nature of olivine and enstatite minerals.

Appendix

2.6 Application to Uppermost Mantle

Our research focuses on the northernmost portion of the Mid-Atlantic Ridge, the Gakkel Ridge. The Gakkel Ridge has a length of about 1800 km, and a spreading rate from 14.6 mm/year on its western end to 6.3 mm/year in the Laptev Sea (Michael et al., 2003). The ultra-slow spreading rate of the Gakkel Ridge allows us to test the PCA technique without the effects of partial melting. In contrast to intermediate or fast spreading ridges, spreading at ultra-slow ridges is not dominated by magmatic activity; extension at the spreading ridge is mainly accommodated by tectonic deformation (Sauter et al., 2009). The Pair Correlation Approximation was used to calculate elastic stiffness properties of an aggregate composed of 70 percent olivine and 30 percent enstatite as a function of depth and temperature. The elastic stiffness tensor (C_{ij}) values computed at room temperature (25C) and room pressure (1atm = 0.001GPa) for each mineral were taken from publications by Kumazawa and Anderson (Kumazawa & Anderson, 1969), Kumazawa (Kumazawa, 1969), and An-

derson (Anderson, 1988). Our results show that the general trend of stiffness tensor variation with depth and offset follows the trend of temperature variation with depth and offset, as expected, figure (2.51).

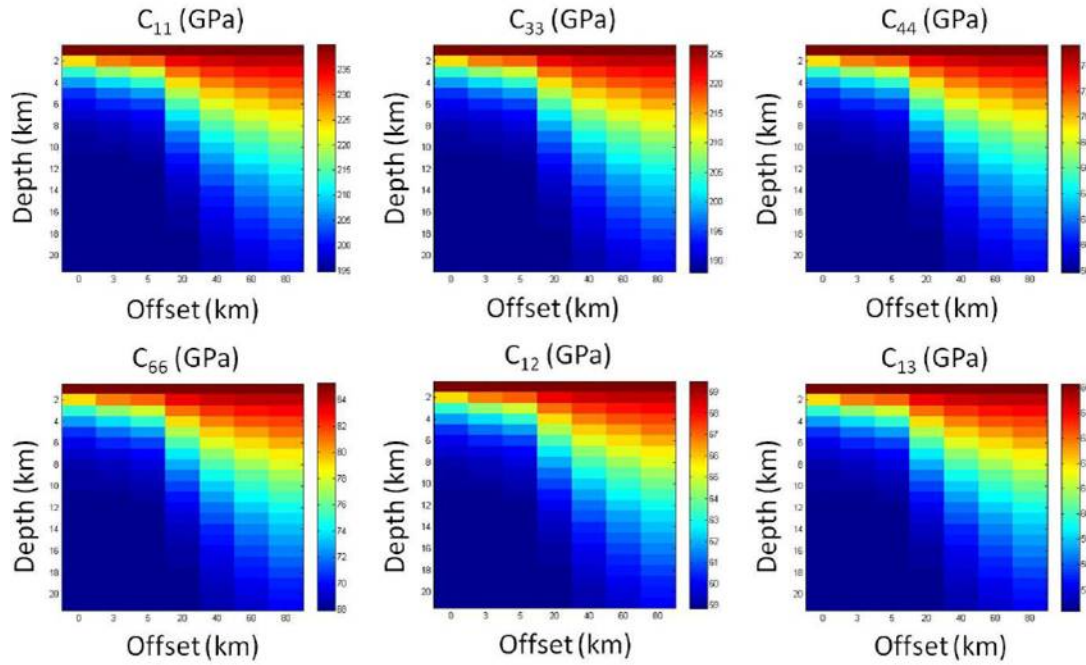


Figure 2.51: Stiffness tensor values as a function of depth and offset

The stiffness tensor values decrease with depth as temperature increases, and increase with offset because temperature decreases with offset from the spreading ridge. Total decrease of stiffness tensor values with depth and increase with offset are listed in Table (2.47) and (2.48). Elastic stiffness tensor values are represented in GPa.

The thermal structure underneath the Gakkel Ridge that was calculated by (Montesi & Behn, 2007). Their model is 40 km deep, with temperature boundary conditions of $0^{\circ}C$ at the top and $1370^{\circ}C$ at the bottom of the considered region. We used the upper 20 km of this model domain, as this is the region where most

Table 2.47: Variation of stiffness tensor with depth at zero-offset

Depth (km)	C_{11}	C_{12}	C_{13}	C_{33}	C_{44}	C_{66}
0	239.988	69.511	65.158	226.626	75.635	85.238
5	199.479	59.981	57.128	192.174	59.768	69.749
10	195.083	58.948	56.257	188.435	58.047	68.068
15	194.651	58.846	56.172	188.067	57.876	67.902
20	194.609	58.837	56.164	188.032	57.859	67.886

Table 2.48: Variation of stiffness tensor with offset at 5 km depth

Offset (km)	C_{11}	C_{12}	C_{13}	C_{33}	C_{44}	C_{66}
0	199.479	59.981	57.128	192.174	59.768	69.749
3	201.062	60.353	57.442	193.519	60.388	70.354
5	203.112	60.836	57.848	195.263	61.191	71.138
20	214.635	63.547	60.132	205.062	65.704	75.544

temperature variation is predicted. The temperature and pressure variations are shown on figure (2.52).

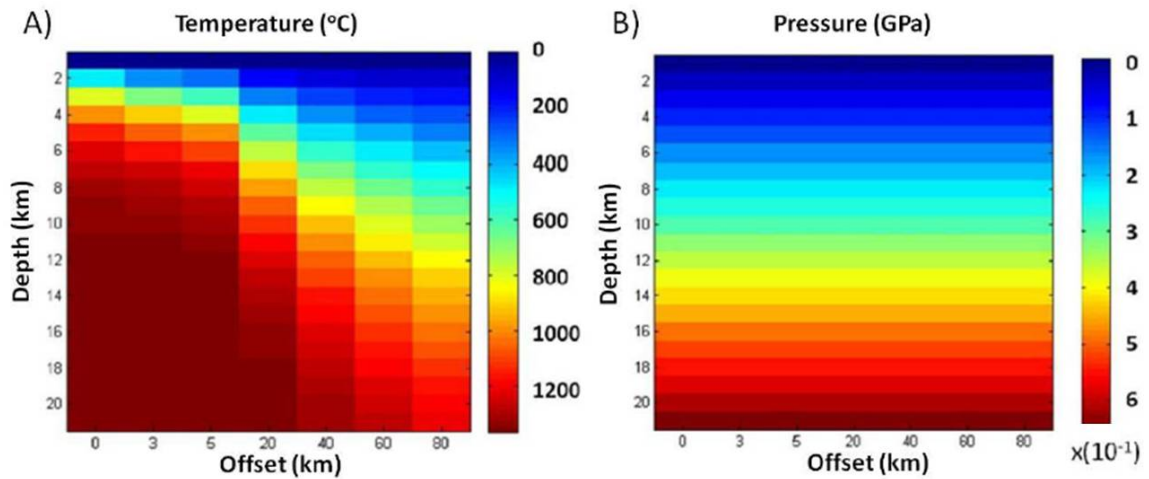


Figure 2.52: Temperature (A) and pressure (B) under Gakkel Ridge

The analytical solution for corner flow was used for advection of material. Tem-

perature decreases with distance from the ridge as the plate cools, figure (2.52(A)). Pressure, figure (2.52(B)), has been computed using the hydrostatic pressure equation: $P = \rho * g * h$. Here, ρ is density (3300 kg/m^3), g is acceleration due to gravity (9.807 m/s^2) and h is depth difference or height. Our results show that P-wave velocities decrease with depth and increase with offset, figure (2.53). The percentages of velocity variations with depth and with offset are shown in tables (2.49) and (2.50), respectively. The temperature is the main factor that controls the velocity variations.

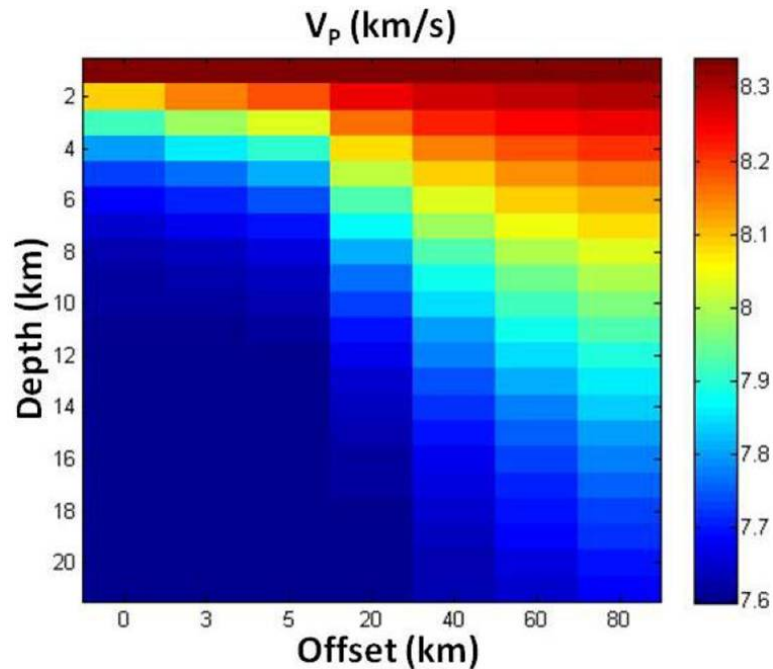


Figure 2.53: P-wave velocity variation under Gakkel Ridge

The behavior of the S-wave velocities (V_{S1} and V_{S2}) is identical to the behavior of the P-wave velocity (V_P), figure (2.54). Total velocities variation with depth and offset is around eight to nine percent.

Table 2.49: Variation of stiffness tensor with depth at zero-offset

Depth (km)	$V_P(km/sec)$	$V_{S1}(km/sec)$	$V_{S2}(km/sec)$
0	8.287	5.082	4.787
5	7.631	4.597	4.256
10	7.557	4.542	4.194
15	7.549	4.536	4.188
20	7.548	4.536	4.187

Table 2.50: Variation of velocity with offset at 5 km depth

Offset (km)	$V_P(km/sec)$	$V_{S1}(km/sec)$	$V_{S2}(km/sec)$
0	7.631	4.597	4.256
3	7.658	4.617	4.278
5	7.692	4.643	4.306
20	7.883	4.785	4.462

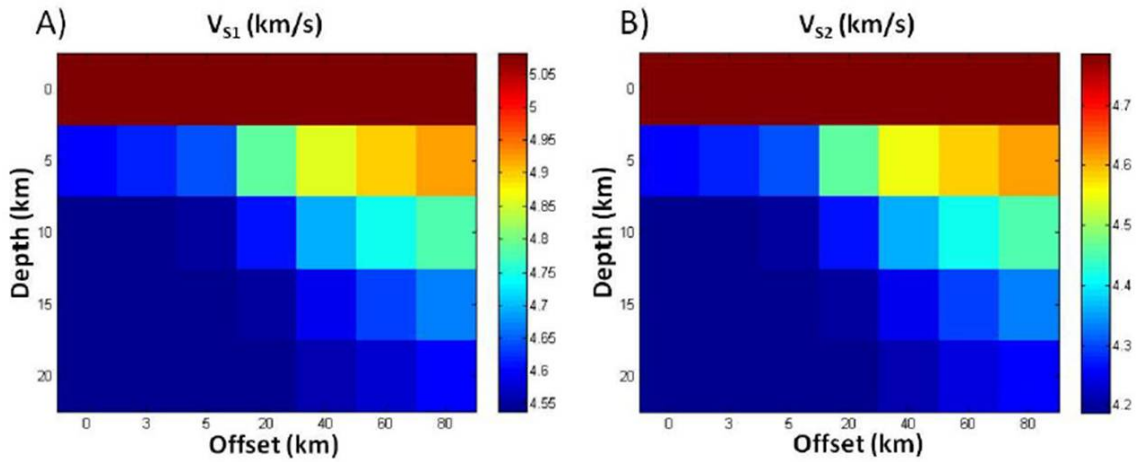


Figure 2.54: S-wave velocity variation under Gakkel Ridge

The anisotropy coefficients in percentages are computed by using the equation

involving P-wave velocity:

$$\left(\frac{V_P^{max} - V_P^{min}}{V_P^{average}}\right) * 100 \quad (2.52)$$

During sea-floor spreading the mantle advects upwards creating a viscous shear deformation (Gaherty, Lizarralde, Collins, Hirth, & Kim, 2004). This deformation causes mantle minerals to experience preferential orientation. With increasing deformation mantle minerals become more aligned, and therefore, as the spreading rate or advection rate increases, the level of mineral alignment increases. Since the spreading rate of the ridge is known, we can calculate a kinematic anisotropy model. Figure (2.55) demonstrates these kinematic variations of anisotropy with depth and lateral distance.

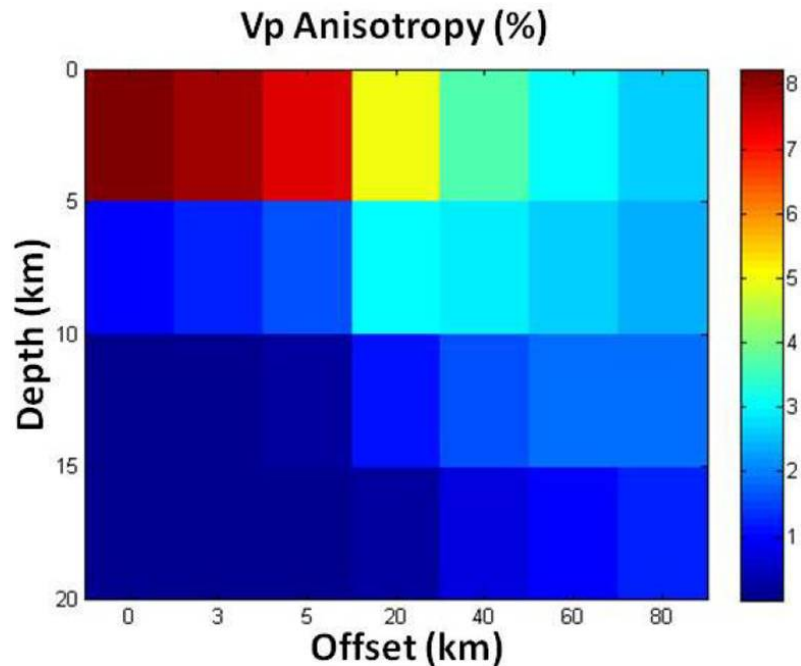


Figure 2.55: P-wave anisotropy under Gakkell Ridge

The highest values of the anisotropy are observed at shallow depths (0–5 km). Near the ridge crest, values up to 8 percent anisotropy in the depth interval 0–5 km drop to 1–2 percent in the 5–10 km interval, reflecting a much higher strain due to corner flow or high advection rate in the upper 5 km of the domain. The higher the spreading rate, the higher the rate of advection of mantle material, hence the higher the strain. However, in our case of ultra-slow spreading rate material under the corner flow advects faster than the spreading rate would predict. Therefore, in this particular case the corner flow field has a higher influence on mineral alignment and hence anisotropy than the spreading rate. Offset has a much more subtle effect, reducing the anisotropy in the uppermost layer by 50 percent in the first 40 km away from the ridge crest. There are several possible explanations for this anisotropy. Laboratory experiments on mantle minerals show that the mantle minerals are anisotropic (Christensen & Crosson, 1968; Mainprice, 2007). Olivine and enstatite possess an orthorhombic symmetry. However, the uppermost mantle at Gakkel Ridge is modeled as having hexagonal symmetry. This can be explained by the preferred orientation of dominating minerals and their possible rotations around one axis of symmetry. The fastest axis of olivine (axis a) tends to orient parallel to the flow (i.e. perpendicular to the ridge). The Crystal Preferred Orientation might be affected by partial melt, the presence of which may itself introduce anisotropy (Hirth & Kohlstedt, 1995). This possibility is less likely since the ultra-slow spreading rate (14–6.5 mm per year full rate) at Gakkel Ridge suggests that substantial melting in that area is not active (Jokat et al., 2003). Several other explanations of

anisotropy, like intra-granular slippage, and dislocation creep have been proposed by different scientists (Karato, 2008), (Korenaga & Karato, 2008).

References

- Anderson, D. L. (1988). Temperature and pressure derivatives of elastic constants with application to the mantle. *Journal of Geophysical Research*, *93*, 4688–4700.
- Backus, G. E. (1962). Long-wave elastic anisotropy reduced by horizontal layering. *Journal of Geophysical Research*, *67*(11), 4427–4440.
- Bayuk, I., Ammerman, M., & Chesnokov, E. M. (2007b). Upscaling of elastic properties of anisotropic rocks. *Journal of Geophysical International*, *172*(842–860).
- Belikov, B. P., Alexandrov, K., & Ryzhova, T. V. (1970). Elastic properties of rock forming minerals and rocks. *Nauka Publishers*, *15*, in Russian.
- Biot, M. A. (1956). Theory of propagation of elastic waves in a fluid saturated porous solid. i. low frequency range and ii. higher-frequency range. *J. Acoust. Soc. Am.*, *28*, 168–191.
- Brodov, L. U., Tikhonov, A. A., Chesnokov, E. M., Tertychnyi, V. V., & Zatsepin, S. V. (1991). Estimating physical parameters of cracked-porous oil reservoirs

- by inverting shear-wave splitting. *Geoph. J. Int.*, *107*, 429–432.
- Chen, D. (2012). *Microstructure study on Barnett Shale*. Unpublished master's thesis, University of Houston.
- Chesnokov, E. M., & Kukharenko, Y. A. (1996). Tensor of effective density for media with inclusions. *SEG Expanded Abstracts*, *1*, 1033–1036.
- Chesnokov, E. M., Kukharenko, Y. A., & Kukharenko, P. A. (1995). Method of diagram technique for calculation of effective physical parameters of microinhomogeneous media. *SPIE, Mathematical Methods in Geophysical Imaging III*, *2577*, 2–12.
- Chesnokov, E. M., & Zatsepin, S. V. (1991). Effect of applied stress on effective elastic anisotropy in cracked solids. *Geoph. J. Int.*, *107*, 563–569.
- Christensen, N. I., & Crosson, R. S. (1968). Seismic anisotropy in the upper mantle. *Tectonophysics*, *6*, 93–107.
- Dederichs, P. H., & Liebfried, G. (1969). Elastic Green's function for anisotropic cubic crystals. *Phys. Rev.*, *188*, 1175–1183.
- Eshelby, J. D. (1957). The determination of the elastic field of an ellipsoidal inclusion, and related problems. *Proc. Royal Soc. London*, *A241*, 376–396.
- Gaherty, J. B., Lizarralde, D., Collins, J. A., Hirth, G., & Kim, S. D. (2004). Mantle deformation during slow seafloor spreading constrained by observations of seismic anisotropy in the western Atlantic. *Earth and Planetary Science Letters*, *228*, 255–265.
- Gassmann, F. (1951). Elastic waves through a packing of spheres. *Geophysics*, *16*,

673–685.

- Hashin, Z., & Shtrikman, S. (1963). A variational approach to the theory of the elastic behavior of multiphase materials. *J. Mech. Phys. Solids*, *11*, 127–135.
- Hill, R. (1952). The elastic behavior of crystalline aggregate. *Proc. Physical Soc. London*, *A65*, 349–354.
- Hill, R. (1963). Elastic properties of reinforced solids: Some theoretical principles. *J. Mech. Phys. Solids*, *11*, 357–372.
- Hirth, G., & Kohlstedt, D. L. (1995). Experimental constraints on the dynamics of the partially molten upper mantle: Deformation in the diffusion creep regime. *Journal of Geophysical Research*, *100*, 1981–2001.
- Jokat, W., Ritzmann, O., Schmidt-Aursch, M., Drachev, S., Gauger, S., & Snow, J. (2003). Geophysical evidence for reduced melt production on the Arctic ultraslow Gakkel mid-ocean Ridge. *Nature*, *423*(6943), 962–965.
- Karato, S. (2008). *Deformation of earth materials: Introduction to the rheology of solid earth*. Cambridge University Press.
- Katahara, K. (1996). Clay minerals elastic properties. *SEG Expanded Abstract*, *15*, 1691–1694.
- Korenaga, & Karato, S. (2008). A new analysis of experimental data on olivine rheology. *Journal of Geophysical Research*, *113*.
- Kumazawa, M. (1969). The elastic constants of single-crystal orthopyroxene. *Journal of Geophysical Research*, *74*, 5973–5980.
- Kumazawa, M., & Anderson, O. L. (1969). Elastic moduli, pressure derivatives, and

- temperature derivatives of single-crystal olivine and single crystal forsterite. *Journal of Geophysical Research*, *74*, 5961–5972.
- Kuster, G. T., & Toksoz, M. N. (1974). Velocity and attenuation of seismic waves in two-phase media. *Geophysics*, *39*, 587–618.
- Lifshitz, I. M., & Rozentsweig, L. N. (1946). On the theory of elastic properties of polycrystals. *Z. Eksp. Teor. Fiz.*, *16*(11), in Russian.
- Lifshitz, I. M., & Rozentsweig, L. N. (1947). Construction of the Green tensor for the basic equation of the theory of elasticity for the case of an anisotropic infinite medium. *Z. Eksp. Teor. Fiz.*, *17*, 783–791.
- Mainprice, D. (2007). Seismic anisotropy of the deep earth from a mineral and rock physics perspective. *Treatise on Geophysics*, *2*, 437–492.
- Michael, P. J., Langmuir, C. H., Dick, H. J. B., Snow, J. E., Goldstein, S. L., Graham, D. W., . . . Edmonds, H. N. (2003). Magmatic and amagmatic seafloor generation at the ultraslow-spreading Gakkel Ridge, Arctic Ocean. *Nature*, *423*, 956.
- Montesi, G. J., & Behn, M. D. (2007). Mantle flow and melting underneath oblique and ultraslow mid-ocean ridges. *Geophysical Research Letters*, *34*, L24307.
- Mura, T. (1991). *Micromechanics of defects in solids*. Kluwer Academic Publisher.
- Phan, A. V., Gray, L. J., & Kaplan, T. (2004). On the residue calculus evaluation of the 3-d anisotropic elastic Green's function. *Communication in Numerical Methods in Engineering*, *20*, 335–341.
- Reuss, A. (1929). Berechnung der fließgrenzen von mischkristallen auf grund der

- plastizitätsbedingung für Einkristalle. *Zeitschrift für Angewandte Mathematik und Mechanik*, 9, 49–58.
- Sales, M., & Gray, L. J. (1998). Evaluation of the anisotropic Green's function and its derivatives. *Computers and Structures*, 69, 247–254.
- Sauter, D., Cannat, M., Meyzen, C., Bezos, A., Patriat, P., Humler, E., & Debayle, E. (2009). Propagation of a melting anomaly along the ultra-slow southwest Indian Ridge between 46°E and 52°20'E: Interaction with the Crozet hot-spot? *Geophys. J. Int.*, in press.
- Shermergor, T. D. (1977). *Theory of elasticity of micro-inhomogeneous media*. Nauka.
- Thomsen, L. (1995a). Elastic anisotropy due to aligned cracks in porous rock. *Geoph. Prospg.*, 43, 805–829.
- Tiwary, K. D. (2007). *Mathematical modeling and ultrasonic measurements of shale anisotropy and a comparison of upscaling methods from sonic to seismic*. Unpublished doctoral dissertation, University of Oklahoma.
- Voigt, W. (1928). Lehrbuch der Kristallphysik. Teubner, Leipzig, 962.
- Wang, C.-Y., & Achenbach, J. D. (1995). Three-dimensional time-harmonic elastodynamic Green's functions for anisotropic solids. *Proc. Royal Soc. London*, A449, 441–458.
- Wenk, H.-R., Lonardelli, I., Franz, H., Nihei, K., & Nakagawa, S. (2007). Preferred orientation and elastic anisotropy of illite-rich shale. *Geophysics*, 72(2), E69–E75.